ON THE IMPACT OF ELECTRODE PROPERTIES AND THEIR DESIGN FOR REDOX FLOW BATTERY PERFORMANCE

by

Katharine V. Greco

Master of Science in Chemical Engineering Practice, Massachusetts Institute of Technology, 2018
Bachelor of Science in Chemical Engineering, University of Massachusetts Amherst, 2016

Submitted to the Department of Chemical Engineering
in partial fulfillment of the requirements for the degree of

Doctor of Philosophy in Chemical Engineering
at the
MASSACHUSETTS INSTITUTE OF TECHNOLOGY
September 2021

Author ....
Department of Chemical Engineering
August 9th, 2021

Certified by ....
Fikile R. Brushett
Cecil and Ida Green Career Development Chair
Thesis Supervisor

Accepted by ....
Patrick S. Doyle
Robert T. Haslam Professor of Chemical Engineering
Singapore Research Professor
Chairman, Committee for Graduate Students

On the impact of electrode properties and their design for redox flow battery performance

by

Katharine V. Greco

Submitted to the Department of Chemical Engineering on 9 August 2021, in partial fulfillment of the requirements for the degree of

Doctor of Philosophy in Chemical Engineering

Abstract

Redox flow batteries (RFBs) are a promising technology for grid energy storage. However, cost reductions are required prior to widespread adoption. Advances in the design and engineering of the electrochemical stack may enable cost reductions for multiple redox chemistries. Porous electrodes are a prime target for improvement of system power to lower cost per kilowatt-hour, as they are responsible for multiple critical functions in the flow cell including providing surfaces for electrochemical reactions, distributing liquid electrolytes, and conducting electrons and heat. However, there is limited knowledge on how to systematically design and implement these materials in emerging RFB applications, leading to the repurposing of available materials that are not tailored for this system, i.e. porous carbon papers or felts. For optimal RFB performance, it is necessary to pretreat carbons prior to use to improve electrode wetting and enhance redox kinetics, yet the impact of thermal pretreatment on electrode properties and the correlation between these properties are not well defined, thus the subsequent influence on performance is nebulous. Gaining a deeper understanding of electrode properties and their influence on performance will enable targeted improvements to electrode platforms, allowing system-specific performance gains. Further, identifying essential electrode properties will guide the development of alternative electrocatalytic material that may enable new systems in which carbon is unstable or is not catalytically active.

In this thesis, I will discuss the impact of electrode treatments on RFB performance, combining experimental and computational approaches. First, I investigate the interrelated effects of thermal pretreatment on electrode properties and correlate the changes in these properties with performance. Surface functionalization, wetting, and surface area are identified as the key properties that influence electrode performance. Next, I specifically investigate the impact of

surface area on electrode performance. I show that, while thermal treatment adds a significant amount of physical surface area to the electrode, electrochemical species are unable to access a large fraction of this surface area. Further, I use a convection-reaction model to show that even when all surface area is accessible, there is a limit to the surface area that will improve electrode performance. This limit to "useful" surface area is dictated by rate of reaction and transport within the electrode. Finally, I investigate the viability of nickel metal electrodeposition on carbon electrodes to enhance the performance of a novel polysulfide-permanganate flow battery. I show that nickel-deposited carbon electrodes outperform commercially available metal materials, including foams and weaves. The overarching goal of this thesis work is to develop a deeper understanding of the influence that electrode properties have on performance. By continuing to characterize the fundamental kinetic and transport properties within complex porous materials under forced convection, the community will be prepared to design novel material sets well-suited for use in RFBs and other challenging electrochemical environments.

Thesis Supervisor: Fikile R. Brushett

Title: Cecil and Ida Green Career Development Chair, Associate Professor of Chemical Engineering

Acknowledgments

Throughout my Ph.D. I have had the opportunity to work with incredible mentors and collaborators, as well as maintain a strong support network of friends and family. These people made the pursuit of my Ph.D. possible, and I am very grateful for everything they have provided for me.

I want to thank my research advisor, Fik, for guiding both my research and my professional development over the past five years. I have learned to tackle deep, intangible problems unflinchingly and with excitement. I would also like to thank my thesis committee members, Bill and Paula, for their encouragement and guidance. I feel fortunate to have developed a relationship with both outside of my committee meetings. Bill, thank you for your technical guidance on electrolyte transport, as well as mentorship in written scientific communication. Paula, thank you for your leadership as department head, I am happy to have worked with you as part of the graduate women's group to make the department a more inclusive and friendlier environment.

A huge thank you to the Brushett Research Group, which made coming in to work every day fun, even when my research projects were frustrating or discouraging. I am confident that the warm, inclusive environment that has developed in the group will continue long past my tenure. Thank you to my friends and family, who supported me throughout my Ph.D. journey. To my friends from UMass, thank you for being an amazing support network and cheering me on every step of the way. Your excitement and encouragement constantly remind me of how fortunate I am to have the opportunity to pursue a Ph.D. at MIT, even when the going got tough. To my friends I met in Boston, both in and outside of MIT, thank you for inspiring me every day with your passion and for broadening my perspective. I have experienced many exciting firsts with you, including climbing, skiing, and swimming with (whale) sharks, just to name a few. To my family, thank you for your unwavering support. You never stopped believing in me, thereby compelling me to believe in myself.

Table of Contents

List of Figures

List of Tables

I.   Introduction

Stationary energy storage technologies have the potential to facilitate the transition to a sustainable and reliable energy economy with high fractions of low-carbon variable energy resources.[1] Redox flow batteries (RFBs) are an attractive option as the flexible and scalable system architecture offers a pathway to low-cost, long-duration energy storage;[2–6] however, current RFBs are considered too expensive for widespread adoption.[7] Advances in the design and engineering of the electrochemical stack may enable cost reductions for multiple redox chemistries. Electrodes are a principal component of the individual flow cells of which the stack is comprised and are thus a target for further development, as they are responsible for several critical functions in the battery including distributing reactants, providing catalytic sites for reactions, and conducting electrons and heat.[8] Current generation flow battery electrodes are carbon papers, typically composed of polyacrylonitrile (PAN)-based carbon fibers which are woven together or are held together with an epoxy-like binder.[9] These carbon fiber electrodes are designed for use as the fibrous backing of gas diffusion layers in polymer electrolyte fuel cells and must provide several critical functions in that system, including distribution of gas reactants, removal of liquid water product, provision of mechanical integrity to cushion membrane volume changes, and conduction of electrons and heat. While functional for use in RFB systems, they are not designed to meet all RFB requirements (e.g., uniform liquid electrolyte distribution, wetting to electrolyte, high surface area for electrochemical reactions).[10] Thus, electrodes are typically modified prior to use in RFBs to improve performance.

1.   Thermal pretreatment to improve electrode performance

In 1992, Skyllas-Kazacos and coworkers published one of the first reports on electrode pretreatment for VRFBs.[11] Specifically, they investigated the impact of thermally oxidizing graphite felt electrodes at different temperatures (200, 300, 400, and 500 °C) for a set time of 30 hours and found that the electrode resistance is minimized at 400 °C, which also corresponded to the best cell performance. In subsequent years, thermal pretreatment strategies have been widely adopted and extended to other carbonaceous electrodes, including papers, and while all reported pretreatments lead to performance improvements, thermal oxidation is known to alter multiple electrode properties, and there is still ambiguity as to which of these properties is responsible for the observed enhancements.[11–18] The authors of these studies have attributed improved electrode performance to either increased activity due to surface functionalization by oxygen or other groups[11–17] or due to greater graphitic edge site population.[15,18] Higher electroactive surface area[12–

[14,17] and improved wettability[18] have also been cited. Moreover, it remains unclear whether one effect dominates, or a combination of properties is responsible for the augmented performance. This lack of understanding is limiting progress in flow battery research; indeed, if key properties could be identified and modified in a deliberate fashion, electrode performance could be dramatically enhanced. However, developing a thorough understanding is challenging as many properties are interrelated (e.g., electrochemically active surface area and wetting), and each property has a different dependence on pretreatment temperature. This range of outcomes may be a result of experimental design factors that complicate analysis, including the manufacturer-specific properties of electrodes (i.e., differences in binder content, graphitization temperatures, etc.) and the choice of redox electrolytes (i.e., redox couple, supporting salt, solvent). Thus, there is a need for systematic studies of different material sets to develop a more complete understanding of how the structural properties of electrodes impact their electrochemical performance in a given redox electrolyte.

2. *Metal electrodes for novel redox flow battery chemistries*

Carbon electrodes are the standard for RFB systems due to their low cost, high electrical conductivity, and high chemical and mechanical stability[8]; however, these electrodes exhibit low kinetic activity in many electrolyte systems, most notably the state-of-the-art vanadium redox flow battery.[9] Electrode treatment methods (including thermal treatment) can successfully activate carbon electrodes and overcome these disadvantages, yet these methods are difficult to scale, require batch processing, and often involve energy-intensive heating.[19] Although the mechanical, thermal, and electrochemical stability of oxidized carbon materials is not well understood, it is vital to the success of long-term battery operation.[8]

Metal electrocatalysts are one possible alternative to carbon. Metals have been incorporated into electrode platforms via a variety of fabrication methods, including electrodeposition, electrospinning, and impregnation/drying.[19] Electrodeposition is advantageous over other fabrication methods, as the thickness, mass, and surface structure of the metal catalyst may be controlled via deposition parameters, including deposition time, current, and electrolyte composition.[20] Further, the electrodeposition process is easily scalable and does not require any post-treatment steps, making it ideal for large-scale electrode production.[21] Metal electrocatalysts have the potential to significantly improve standard electrode performance—for example, electrodes utilizing precious metal catalysts have been shown to be augment the vanadium redox

reaction.[22] In fact, the majority of papers published which investigate the use of metal electrodes in RFBs focus on vanadium systems.[19] However, metal catalysts have been shown to augment other redox reactions of interest, including polysulfide;[23] hence metal electrodeposition may be used as a tool to augment performance of these novel redox electrolytes, particularly for kinetically limited redox couples, increasing their commercial viability.

3.   *Outline of thesis document*

The contents of **Chapter I** serve to provide a summary of current generation electrodes, including pretreatment techniques and the need to further understand the impact that thermal treatment has on electrode properties. I also discuss metal as an alternative electrode material and describe potential avenues for synthesis of next-generation metal electrodes. In **Chapter II** I present an overview of the effect that thermal pretreatment has on electrode properties and study the resulting influence on electrode performance. First, I thoroughly characterize surface functionalization, wetting, and surface area of carbon paper electrodes via *ex-situ* characterization techniques. Then, I analyze how each of these properties impacts *in-situ* electrode performance via full flow cell testing. In **Chapter III** I dive deeper into the relationship between physiochemical electrode properties and attempt to isolate the impact of surface area on electrode performance. I show that, while thermal treatment adds a significant amount of physical surface area to the electrode, electrochemical species are unable to access a large fraction of this surface area. In **Chapter IV** I describe the development of a convection-reaction model that I use to further elucidate the impact of surface area on electrode overpotential, assuming all of the surface area is accessible. I illustrate that regardless of accessibility, increasing surface area is not an effective method of improving RFB performance, and argue that the focus of future electrode improvements should be catalysis and mass transport. In **Chapter V**, I broaden the electrode material set under investigation to include metals, and describe an metal electrode synthesis process which involves depositing nickel metal on a carbon scaffold. I also show performance of these nickel-deposited electrodes in a polysulfide-permanganate redox flow battery, a new technology under investigation in the Brushett research group. In **Chapter VI,** I conclude by providing some perspective on why understanding the physical mechanisms at play within the electrode is necessary for upgrading, designing, and synthesizing next-generation RFB electrodes. I also discuss how the research thrusts in this doctoral work might be continued in the future, not just for RFBs but for any electrochemical system that utilizes porous electrodes.

II. Understanding the Effect of Thermal Pretreatment on Electrode Properties and Flow Cell Performance

Thermal oxidation of carbon electrodes is a common approach to improving flow battery performance. Here, we investigate the various property changes that occur as a result of thermal pretreatment, and the corresponding effects of pretreatment on flow cell performance. Specifically, we characterize the properties of Sigracet 29AA (SGL 29AA) carbon paper electrodes, under varying pretreatment temperatures (400, 425, 450, 475, and 500 °C) for 30 hours. We evaluate changes in the physical, chemical, and electrochemical properties of the electrodes using a suite microscopy, spectroscopy, and electrochemical characterization techniques. We find that as pretreatment temperature increases, some properties that we would expect to correspond to performance improvements (i.e., oxygen content, hydrophilicity) increase as pretreatment temperature increases, while other properties (i.e., mass/surface area) decrease with increasing pretreatment temperature. We subsequently explore the impact that these trade-offs have on electrode performance by testing each pretreated electrode in a vanadium redox flow battery (VRFB). We find that initially, increasing pretreatment temperature improves electrode performance—electrodes treated at 475 °C were found to be optimal with an increase in maximum power density of 26% over electrodes treated at 400 °C. However, electrodes treated at 500 °C were found to have worse performance than pristine electrodes. This shows that electrode performance is optimized when properties are balanced, and there is not necessarily one property that is more important than the others. Ultimately, this work aims to provide a guide for changes in electrode properties that may occur as a result of thermal treatment, and to understand the impact that these properties have on electrode performance.

1. Background

Developing electrochemical reactors with increased power output, reduced size, and high roundtrip efficiency represents a promising pathway for lowering RFB system costs. VRFBs, and indeed most RFB systems, utilize porous carbon electrodes based on three-dimensional fiber beds, most commonly polyacrylonitrile (PAN)-based graphite felts (> 5 mm) or carbon papers (~200 μm).[9] While, historically, graphite felts have been the preferred electrode material, emerging engineering advances in both the peer-reviewed literature[24,25] and industry[26] have shown the combination of thin carbon paper electrodes and structured flow fields dramatically increases

VRFB power output. However, charge-transfer overpotentials, due to slow vanadium redox reaction rates on carbon electrodes, remain a key performance limitation.[27] Current-generation carbon electrodes are typically modified prior to use in RFBs to improve performance. In 1992, Skyllas-Kazacos and coworkers published one of the first reports on electrode pretreatment for VRFBs.[11] Specifically, they investigated the impact of thermally oxidizing graphite felt electrodes at different temperatures (200, 300, 400, and 500 °C) for a set time of 30 h and found that electrode resistance is minimized at 400 °C, which also corresponded to the best cell performance. In subsequent years, thermal pretreatment strategies have been widely adopted and extended to other carbonaceous electrodes, including papers, and while all reported pretreatments lead to performance improvements, thermal oxidation is known to alter multiple electrode properties and there is still ambiguity as to which of these properties is responsible for the observed enhancements.[11–18] Authors have attributed improved electrode performance to either increased activity due to surface functionalization by oxygen or other groups.[11–17] or due to greater graphitic edge site population.[15,18] Higher electroactive surface area[12–14,17] and improved wettability[18] have also been cited. Moreover, it remains unclear whether one effect dominates or a combination of properties is responsible for performance enhancements. This lack of understanding is limiting progress in vanadium flow battery research; indeed, if key properties could be identified and modified in a deliberate fashion, electrode performance could be dramatically enhanced. However, developing a thorough understanding is challenging as many properties are interrelated (e.g., electrochemically active surface area and wetting), and each property has a different dependence of pretreatment temperature.

Here, we systematically study the impact of thermal oxidation on SGL 29AA carbon paper electrodes leveraging an array of electrochemical, spectroscopic, and microscopic methods, culminating with full cell testing, to identify temperature-dependent trends of performance-controlling electrode properties. By correlating *ex-situ* characterization with *in-situ* flow cell testing, we are able to identify how various chemical and physical properties of electrodes, including hydrophilicity, electrochemical surface area, and surface chemistry, contribute to overall performance and how these properties vary with pretreatment temperature. We identify the optimal pretreatment for SGL 29AA carbon paper electrodes is 475 °C, and treating electrodes at this temperature results in an increase in maximum power density of 26% over the commonly implemented base case of electrodes treated at 400 °C. This enhancement is achieved by a balance

of critical properties described above, rather than an improvement of all. This work represents the first step towards developing deterministic methods for modifying electrode microstructure and surface chemistry to augment performance and durability. The fundamental relationships we have identified, which were previously unknown to date due to the lack of systematic investigations in flow battery electrode literature, will play a central role in designing advanced electrode for next generation flow batteries.

2. *Experimental methods*

2.1. Thermal oxidation of the carbon paper electrodes

Sigracet SGL 29AA electrodes (Fuel Cell Store, College Station, Texas, USA) were oxidized under air in a Barnstead Thermolyne Type 47900 box furnace at either 400, 425, 450, 475, or 500 °C for 30 h. During the pretreatment, the electrodes were placed on aluminum foil to prevent contamination, and care was taken to ensure individual electrodes did not overlap. Post-treatment, the electrodes were immediately removed from the oven and allowed to cool at room temperature on the lab bench, and stored in plastic containers under air. Care was taken to avoid damaging the electrodes during handling, particularly the electrodes treated at 500 °C which were very fragile.

2.2. Characterization of electrode properties

Prior to cell testing, the electrodes were characterized with microscopic, tomographic, spectroscopic, and analytical techniques. Electrode microstructure and morphology was characterized by scanning electron microscopy (SEM) / energy-dispersive X-ray analysis (EDX). SEM/EDX measurements were performed using a ZEISS MERLIN HR-SEM (Jena, Germany) with an electron energy of 3 keV, an aperture of 30 μm, and a gun-to-sample distance of ca. 5 mm. The samples were adhered to the stage with double-sided conductive carbon tape (Ted Pella Inc.). The results were analyzed using SmartPI software (Zeiss, Jena, Germany).

The mass lost during thermal oxidation was determined at each temperature, by weighing the electrodes before and after treatment, and the average areal density was calculated by dividing by the geometric area (2.55 cm^2). The electrodes were weighed using a XS205 Mettler Toledo balance (0.1 mg uncertainty) in an enclosed scale in an argon atmosphere glovebox (PureLab HE Glovebox, Inert Technology, Amesbury, MA) with < 5 ppm water and < 10 ppm oxygen to ensure dryness.

Raman spectroscopy measurements and subsequent data fitting were performed using a Renishaw Invia Reflex Micro Raman with WiRE (Wotton-under-Edge, Gloucestershire, UK). First order Raman spectra were recorded from wavenumbers of 650 to 3140 cm^{-1} and peaks were fit at wavenumber of 1332 and 1582 cm^{-1} to evaluate the intensity of the diamond (D) and graphite (G) bands, respectively, the ratio of which was used to evaluate the level of disorder.[28]

X-ray photoelectron spectroscopy (XPS) spectra were collected with a Thermo Scientific K-Alpha Plus XPS system (Thermo Fisher Scientific, East Grinstead, UK) and peak fitting was performed using the Avantage program. All samples were analyzed using a microfocused, monochromatized Al Kα X-ray source of 400 μm spot size, and a dual-beam flood source provided charge compensation. A 2×220 L s^{-1} Pfeiffer HIPACE 300 turbopump vacuum was employed for both the entry and analysis chambers. Survey scans from 200-800 eV were collected along with C1s (275-295 eV) and O1s (512-552 eV) narrow scans. The survey scan and narrow scans were repeated $5\times$ per sample and $10\times$ per sample, respectively, and then averaged to generate the presented spectra. Two samples were analyzed per pretreatment temperature and two different spots on each sample were scanned.

Electrode capacitance was used as an approximate measure of electrochemically active surface area and was determined by performing cyclic voltammetry (CV) on a single electrolyte flow cell configuration containing pretreated electrodes and using a blank electrolyte of 2.6 M polysulfideic acid (H_2SO_4, 95.0-98.0 w/w %, Sigma Aldrich) flowing at 10 mL min^{-1}. Specifically, in this configuration, the electrolyte stream first passed through the positive half-cell and the directly looped through the negative half-cell.[29] A Nafion 117 membrane (183 μm nominal thickness, Fuel Cell Store) was used as a separator and was conditioned by soaking in the 2.6 M H_2SO_4 solution at ambient temperature > 24 h prior to use. Further details on flow cell assembly and operation can be found in the proceeding section. The capacitance was calculated from the slope of the linear relationship between capacitive current (A) and scan rate (V s^{-1}). Scan rates used were 5, 10, 20, 50, 100, and 200 mV s^{-1} and the cell voltage window was -0.3 to 0.3 V. To ensure ohmic losses did not convolute data analysis, iR_Ω-corrections were performed using the high frequency intercept of Nyquist plots derived from electrochemical impedance spectroscopy (EIS) measurements.[30] To isolate the electrode capacitance, the capacitance of a flow cell without electrodes was subtracted from the calculated capacitance of cells with each set of pretreated electrodes. Each capacitance measurement was repeated once.

Static contact angle measurements were performed with a Ramé-Hart Contact Angle Goniometer (Ramé-Hart Instrument Co., Succasunna, NJ). Specifically, a 2 μL water droplet was placed on the electrode surface and the apparent contact angle was determined through image analysis (ImageJ software). Contact angle was measured immediately after the droplet was placed on the electrode surface to ensure evaporation did not skew the results. When spontaneous imbibition occurred, videos of water droplet were also recorded at 30 fps using an Aven 26700-300 Digital Microscope (Aven Tools, Ann Arbor, MI) directly above the sample and captured images were processed post-test, using an ImageJ algorithm, to extract the rate of droplet spreading. Each measurement was repeated once.

2.3. Evaluation of electrode performance via flow cell testing

Electrochemical testing was performed in a 2.55 cm^2 zero-gap flow cell architecture with an interdigitated flow field at room temperature.[24,25] Tokai G347B resin-impregnated graphite plates of 3.18 mm thickness (Tokai Carbon Co., Tokyo, Japan) milled with an interdigitated pattern served as current collectors and flow fields, while polypropylene flow diffusers served as backing plates. Polytetrafluoroethylene (PTFE) gaskets (of thicknesses sized for each electrode) compressed electrodes by 20% and prevented electrolyte leaking. Two layers of carbon paper (1.5 cm × 1.7 cm) were used for each electrode, positive and negative. The electrodes were cut using a Silhouette Cameo tape cutter (Silhouette America Inc., Lindon, UT) to ensure dimensional uniformity. Pristine electrodes have a 190 μm thickness, and in the absence of compression thermally pretreated electrodes had thicknesses of 165-190 μm, measured using a dial thickness gauge (Mitutoyo, 500-195-30). As mentioned in section 2.1, electrodes pretreated at 500 °C were particularly fragile. A Nafion 212 membrane (50.8 μm nominal thickness, Fuel Cell Store), was utilized as a separator and was conditioned by soaking in 2.6 M H_2SO_4 solution at ambient temperature prior to use for > 24 h. During this pretreatment the membrane swelled to its wetted state; membrane thickness did not appreciably change, indicating that almost all swelling occurred in the in-plane direction. For all tests, electrolyte was pumped through the cell at a rate of 10 mL min^{-1} using a peristaltic pump (Masterflex L/S series model) and Norprene tubing (Masterflex L/S 14). All battery testing, with the exception of EIS measurements, was performed using an Arbin battery tester (FBTS-8). EIS was performed using a VMP3 Bio-Logic potentiostat (Bio-Logic USA, Knoxville, TN).

Prior to cell cycling, VRFB electrolyte solutions were prepared via electrolysis. The starting electrolyte in both tanks (10 mL in each) was 1.06 M $VOSO_4$ (VO^{2+}), from vanadium (IV) sulfate oxide hydrate (99.9% metals basis, Alfa Aesar), in 2.6 M H_2SO_4. Based on this electrolyte composition, the theoretical capacity of the cell is 284 mAh, and assuming a nominal cell voltage of 1.4 V, the energy density is 14.9 Wh L^{-1}. Quantitative comparison of cell performance with previous literature is difficult given variations in electrolyte composition and flow rate as well as cell configuration. In general, our results for cell efficiency and capacity align with those reported for other high performance laboratory cells with similar material sets and operating conditions.[12,13,17]

Each electrolyte tank was actively purged with nitrogen to prevent chemical oxidation of the redox couples via exposure to oxygen. A potentiostatic precharge step was used wherein the cell was held at a potential of 1.9 V until the current dropped below 10 mA (ca. 3.9 mA cm^{-2}). During this step, the positive electrolyte was oxidized from VO^{2+} (V(IV)) to VO_2^+ (V(V)) and the negative electrolyte was reduced from VO^{2+} (V(IV)) to V^{3+} (V(III)) with a typical conversion efficiency of 100%. Subsequently, the VO_2^+ solution was replaced with a fresh 10 mL of 1.06 M $VOSO_4$ / 2.6 M H_2SO_4 solution and the cell was galvanostatically charged, at 100 mA cm^{-2}, until a cell potential again reached 1.9 V. At this point cell capacity was equal to the theoretical capacity of 284 mAh, indicating that all VO^{2+} was oxidized to VO_2^+ at the positive electrode and all V^{3+} was reduced to V^{2+} at the negative electrode, corresponding to 100% state of charge (SOC). The cell was then galvanostatically discharged, at 100 mA cm^{-2}, to 50% SOC for subsequent electrochemical testing.

Next EIS was performed at open circuit potential and 50% SOC to identify the kinetic, ohmic, and mass transport contributions to the total DC resistance of the flow cell. Frequencies from 1 MHz to 10 mHz were applied at 6 points per decade and an average of 5 measures per frequency were recorded. The sinus amplitude is 10 mV. Upon completion of EIS, discharge polarization curves were obtained by discharging the cell for 30 s at current densities varying from 25 to 500 mA cm^{-2} in increments of 25 mA cm^{-2}. Data was recorded every second, and data points from the last 10 s at each current density were used to quantify the degree of polarization to ensure the system was at steady state. After each discharge the cell was returned to 50% SOC by charging at 100 mA cm^{-2} for a set time that ensured coulombic balance.

A rate study was conducted by varying current densities from 50 to 200 mA cm^{-2} in increments of 50 mA cm^{-2}. The flow cells were cycled 5× at each current density, with the same current density

implemented for both charge and discharge. The long-term cycling stability of the flow cells was evaluated via galvanostatic cycling at 100 mA cm^{-2} for 40 cycles (ca. 1-2 days depending accessed capacity). In both cases, cut-off cell voltages were set at 1.7 V for charge to avoid the parasitic oxygen evolution reaction and 0.9 V for discharge. Coulombic efficiency of the cell is calculated as the ratio of discharge time to charge time. Voltage efficiency is calculated by dividing the average discharge voltage by the average charge voltage, and energy efficiency is calculated as the average discharge energy divided by the average charge energy. All flow cell experiments were repeated once.

3.   *Results and discussion*

3.1.   *Ex-situ* materials characterization

Ex-situ electrochemical, microscopic, and spectroscopic techniques were used to characterize the physicochemical properties of pretreated electrodes. The physical properties were assessed using SEM and XTM to qualitatively and quantitatively evaluate the microstructure, areal density to quantify mass loss, and capacitance to estimate electrochemically active surface area. The chemical properties were analyzed using Raman spectroscopy to determine nature of edge sites, XPS to determine surface chemical composition, and EDX to map the elemental distribution of the surfaces. In addition, the wetting properties were determined by a combination of static and dynamic measurements. When analyzed together, the effect of pretreatment on changes in physical and chemical properties, as well as the relationships between these properties, can be determined

3.1.1.   *Electrode morphology and microstructure*

Thermal pretreatment is expected to induce significant changes to the surface morphology and electrode microstructure due to oxidation of the constituent components (e.g., carbon fibers and binder). To this end, we quantify the temperature-dependence of electrode morphology, areal density, surface chemistry, and electrochemically active surface area. As shown in **Figure II-1**, SEM was utilized to qualitatively visualize the major structural changes occurring in the electrodes at two different magnifications, 250× to observe electrode pore structure and binder content and 5000× to observe individual fibers. Micrographs of the pristine electrode show the bed of carbon fibers held together by the binder. As pretreatment temperature increases, the binder content decreases due to oxidative decomposition to carbon dioxide and other volatile products. This

binder loss becomes clearly observable at 450 °C and, at 500 °C, the binder is almost completely removed leading to a very fragile electrode that is easily damaged by physical contact.
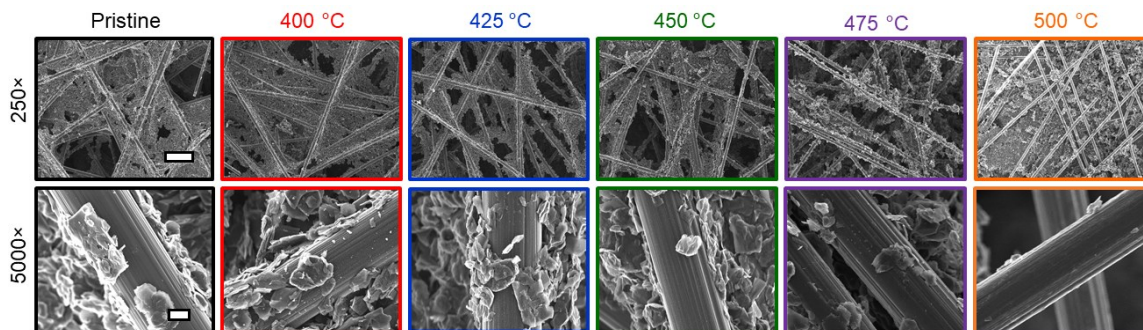
Figure II-1 *SEM micrographs of SGL 29AA carbon paper electrodes pretreated at different temperatures. The 250× magnification shows overall electrode structure (inset bar length = 2 μm), while the 5000× magnification shows morphology of individual fibers (inset bar length = 60 μm). At 500 °C, the sample holder is visible beneath the fiber bed due, in part, to the absence of the binder.*

To quantify binder removal during thermal pretreatment, we calculated the average areal density for each electrode (**Figure II-2**). We measured an areal density of 3.5 ± 0.1 mg cm^{-2} for the pristine SGL 29AA electrodes, which is somewhat lower than the vendor reported value of 4.0 mg cm^{-2}.[10] We ascribe this difference to batch-to-batch product variability and, as the same electrode sheet was used for all experiments, we anticipate that the trends are representative. While the areal density of pristine electrodes and those pretreated at 400 and 425 °C are similar, the density significantly decreases for electrodes pretreated at 450, 475, and 500 °C, in agreement with our observations of reduced binder content throughout the electrode structure via SEM. Additionally, as shown with SEM and XTM, the diameter of the carbon fibers is reduced during thermal treatment, so the loss in areal density is a result of both binder and fiber decomposition.
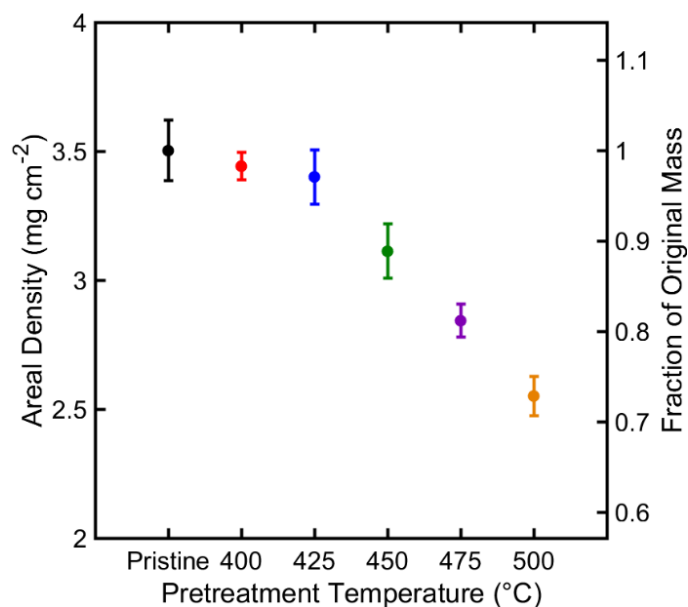
Figure II-2 *Average areal density of SGL 29AA carbon paper electrodes pre-treated at six different temperatures. The areal density shown is an average of six different samples pretreated at each temperature.*

Beyond changes to the electrode structure, thermal pretreatment impacts the electrochemically active surface area (ECSA) by exposing more active sites for redox reactions through removal of inert components in the binder and/or an increase in site accessibility due to increased hydrophilicity (see Section 3.1.4 below). Here, we used capacitance measurements to estimate ECSA (**Figure II-3**). The specific capacitance of SGL 29AA is unknown, so ECSA values for each electrode were estimated based on the measured capacitance, the areal density (see **Figure II-2**), and the specific capacitance of glassy carbon, 23 μF cm^{-2}, as reported by Sun *et al.*[31] As graphitic SGL 29AA and glassy carbon have different structure and surface functionalization, in all likelihood, they have different specific capacities, but we expect the observed trends to be representative. Moreover, we find good agreement with the results of Sun *et al.* who report an ECSA of 1.0 m^2 g^{-1} for pristine SGL 10AA carbon paper and 49.8 m^2 g^{-1} for enhanced surface area carbon paper, which was previously commercially available.[31] Here, we calculated an ECSA of 0.2 m^2 g^{-1} for pristine SGL 29AA carbon paper and 48.8 m^2 g^{-1} for electrodes treated at 400 °C. Electrodes pretreated at 400 °C have the highest ECSA, two orders of magnitude greater than that of the pristine electrodes. As the areal density of pristine electrodes is the same as electrodes pretreated at 400 °C (see **Figure II-2**), it is reasonable to assume that the electrode morphologies

are also similar and, therefore, the increase in ECSA can be attributed to a change in surface chemistry and related wetting properties. The capacitance of carbon electrodes has been shown to increase as a function of electrode wettability[32,33], which is typically due to the presence of oxygen functional groups on the electrode surface.[11] The capacitance of carbon electrodes is also known to improve with an increased number of graphitic edge sites.[32] Although electrodes pretreated at different temperatures likely have different specific capacities, we do not expect them to vary greatly as the Raman spectra indicates the ratio of graphitic edge sites to basal carbon is similar (within 10%) for all pretreated electrodes (see **Figure II-4**, *vide infra*). Similar content of graphitic edge sites indicates comparable capacitance, as graphitic edge sites dominate contribution to capacitance per Rabbow *et al.* who found that basal plane carbon has a specific capacitance of 4.7 $\mu F\ cm^{-2}$, and that the specific capacitance of graphitic edge sites is 132 $\mu F\ cm^{-2}$.[34] As such the increased presence of graphitic edge sites on heat-treated electrodes compared to pristine samples increases capacitance of these electrodes. While we find that number of edge sites increases with increasing pretreatment temperature and the specific capacitance of graphitic edge sites is two orders of magnitude greater than that of basal sites, electrode capacitance decreases as pretreatment temperature increases. This is a result of decreased binder content at higher temperatures. Specifically, as pretreatment temperature increases, the binder is oxidized and the total electrode surface area is decreased, leading to lower ECSA and hence reduced capacitance.
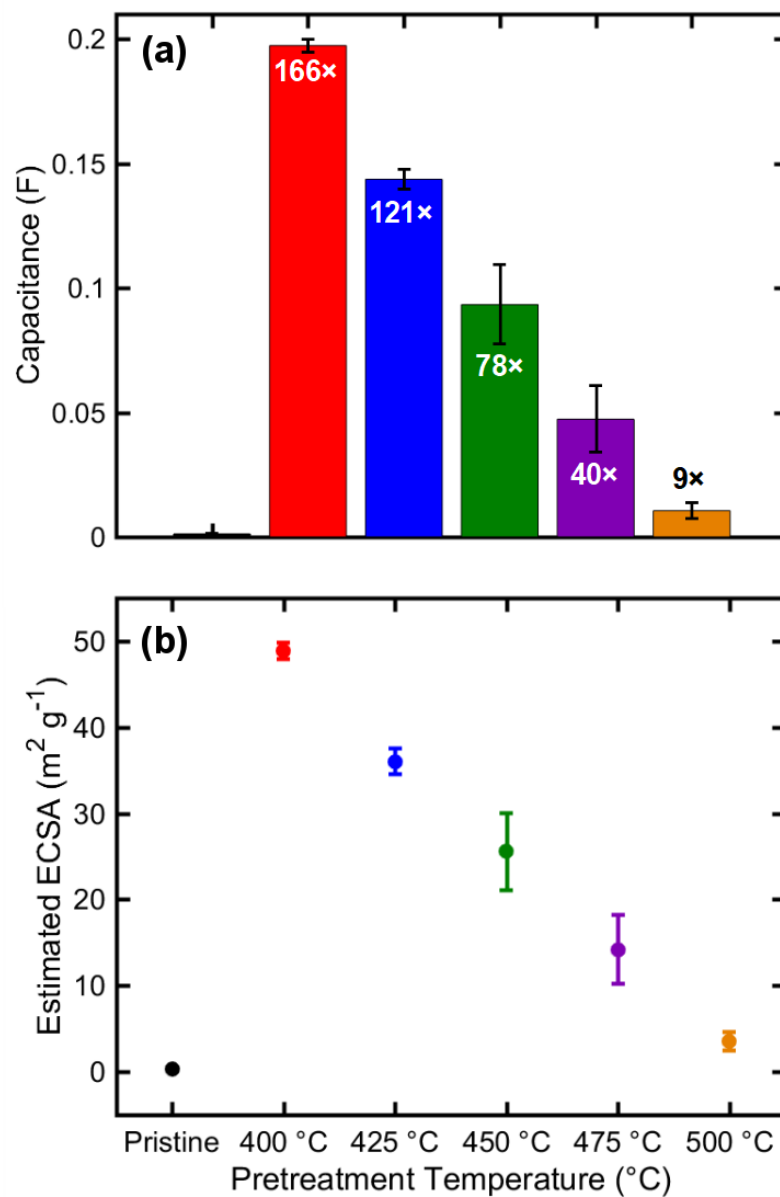
Figure II-3 *a) Electrode capacitance estimated from cyclic voltammetry measurements within a flow cell with a blank electrolyte of 2.6 M H_2SO_4. Measurements were repeated once for each pretreatment temperature. The numerical values within each bar represent increase in capacitance as compared to the pristine electrodes. b) ECSA estimated from measured capacitance using the respective electrode areal densities and the specific capacitance of a glassy carbon surface.*

3.1.2. Analysis of Surface Chemistry

Thermal pretreatment also affects the bonding structure of electrode surfaces which, in turn, impacts electrochemical behavior. Raman spectroscopy was used to evaluate the disorder of the

graphic carbon electrodes, and to quantify the presence of graphitic edge sites (**Figure II-4**). In addition to having higher specific capacitance, as discussed above, graphitic edge sites have been reported to catalyze vanadium redox reactions at both the positive and negative electrode[35–40], thus electrodes with higher I_D/I_G ratios are expected to lead to better VRFB performance due to a decrease in charge-transfer overpotential. An additional consideration is that edge sites have a higher probability of incorporating surface oxygen functional groups which are believed to catalyze vanadium redox reactions.[37] **Figure II-4(a)** shows the Raman spectrum of a pristine SGL 29AA electrode with the D band and G band peak fitting.[28] The D band is ascribed to the presence of a disordered graphitic edge lattice, while the G band is assigned to the ordered graphitic domains.[15,41] I_D corresponds to the intensity of the D band, while I_G corresponds to intensity of the G band. **Figure II-4(b)** shows the calculated I_D/I_G ratio of electrodes at each pretreatment temperature which provides a measure of the defects at the surface of the carbon fibers.[36,42] As compared to the pristine samples, all pretreated electrodes show an increased level of disorder with a maximum at ca. 425 °C. Due to the heterogeneity of the material, which is composed of carbon fibers and binder, the information obtained from peak intensity is related to the presence and molecular structure of these constituents. As shown by the areal density measurements (**Figure II-2**), the electrode mass does not significantly decrease at T < 450 °C. In this range, the increase in oxygen content (**Figure II-5**) explains the increase in molecular disorder. At higher temperatures (T > 450 °C), notable decomposition, preferentially of the binder, occurs and the weight fraction of carbon fibers dominates over that of the binder. Consequently, the average molecular disorder of the surfaces decreases, despite the increase in oxygen functionalities, as the sp^2 hybridization of the carbon fibers is more ordered than the amorphous binder particulates.
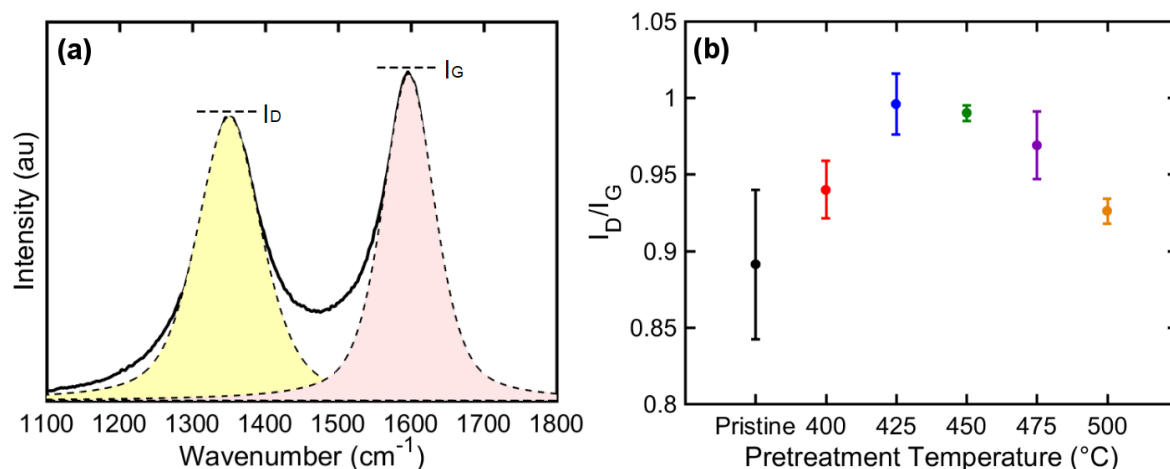
Figure II-4 *(a) Raman spectra of pristine SGL 29AA electrodes. Peak fitting of the D and G bands is shown. (b) I_D/I_G ratio of electrodes pre-treated at different temperatures. Spectra were recorded at three locations on two different samples for each pretreatment temperature.*

The nature of surface bonding can be further understood by determining the chemical changes to the electrode surface through the formation of oxygen functional groups which have been reported to catalyze vanadium redox reactions[15,36,37,43] as well as to increase the hydrophilic character of carbon surfaces.[11,14,38] We utilized XPS to quantify the concentration of oxygen functional groups on electrode surfaces as well as EDX to evaluate oxygen content on a single fiber. XPS analysis in **Figure II-5(a)** shows a growth of the O1s peak at 585 eV with pretreatment temperature, indicating increased presence of surface oxygen functional groups. The O1s peak is barely discernable in pristine electrodes, but becomes more prominent in the thermally oxidized electrodes, particularly those pretreated at 475 and 500 °C, indicating that thermal pretreatment causes carbon oxidation and the addition of surface oxygen groups, in agreement with prior reports.[11,12,15] As seen in **Figure II-5(b)**, the overall trend observed is increasing pretreatment temperature results in an increased O/C atomic composition ratio. We find that O-C bonds are the predominant functional group present on the electrode surface and that the presence of these bonds increases with thermal pretreatment temperature compared to pristine electrodes; in agreement with prior reports.[11,16,17,36,38] We also observe that pretreatment leads to the addition of carboxyl and carbonyl bonds, but there is no clear trend with pretreatment temperature.
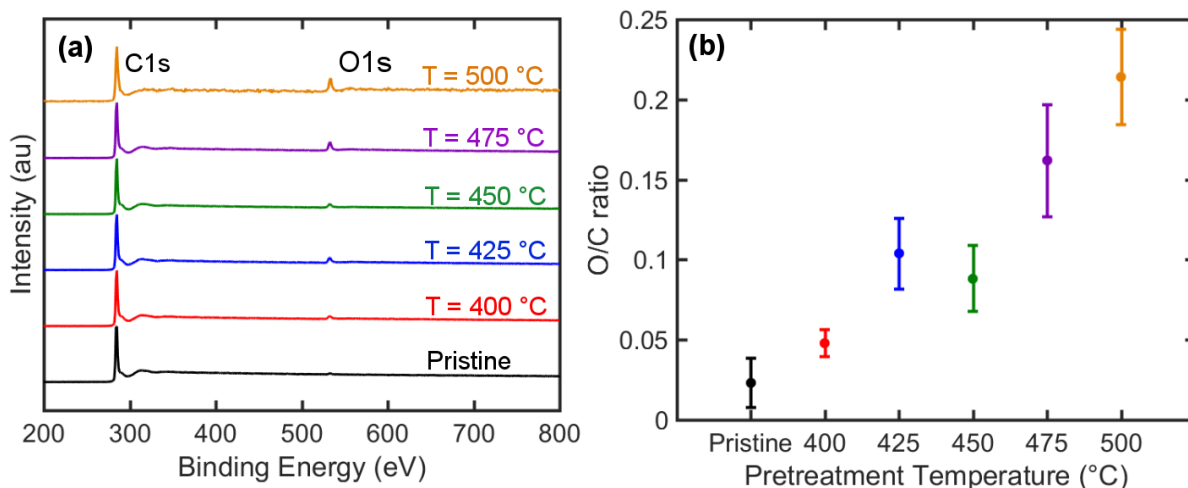
Figure II-5 (a) *XPS survey scans of SGL 29AA carbon papers. C1s and O1s peaks are labeled. (b) O/C atomic composition ratio calculated from survey scans. Measurements were performed on two samples pretreated at each temperature at two locations on each electrode.*

To compare local oxygen concentration on the surface of the binder and fibers of the SGL 29AA electrodes, EDX was used to measure the O/C ratio of electrodes treated at 400 °C. As seen in **Figure II-6**, oxygen content is more abundant on the binder than the fiber itself which can be explained by the differences in the chemical composition of the precursors used to generate each material. The precursor for the SGL 29AA carbon fibers is PAN, whereas the binder is derived from a proprietary carbonized resin.[10] This result highlights an interesting discrepancy: namely, the oxygen content of the binder is greater than that of the fiber, but electrodes pretreated at 500 °C have the least amount of binder as determined by areal density and SEM measurements (**Section II.3.1.1**) yet they have the highest oxygen content, as determined by XPS (**Figure II-5**). This indicates that the oxidation of carbon fiber surfaces via pretreatment results in a greater number of surface oxygen functional groups than are initially present on the surface of both the binder and the fibers.
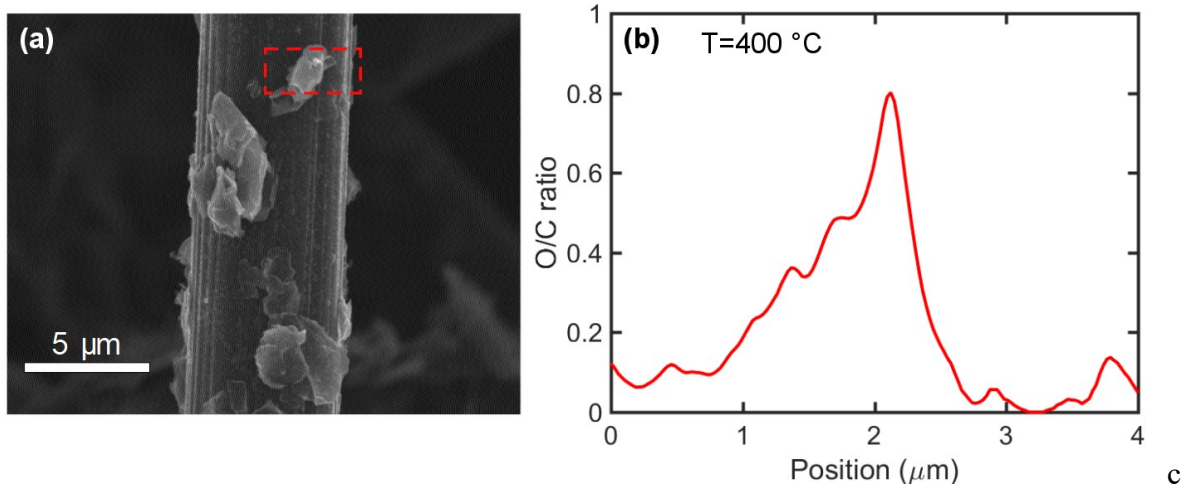
Figure II-6 *EDX elemental mapping of a carbon fiber surface treated at 400 °C. (a) SEM micrograph of the fiber partially coated with the binder. The area probed via EDX is highlighted in red. b) Measured O/C ratio with position.*

3.1.3. Electrode wetting

Pristine carbon fibers display near neutral wetting character with contact angles around 80-90º [44,45]. As wetting affects electrolyte transport and electrode utilization (accessibility to active sites),[33] increasing hydrophilicity is an important step to improving performance. To investigate the relationship between pretreatment temperature and electrode wetting, *ex-situ* wetting properties of water on the external surface of the carbon paper electrodes were studied using a goniometer to measure the static contact angle (**Figure II-7(a)**). As the surfaces are textured and heterogeneous, apparent contact angles, which can differ from intrinsic contact angles, are defined between water and the electrodes. If the paper spontaneously imbibed the water, the radius of the imbibed droplet was measured as a function of time to determine spreading rate (**Figure II-7(b)**), as this provides an indirect means to assess the intrinsic contact angle. Through this analysis the hydrophilicity of each pretreated electrode can be compared.
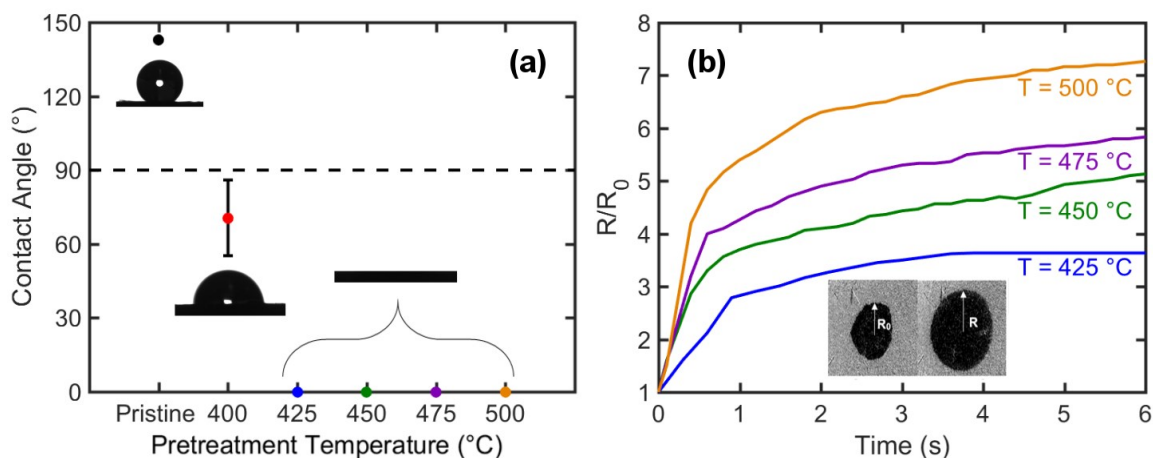
Figure II-7 *(a) Static contact angle of 2 μL water droplet on carbon electrode surface. Contact angle of three separate water droplets, each on a different electrode, were measured. (b) Dynamic wetting of spontaneously imbibed water droplets.*

Water droplets deposited on pristine papers and papers pretreated at 400 °C stayed on the surface. Droplets on pristine papers show hydrophobic behavior as the measured apparent contact angle was 140.0 ± 0.1°. Droplets on 400 °C electrodes show a hydrophilic apparent contact angle of 72 ± 15°, but water did not spontaneously imbibe. Electrodes pretreated at temperatures greater than 400 °C spontaneously imbibe water, thus, to obtain a semi-quantitative comparison, we measured the spreading dynamics, which increase with increasing pretreatment temperature indicating enhanced hydrophilicity (**Figure II-7(b)**). This trend can be explained as: (1) the intrinsic contact angle decreases as a function of the pretreatment temperature and consequent oxygen content increase, and (2) the binder removal at elevated temperatures reduces the possibility of retaining trapped air pockets within the electrode (i.e., the Cassie-Baxter effect). In a flow cell, faster wetting dynamics correspond to more complete electrode wetting; yet all electrodes pretreated at 425 °C and above are likely to wet fully during flow battery operation. Pristine papers and those pretreated at 400 °C may not wet completely in a flow cell, leading to decreased electrode utilization and hence decreased cell performance. Incomplete wetting, due to insufficiently low contact angle and surface roughness, could result in coexistence of gas and liquid within the electrode, leading to capillary forces that cause preferential liquid channeling.[44,46,47]

3.2. Cell performance

In the preceding sections, *ex-situ* techniques were used to characterize the pretreatment-induced changes in electrode morphology, microstructure, and surface chemistry. In the following section we utilize *in-situ* flow cell testing to assess the impact of these electrode properties on RFB performance, including cell resistance, power output, and cycling stability. Cell resistance and power output were assessed with a combination of EIS and polarization techniques. Cycling performance was evaluated at a range of current densities from 50-200 mA cm^{-2}, and cycling stability was assessed with constant current cycling at 100 mA cm^{-2}.

3.2.1. *Cell polarization and electrochemical impedance spectroscopy*

Polarization and EIS were used to evaluate the resistive contributions of each electrode, which, in turn, were used to evaluate cell performance. **Figure II-8** shows the iR$_\Omega$-corrected discharge polarization and the actual power density curves (inclusive of ohmic losses) obtained at 50% SOC for flow cells as function of electrode pretreatment temperature. As discharge resistance should be minimized at 100% SOC and maximized at 0% SOC, 50% SOC was selected as it represents an average discharge resistance. The best cell performance is achieved with electrodes pretreated at 475 °C, a 26% improvement as compared to the base case (400 °C pretreatment), followed closely by electrodes pretreated at 450 °C. Cells with electrodes pretreated at 400 and 425 °C show similar performance which is lower than the 450 °C and 475 °C. Interestingly, cells with electrodes pretreated at 500 °C display the poorest performance, even lower than the pristine electrodes. These results are consistent with those of Sun *et al.*, as in that study the authors increased temperature in 100 °C increments observing a minimum resistance at 400 °C and a maximum resistance at 500 °C.[11] Thus, based on our *ex-situ* characterization data, peak electrode performance appears to be achieved through a balance of properties.

Through analysis of polarization and EIS measurements, we can begin to deconvolute contributions of charge and mass transfer resistance. At low current densities, the overpotential is dominated by charge transfer resistance, and, in this region, the slope of the polarization curve can be correlated to the kinetics of the vanadium redox reactions (**Figure II-8(a)**). Electrodes pretreated at 400-475 °C show enhanced kinetic performance, as their slopes are shallow in the low current density region. Thus, observation is in agreement with prior literature which reports thermal pretreatment results in reduced cell overpotential.[12,15] Polarization of electrodes pretreated at 500 °C, however, has a steeper slope, indicating greater kinetic resistance. The interplay between

kinetic, ohmic, and mass transport resistance can be further characterized with EIS measurements (**Figure II-9**). The ohmic losses were determined with the high frequency intercept of the Nyquist plot and are found to be near identical for each cell, 0.25 ± 0.04 Ω-cm^2, in agreement with prior VRFB reports using similar flow cell configurations and membranes.[25,48,49] The Nafion membrane represents the greatest contribution to ohmic resistance. Tang *et al.* report a conductivity of 0.052 S cm^{-1} for Nafion 212 in a 1 M VO^{2+} / 5 M H$_2$SO$_4$.[50] Assuming this value for our cells, the membrane resistance was estimated as 0.1 Ω-cm^2, ca. 40% of total ohmic resistance. The remaining ohmic losses are attributed to resistive losses within the other cell components (e.g., porous electrodes, graphite flow fields, etc.) and electrical leads connected to the cell, as well as contact resistances between different internal and external components. No clear trend in ohmic resistance is observed as a function of pretreatment temperature.

To focus on kinetic and transport contributions, the ohmic resistance was subtracted in the iR$_\Omega$-corrected Nyquist plots derived from EIS at open circuit conditions and 50% SOC are shown in **Figure II-9**. The first (higher frequency) loop of the Nyquist curve corresponds to charge-transfer (kinetic) resistance, while the second (lower frequency) corresponds to mass transfer resistance.[51] The charge-transfer arc is much larger for the pristine electrode than any of the heat treated electrodes, which is expected as pristine electrodes have both the lowest ECSA and surface oxygen content. The combined kinetic and mass transfer resistances among pretreated electrodes are greatest for electrodes treated at 400 and 500 °C, while electrodes treated at 425, 450, and 475 °C show decreased total resistance. The kinetic resistance of electrodes pretreated at 425 to 475 °C are very similar, despite the reduction in ECSA as pretreatment temperature increases. This result can be explained as a balance between decreasing ECSA and increasing surface oxygen content, resulting in roughly equivalent charge-transfer overpotentials which is also supported by the polarization results. The increased charge-transfer resistance at 500 °C, despite the increased oxygen content, is a result of the greatly reduced surface area.
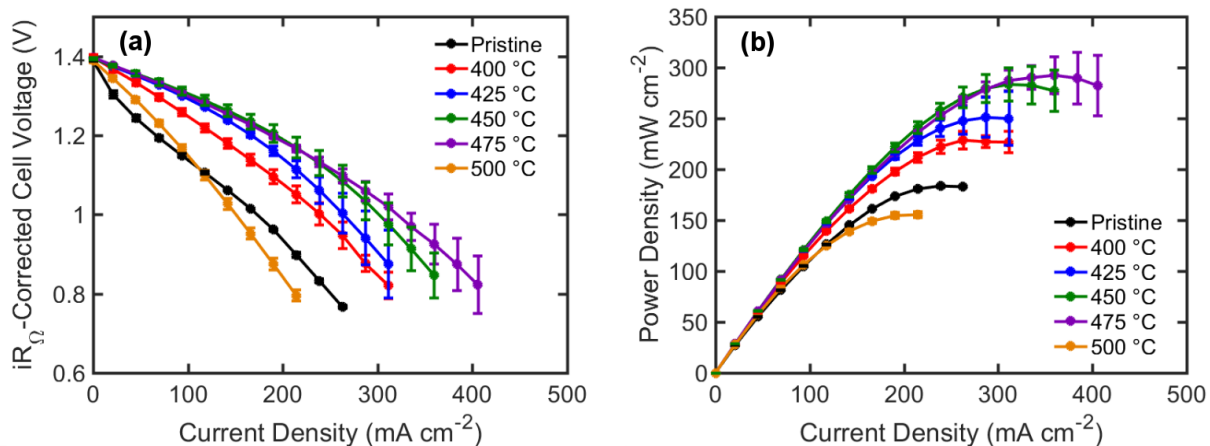
Figure II-8 *Polarization data of flow cells at 50% SOC with carbon paper electrodes pretreated at different temperatures. (a) iR_Ω-corrected voltage vs. current density (b) Actual (no iR_Ω correction) power density plotted as a function of current density. Data shown is an average of two experiments per pretreatment temperature.*
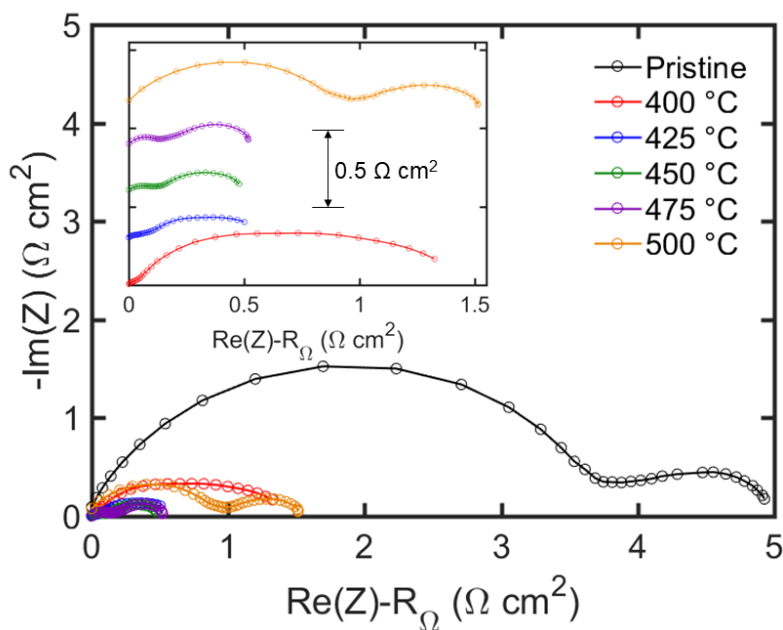
Figure II-9 *iR_Ω-corrected Nyquist plots of EIS data. The inset plot shows results from heat-treated electrodes only. Experiments were repeated once, and the spectra shown are representative of the two separate data sets.*

The reduced charge transfer resistance of the thermally-oxidized electrodes indicates faster vanadium reaction rates, but the source of these improvements may be the enhanced ECSA, an increase in surface-bound oxygen functional groups, or the presence of edge sites.[36] These effects are interrelated as, for example, more graphitic edge sites correspond to higher ECSA and more

35

surface oxygen. Prior studies have suggested that surface oxygen content plays a role in vanadium redox reactions[15,37,39,52–56], while others argue that the kinetic enhancement is due to the increased ECSA alone and the addition of oxygen functional groups are a side effect of the pretreatment that has little influence on reaction rate.[12,57] To determine the respective roles of ECSA and surface oxygen content on vanadium reaction rates, we estimated vanadium redox reaction rate on each electrode by fitting the low current density (< 50 mA cm^{-2}) region of the polarization curves to the Butler-Volmer equation and extracting an exchange current density. For these calculations, the error propagation considers all measured variables (e.g. ECSA, current density, voltage). Exchange current density of pristine SGL 29AA electrodes was calculated as 4.3×10^{-4} A cm^{-2} based on a geometric area. This result is the same order of magnitude as Zhong *et al.* who report an exchange current density of 2.47×10^{-4} A cm^{-2} for the VO_2^+/VO^{2+} redox couple on pristine graphite felt electrodes,[58] and Aaron *et al.* who report 1.49×10^{-4} A cm^{-2} for the V^{3+}/V^{2+} redox couple on pristine SGL 10AA electrodes,[59] each normalized by geometric area. It should be noted that the exchange current density calculated in this work contains information of both redox events as it is calculated assuming full cell voltage. The ECSA of an electrode provides a more accurate representation of current density but is more difficult to measure. The exchange current density (based on geometric surface area) of pretreated electrodes is a function of both ECSA and surface oxygen functional groups and follows a similar trend to the polarization and EIS data, with a maximum at 450 °C (**Figure II-10(a)**). Electrodes pretreated at moderate temperatures (425-475 °C) show the highest exchange current density, and therefore the best kinetic performance. Increased ECSA appears partially responsible for improved kinetics as the exchange current density shows a positive correlation with ECSA for electrodes treated at 500, 475, and 450 °C; however, electrodes treated at 400 and 425 °C have higher ECSA but reduced values for exchange current density. Thus, the estimated ECSA alone cannot explain the observed trends. The correlation between exchange current density (based on geometric surface area) and estimated ECSA (**Figure II-10(b)**) reveals an optimum around 23 m^2 g^{-1}, but the oxygen content is convoluted.

To obtain a more fundamental kinetic parameter, we converted the exchange currents estimated from Butler-Volmer to rate constants by dividing by the number of electrons transferred (here, n = 1), the Faraday constant (96485 C/mol e$^-$), the bulk concentration (0.53 M), and the estimated ECSA. Estimated rate constants were found in the range of $0.2 – 1.8 \times 10^{-9}$ m s^{-1}; these results are

comparable to the V^{4+}/V^{5+} rate constant on graphite electrodes of 3.0×10^{-9} m s^{-1} reported by Weber.[60] These estimated rate constants, kinetic parameters independent of ECSA, show a positive correlation with increasing O/C ratio (**Figure II-10(c)**). XPS data shows that oxygen functional groups also increase with increasing pretreatment temperature (see **Figure II-5**); overall, these results suggest that vanadium redox reaction rates on carbon paper electrodes improve with increasing surface oxygen functional content. However, increasing surface oxygen content via thermal treatment results in reduced ECSA, thus a trade-off exists between these two properties and electrodes treated at 450 °C show the best performance despite not having the maximum ECSA or surface oxygen content.
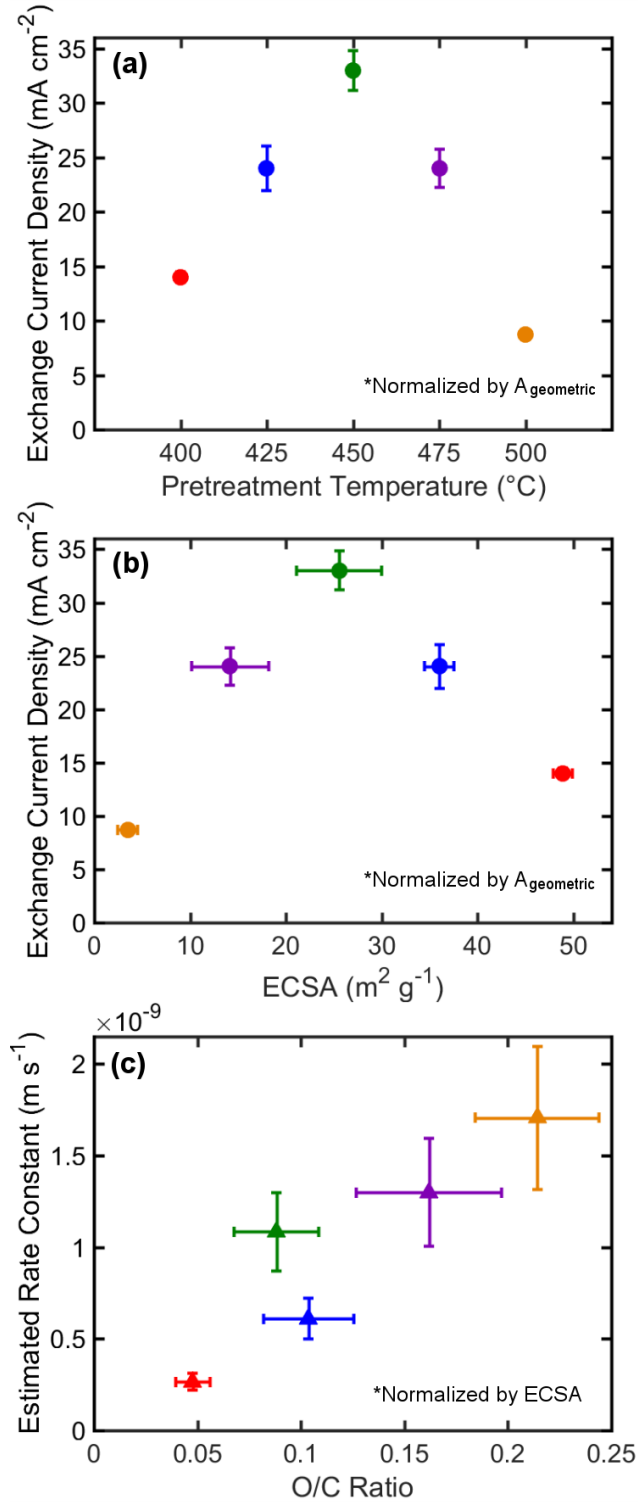
Figure II-10 *Estimates of kinetic parameters derived from a Butler-Volmer model estimating charge-transfer overpotential fitted to polarization data. (a) Exchange current density plotted as a function of pretreatment temperature. (b) Exchange current density plotted as a function of ECSA. (c) Estimated rate constant plotted as a function of relative oxygen content of the electrode.*

The lower frequency features of the Nyquist plot provide insight into mass transport within the porous electrode structure. The mass transfer resistance depends on the electrode microstructure (e.g., pore size, geometry, connectivity) and the fluid characteristics (e.g., flow rate, electrolyte viscosity): electrodes with pores of similar size will have comparable velocity profiles, resulting in similar momentum boundary layer thicknesses.[61] The mass transfer arc of the pristine electrode is approximately equal to that of 400 °C, indicating that these electrodes have similar mass transfer resistance and therefore equivalent morphologies (binder content) and electrolyte distribution. The mass transfer resistance of electrodes pretreated at 425-500 °C are near identical. In general, we find that electrodes that show spontaneous imbibition of water, those pretreated at 425-500 °C, have the lowest mass transfer resistances (electrodes treated at 475 °C have the lowest mass transfer resistance of 0.038 Ω-cm^2, while electrodes treated at 500 °C have the highest of this group of 0.053 Ω cm^2 likely due to loss of structural integrity). Resistance to wetting could lead to preferential paths for liquid flow within electrodes: such mass transport limitations have been observed via imaging[62] and exploited in the engineering of fuel cell GDLs.[63,64] Wetting resistance causes high capillary pressure[65] and preferential, tortuous pathways are defined as a consequence. Overcoming these barriers leads to increased resistance.

3.2.2. *Flow cell cycling performance*

To evaluate flow cell performance, we cycled cells utilizing each electrode at current densities varying from 50-200 mA cm^{-2}. Efficiencies and charge/discharge curves for a cell with electrodes pretreated at 475 °C are shown (**Figure II-11(a), (b)**). The performance stability suggests that the impact of the pretreatment is persistent, at least in the short term. Figure 12c shows the accessed capacity for cells with different heat-treated electrodes over a range of each current densities (**Figure II-11(c)**) Similar to the polarization curves shown before, electrodes at 400 and 500 °C show the lowest performance, while electrodes treated at 475 °C show the best performance. We note that the differences in accessible charge capacity are minimal at low current densities (i.e., 50 mA cm^{-2}), but become more pronounced at, at higher current densities (i.e., 150 mA cm^{-2}) as differences in charge transfer and mass transport overpotentials become more relevant. Pezeshki *et al.* found that as surface oxygen content increased, discharge capacity increased.[12] Our results agree with this prior report until electrodes pretreated at 500 °C which perform poorly, despite the highest O/C ratio. This is due to low surface area (charge-transfer resistance) and loss of structure (mass transfer resistance) which together lead to high cell resistance (see Section 3.2.1). These

results show heat pretreatment below 500 °C can improve performance, particularly at high current densities. It should be noted that pristine electrodes have not been included, as the extremely high overpotentials of these electrodes made cycling at moderate current densities difficult.
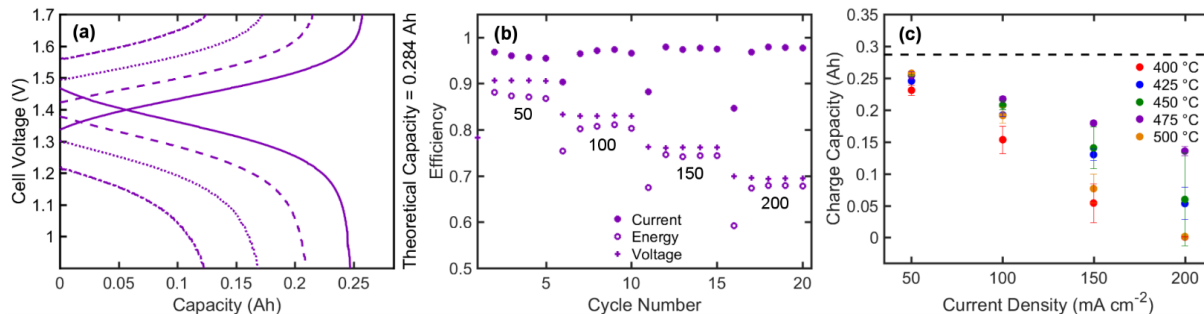
Figure II-11 *Performance of VRFB cells with for SGL 29AA electrodes at different current densities. (a) Voltage vs. capacity curves at each current density for electrodes pretreated at 475 °C. Data shown is from the fifth of five cycles at each current density. (b) Efficiencies of each cycle for electrodes pretreated at 475 °C (labeled current densities in mA cm^{-2}). (c) Average charge capacity at each current density for each set of electrodes. Two different cells were cycled with electrodes pretreated at each temperature. The pristine electrode is not included due to limitations in cycling caused by extremely high overpotentials.*

Flow cells were cycled at a constant current density of 100 mA cm^{-2} for 40 cycles (ca. 1-2 days) to assess the stability of the pretreated electrodes. The goal of this test was to compare efficiency and stability of the electrodes over several cycles. More extensive stability testing has been performed elsewhere[66] and is not the focus of this work. The average cycling efficiencies, including coulombic, voltage, and energy efficiencies, are shown in **Table II-1**. The efficiencies remain consistent throughout cycling: we achieve average coulombic efficiencies ranging from 98.2-99.4% and voltage efficiencies ranging from 64.9-84.1%, which are similar those reported elsewhere.[48,67,68] Voltage efficiency increases as pretreatment temperature is increased from 400 to 475 °C. At 500 °C, the voltage efficiency drops. These results agree with the increased overpotential losses of electrodes pretreated at this temperature as measured via polarization (see **Figure II-8(a)**). While all pretreated electrodes are found to be reasonably stable, all experienced some level of capacity fade, and this loss of charge capacity is most likely due to active species crossover through the semi-permeable Nafion membrane.[9,48,67,69,70] However, cell degradation such as the removal of surface oxygen active sites from the negative electrode, or negative electrolyte oxidation by oxygen in air, may contribute to capacity fade.[9,36,53,71–74] Quantifying the

extent of electrode degradation and its role in capacity fade is beyond the scope of the current work and will be the subject of future studies.

Quantitative comparison of cell performance with previous literature is difficult given variations in electrolyte compositions and flow rate, as well as cell configuration. In general, our results for cell efficiency and capacity align with those reported for other high performance cells.[12,13,17]

Table II-1 – Constant coulombic cycling efficiencies for each pretreated electrode. Cycling experiments were repeated once per each pretreatment temperature.

Pretreatment	Efficiency (%)		
Temperature (°C)	Coulombic	Energy	Voltage
400	98.31 ± 1.02	66.31 ± 1.53	67.47 ± 0.70
425	99.37 ± 0.31	77.41 ± 1.46	78.00 ± 1.23
450	98.96 ± 0.63	80.13 ± 2.33	81.07 ± 3.00
475	98.16 ± 0.50	77.49 ± 5.12	78.84 ± 4.74
500	99.41 ± 1.66	64.13 ± 7.62	64.94 ± 8.39

4.   Conclusion

Thermal oxidation offers a means to improve the performance of porous carbon electrodes in VRFBs but its impact on the physical and chemical properties of the electrodes are complex and nuanced. To better understand the temperature-dependent trends of performance-controlling electrode properties, we systematically studied the impact of thermal oxidation on SGL 29AA carbon paper electrodes leveraging an array of electrochemical, spectroscopic, and microscopic techniques, culminating with full cell testing. Through this approach, we identified several key electrode properties, including hydrophilicity, electrochemical surface area, and surface chemistry, which significantly impact on the cell performance but display opposing trends. Electrochemical surface area decreases as pretreatment temperature increases due to partial combustion of the electrode binder and fibers. Wetting dynamics are improved and surface oxygen content is higher at higher pretreatment temperatures. The best overall performance is achieved by thermally pretreating electrodes at 475 °C. These electrodes show an increase in maximum power density of 26% over the base case of electrodes treated at 400 °C. This enhancement is achieved by a balance of critical properties described above, rather than a maximization of all. In particular, we have

shown that oxygen content increases the overall rate constant and therefore contributes to a reduction in charge-transfer overpotential. Based on our findings, it is suggested that an optimal electrode should feature high ECSA and oxygen content to reduce charge-transfer resistance, facilitate spontaneous wetting to minimize mass transport resistance, and maintain a mechanically robust structure. The findings presented herein can be used to inform the design of advanced electrodes. These learnings do not only impact the redox flow battery community, but are also relevant for any electrochemical technologies employing porous carbonaceous substrates, including fuel cells, metal-air batteries, and electrolyzers. More generally, the results described here highlight the complex effects bulk pretreatments have on electrode materials and motivates the development of targeted methods, based on the structure-property relationships outlined here and elsewhere [11–18], to tune specific electrode characteristics, which may enable transformative performance improvements in RFBs and other electrochemical technologies.

III. Investigating Accessible Surface Area and the Impact of Surface Area on Redox Flow Battery Performance

Investigating Accessible Surface Area and the Impact of Surface Area on Redox Flow Battery Performance

Thermal oxidation of carbon electrodes is a common approach to improving flow battery performance. Here, we investigate how thermal pretreatment increases electrode surface area and the effect this added surface area has on electrode performance. Specifically, we rigorously analyze the surface area of Freudenberg H23 carbon paper electrodes, a binder-free model material, by systematically varying pretreatment temperature (400, 450, and 500 °C) and time (0 to 24 h) and evaluating changes in the physical, chemical, and electrochemical properties of the electrodes. We compare physical surface area, measured by a combination of gas adsorption techniques, to surface area measured via electrochemical double layer capacitance. We find good agreement between the two at shorter treatment times (0-3 h); however, at longer treatment times (6-24 h), the surface area measured electrochemically is an underestimate of the physical surface area. Further, we use gas adsorption to measure a pore size distribution and find that the majority of pores are in the micropore range (< 2 nm), and ca. 60% of the added surface area are in the sub-nanometer (< 1 nm) pore size range. We postulate that the solvated radii and imperfect wetting of electrochemical species may hinder active species transport into these recessed regions, explaining the discrepancy between electrochemical and physical surface area. These results are supported with *in situ* flow cell testing, where single-electrolyte polarization measurements show little improvement with increasing surface area. Ultimately, this work aims to inform the design of electrodes that offer maximal accessible surface area to redox species.

1. Background

As discussed in **Chapter II**, thermal oxidation in air augments electrode performance by enhancing electrochemical activity and wetting via surface functionalization[11–17] and by increasing available surface area via improved wettability and increased physical surface area.[12–14,17] However, these effects are difficult to decouple and, as such, it is often unclear to what extent each is responsible for performance improvements. Indeed, conflicting conclusions have emerged across the literature: improved electrode performance in RFBs has been attributed to increased

surface area,[12] increased oxygen functional groups[75,76], or a combination of both.[77–80] This range of outcomes may be a result of experimental design factors that complicate analysis, including the manufacturer-specific properties of electrodes (i.e., differences in binder content, graphitization temperatures, etc.) and the choice of redox electrolytes (i.e., redox couple, supporting salt, solvent). Thus, there is a need for systematic studies of different material sets to develop a more complete understanding of how the structural properties of electrodes impact their electrochemical performance in a given redox electrolyte.

Surface area is an important parameter for RFB electrodes, as increased surface area enhances volumetric redox reaction rates.[81] Accordingly, a number of sophisticated surface modification approaches have been described in the literature, including the introduction of nanocracks,[82] nanorods,[83] and nanowalls,[84] which enlarge the electrode surface area, measured by gas adsorption, by several orders of magnitude. However, the performance of flow cells with these materials is similar to that of flow cells with more conventional heat-treated materials, evincing a mismatch between surface area increases and performance improvements. This may be due to a disparity between physical surface area (specific surface area, SSA, m^2 g^{-1}) and electrochemically active surface area (ECSA, m^2 g^{-1}), defined as the surface area available to electrochemical species.[85,86] Taken together, these results suggest that not all the porosity—and therefore not all physical electrode surface area—is accessible to electrochemical species, and, in this work, we set out to explore this hypothesis.

To further study the nature of surface area generated via thermal pretreatment and to assess its role in electrochemical reactions, we investigated how thermal oxidation alters both SSA and ECSA, as well as other key electrode properties (e.g., functionalization, pore size distribution, and wettability). In order to separate these convoluting effects on cell performance, we selected a nonaqueous electrolyte ((2,2,6,6-tetramethylpiperidin-1-yl)oxyl (TEMPO•)/2,2,6,6-tetramethylpiperidin-1-yl)oxidanyl (TEMPO$^+$) in acetonitrile), which should thus be insensitive to surface functional groups and wetting effects, allowing study of the impact of surface area alone on electrode polarization performance. Freudenberg H23 was selected as a model binder-free electrode material to avoid the influence of extraneous and often poorly-understood binder materials and to enable focus on the effect of thermal pretreatment on the carbon fibers themselves. Surface area of the electrodes was compared with ECSA, estimated via electrochemical double-layer capacitance measurements, and by SSA, quantified based on krypton (Kr) and argon (Ar)

adsorption. Porosity on the fiber surface in the micropore (pores < 2 nm per IUPAC classification) and mesopore (pores between 2 and 50 nm) was measured with multiple probe molecules (Kr, Ar, carbon dioxide (CO_2) and hydrogen (H_2)) and using different models (BET, 2D-NLDFT). The macropore range (pores > 50 nm) was further measured by Mercury Intrusion Porosimetry (MIP). Surface functionalization and electrode wetting were assessed by X-ray photoelectron spectroscopy (XPS) and external contact angle measurements, respectively. Subsequently, pretreated electrodes were tested in a single-electrolyte flow cells with the TEMPO$^•$/TEMPO$^+$ redox couple to deconvolute effects of surface area and oxygen functionality.

Our analyses indicate that both ECSA and SSA of the electrodes are maximized at moderate pretreatment temperatures and times beyond which surface area reduces. Further, we find that thermally treated electrodes with increased surface area show improved performance over the baseline, but there are diminishing returns in surface-area-derived performance gains. We rationalized this observation with a simple convection-reaction model, which predicts a maximum current that may be achieved with increases in surface area (**Chapter IV**). These results indicate that surface area has an effect on electrode performance, but only up to a certain threshold, beyond which increasing surface area does not improve performance. Overall, we find that the mass transfer and redox reaction rates themselves have a greater effect on electrode performance than surface area. While the quantitative values revealed by this study (surface area, oxygen content, etc.) are specific to Freudenberg H23, we posit that the property-performance trends and trade-offs are anticipated to extend across carbonaceous electrode materials, although the pretreatment temperatures and times at which they occur will differ.[27]

2.   *Experimental methods*

2.1.   Thermal oxidation of Freudenberg H23 electrodes

Freudenberg H23 electrodes (Fuel Cell Store, College Station, Texas, USA) were oxidized under air in a Barnstead Thermolyne Type 47900 box furnace at either 400, 450, or 500 °C for varying times (0.5, 3, 6, 12, and 24 h for 400 and 450 °C, and 0.5, 1, 3, 4, and 5 h for 500 °C). Electrodes treated for more than 5 h at 500 °C lost a significant percentage of their mass and were too fragile to test. During the pretreatment, the electrodes were placed on aluminum foil to prevent contamination, and care was taken to ensure individual electrodes did not overlap. The electrodes were placed in the oven at room temperature, and temperature was ramped to the set-point at 20 °C min^{-1}. The oven temperature was then held at the set-point for the specified time. After thermal

pretreatment, the electrodes were allowed to cool to room temperature in the oven and were subsequently stored in sealed plastic containers under air.

2.2.   Characterization of electrode properties

2.2.1.   *Electrode weight, functionalization, and wetting*

Prior to cell testing, the electrodes were characterized with microscopic, spectroscopic, and analytical techniques. The mass lost during thermal oxidation was determined by weighing the electrodes before and after pretreatment, and the average areal density was calculated by dividing by the geometric area (2.24 cm^2, 1.4 cm $\times$ 1.6 cm). A Silhouette Cameo tape cutter (Silhouette America Inc., Lindon, UT) was used to ensure dimensional uniformity between samples. The electrodes ($n = 6$ per treatment condition) were weighed using a XS205 Mettler Toledo balance ($\pm$ 0.1 mg uncertainty). To compare wettability of treated electrodes, apparent external contact angles were measured with a ramé-hart Contact Angle Goniometer (ramé-hart Instrument Co., Succasunna, NJ). Measurements were taken in ambient air, where the temperature and relative humidity remained between 20-24 °C and 10-40%, respectively. Specifically, a 2-µL solvent droplet (either deionized (DI) water (18.2 MΩ, Milli-Q) or acetonitrile (99.9%, Extra Dry, ACROS Organic)) was placed on the porous electrode surface and an image of the solid-liquid-gas contact angle of the droplet on the surface was captured immediately to avoid significant solvent evaporation. The contact angle was estimated manually using ImageJ software. It should be noted that this measurement technique is qualitative and intended to comparatively evaluate wetting of different samples.

XPS spectra were collected with a Thermo Scientific K-Alpha Plus XPS system (Thermo Fisher Scientific, East Grinstead, UK) and peak fitting was performed using the Thermo Avantage software (version 5.9904, Thermo Scientific). All samples were analyzed using a microfocused, monochromatized Al Kα X-ray source of 400 µm spot size, and a dual-beam flood source provided charge compensation. A 2× 220 L s^{-1} Pfeiffer HIPACE 300 turbopump vacuum was employed for both the entry and analysis chambers. Survey scans from 200-800 eV were collected along with C1s (275-295 eV) and O1s (512-552 eV) narrow scans. The survey scan and the narrow scan were repeated 5× and 10×, respectively, per sample, and then averaged for the collected spectra. Two samples were analyzed for each pretreatment condition (temperature and time) and three different locations on each sample were scanned.

2.2.2. Characterization of surface area via capacitance

Electrode capacitance was used as an approximate measure of ECSA and was determined by performing cyclic voltammetry (CV) on a single electrolyte flow cell configuration (2-electrode setup) containing one heat-treated electrode per side and using a blank electrolyte of either 1 M polysulfideic acid (H_2SO_4, 95.0-98.0 w/w %, Sigma Aldrich) in deionized (DI) water (18.2 MΩ, Milli-Q) or 1 M tetraethylammonium tetrafluoroborate (TEABF$_4$, 99.45% purity, Gotion Inc., Fremont, CA) in acetonitrile (99.9% extra-dry, ACROS Organics) with a fixed pump flow rate of 7 mL min^{-1} (Masterflex L/S series), resulting in a superficial velocity of ~5 cm s^{-1}.[87] In this configuration, the electrolyte stream first passes through the positive half-cell and then immediately through the negative half-cell.[29] A Daramic 175 separator (175 μm nominal thickness, Daramic LLC, Charlotte, NC) was used as-received as a separator. A flow-through flow field configuration was used for capacitance measurements. All capacitance measurements were performed using a VMP3 BioLogic potentiostat (BioLogic USA, Knoxville, TN), and each test was repeated once. Further details on flow cell assembly and operation can be found in the following section (**Section 2.3**). The capacitance was calculated from the relationship in **Equation 1**:

$$i = C\frac{dV}{dt} \tag{1}$$

where i is the current density (A m^{-2}) determined by averaging the magnitudes of the positive current from the positive voltage sweep and negative current from the negative voltage sweep at a chosen cell voltage of 0 V, C is the areal specific capacitance (F m^{-2}), and dV/dt is the scan rate (V s^{-1}). The capacitance is calculated from a linear fit of the scan rate dependent capacitive current, and ECSA (m^2 g^{-1}) is calculated by normalizing the capacitance with the estimated specific capacitance of glassy carbon $C_{s,gc}$(aqueous) ≈ 0.23 F m^{-2} in 0.5 M H_2SO_4 / water (aqueous electrolyte)[88] and $C_{s,gc}$(nonaqueous) ≈ 0.18 F m^{-2} in 0.25 M TEABF$_4$ / acetonitrile (nonaqueous electrolyte)[89] and by the average electrode mass. Using the specific capacitance value of glassy carbon requires the assumption that the specific capacitance of the carbon fiber surface is similar, and that the specific capacitance is constant across thermally treated electrodes; however, it is likely that oxygen functional groups, as well as the micropores themselves, will influence the specific capacitance of the electrode material.[90] Hence the calculated ECSA values should not be interpreted at quantitatively absolute; however, this estimate is a useful way to compare accessible surface area of electrodes. Scan rates used were 5, 10, 20, 50, 100, and 200 mV s^{-1} and the cell

voltage range was from -0.3 to 0.3 V. To ensure that ohmic losses did not convolute data analysis, iR_Ω-corrections were applied by using the Biologic ZIR method at 85% compensation (with the remaining 15% compensated manually post-experiment).[30] To isolate the electrode capacitance, the capacitance of a flow cell without electrodes was subtracted from the calculated capacitance of cells with each set of pretreated electrodes. Each capacitance measurement was repeated once. To verify the accuracy of measuring capacitance with CV, we calculated the capacitance from electrochemical impedance spectroscopy (EIS) of the same cell set up with pristine electrodes and electrodes treated at 450 °C for 12 h, fitting a RC circuit. The resulting capacitances calculated from EIS and CV were in good agreement, with the pristine and pretreated electrodes showing differences of 4% and 6%, respectively.

2.2.3. *Characterization of surface area and pore size distribution via gas adsorption*

Gas adsorption measurements were performed on electrode samples treated at 450 °C to measure SSA and pore size distribution (PSD). A Micromeritics 3Flex surface characterization analyzer (Micromeritics Instrument Corp, Norcross, GA) was used for all measurements. Prior to measurement, the samples were activated under secondary vacuum at 110 °C for 12 h. Activation at 300 °C for 12 h was also performed for comparison and led to similar results, indicating that the outgassing procedure was efficient at both temperatures. Kr adsorption isotherms measured at 77 K (S_{BET}-Kr) and Ar adsorption isotherms measured at 87 K (S_{BET}-Ar) were collected and interpreted using multi-point Brunauer-Emmett-Teller (BET) analysis for surface area determination[91] over the range 0.06–0.20 relative pressure (P/P_0) and with Kr and Ar cross-sectional areas of 0.210 and 0.143 nm^2, respectively. Due to limitations in the amount of sample that could be loaded into the instrument as compared to the minimum amount of sample needed to obtain reliable data, Ar adsorption isotherms ($m_{sample} \sim 1$ g) were measured for samples presenting surface areas > 10 m^2 g^{-1}, whereas Kr adsorption isotherms ($m_{sample} \sim 60$ mg) were measured for all samples.

The SSA and PSDs were estimated from the analysis of Ar adsorption isotherms using the 2D-Non-Local Density Functional Theory model for carbon slit-shaped pores with heterogeneous surfaces (2D-NLDFT-HS), which has been successfully applied to various carbonaceous materials.[92] Detailed descriptions of the DFT approach can be found elsewhere.[93–95] In brief, theoretical isotherms were generated using the NLDFT method, where the fundamental parameters characterizing the gas-gas and gas-solid interactions of the adsorption system were used, for

individual pores of a given adsorbent-adsorbate system. The PSD was then calculated by fitting a combination of the theoretical isotherms to the experimental data. To ensure that potential diffusional limitations of Ar at 87 K did not influence our results, CO_2 adsorption measurements at 273 K were also performed. The PSDs from the combined Ar and CO_2 isotherms were calculated by simultaneously fitting both isotherms with their corresponding 2D-NLDFT models, following the dual-fit method developed by Jagiello et al.[96] Finally, H_2 adsorption isotherms were measured at 77 K and the PSDs from the combined Ar and H_2 isotherms were calculated using the same method.

2.3. Evaluation of electrode performance via flow cell testing

Electrochemical testing was performed in a 2.55 cm^2 zero-gap flow cell architecture in a single electrolyte configuration with an interdigitated flow field at room temperature.[24,25] Tokai G347B resin-impregnated graphite plates of 3.18 mm thickness (Tokai Carbon Co., Tokyo, Japan) milled with an interdigitated pattern served as current collectors and flow fields, while polypropylene flow diffusers (Adaptive Engineering, Waltham, MA) served as backing plates. The electrode compression was controlled with polytetrafluoroethylene (PTFE) gaskets (McMaster Carr) compressed to ca. 80% of the measured thickness. Pristine electrodes have a nominal thickness of 210 μm[97], but we found the actual thickness of both pristine and thermally treated electrodes in the absence of compression varied between 190-225 μm, as measured by a dial thickness gauge (Mitutoyo, 500-195-30, ±15 μm uncertainty). Two layers of carbon paper (1.4 cm × 1.6 cm) prepared with a tape cutter were used for each half-cell, positive and negative. A Daramic 175 separator was used as received. For all tests, the volumetric flow rate was set to ~15 mL min^{-1} (corresponding to superficial linear velocity of ~2 cm s^{-1})[87] using a fixed speed drive peristaltic pump (Masterflex L/S series, 60 rpm) and Norprene tubing (Masterflex L/S 14).

Electrolytes at 50% state of charge (SOC) and 0.1 M were prepared by dissolving 0.05 M of the reduced species (2,2,6,6-tetramethylpiperidin-1-yl)oxyl (TEMPO$^\bullet$) (TEMPO radical, 98%, Sigma Aldrich) and 0.05 M of the oxidized species (2,2,6,6-tetramethylpiperidin-1-yl)oxidanyl (TEMPO$^+$) in 1 M TEABF$_4$ and acetonitrile solution. TEMPO$^\bullet$ was chemically oxidized to TEMPO-BF$_4$ using NOBF$_4$ (98%, Alfa Aesar) as described in previous work.[98] The nonaqueous solution was prepared in an Ar-atmosphere glovebox (both water and oxygen content < 1 ppm, Inertcorp, Amesbury, MA). 10 mL of electrolyte was used for each test and a single electrolyte configuration was employed. All tests were performed using a VMP3 Bio-Logic potentiostat (Bio-

Logic USA, Knoxville, TN), and each test was repeated once. Charge polarization curves were obtained by applying a positive current to the working electrode for 60 s at potentials varying from 0 to 600 mV in increments of 25 mV. Data were recorded every second, and current values from the last 20 s at each set potential were averaged to quantify the degree of polarization and ensure the system was at steady state.

3.   Results and discussion

3.1.   Impact of thermal oxidation of Freudenberg H23 electrodes

Ex situ microscopic, spectroscopic, and electrochemical techniques were used to characterize the physical, chemical, and electrochemical properties of pretreated electrodes. When analyzed together, the effect of pretreatment on the trends and interrelationships of performance-relevant properties—including hydrophilicity, surface functional groups, pore size distribution, and surface area—can be determined

3.1.1.   Analysis of electrode structure and surface properties

SEM images were collected to qualitatively evaluate the impact of thermal pretreatment of electrode microstructure. At moderate (5000×) magnification, there are no noticeable differences between the pristine and thermally treated electrodes. However, at higher (500,000×) magnification, pores of nanometric dimensions can be seen on the fiber surfaces of electrodes treated at 450 °C for 12 h, whereas the fiber surfaces of the pristine electrodes appear smoother (**Figure III-1**).

Pristine   **12 h 450 °C**
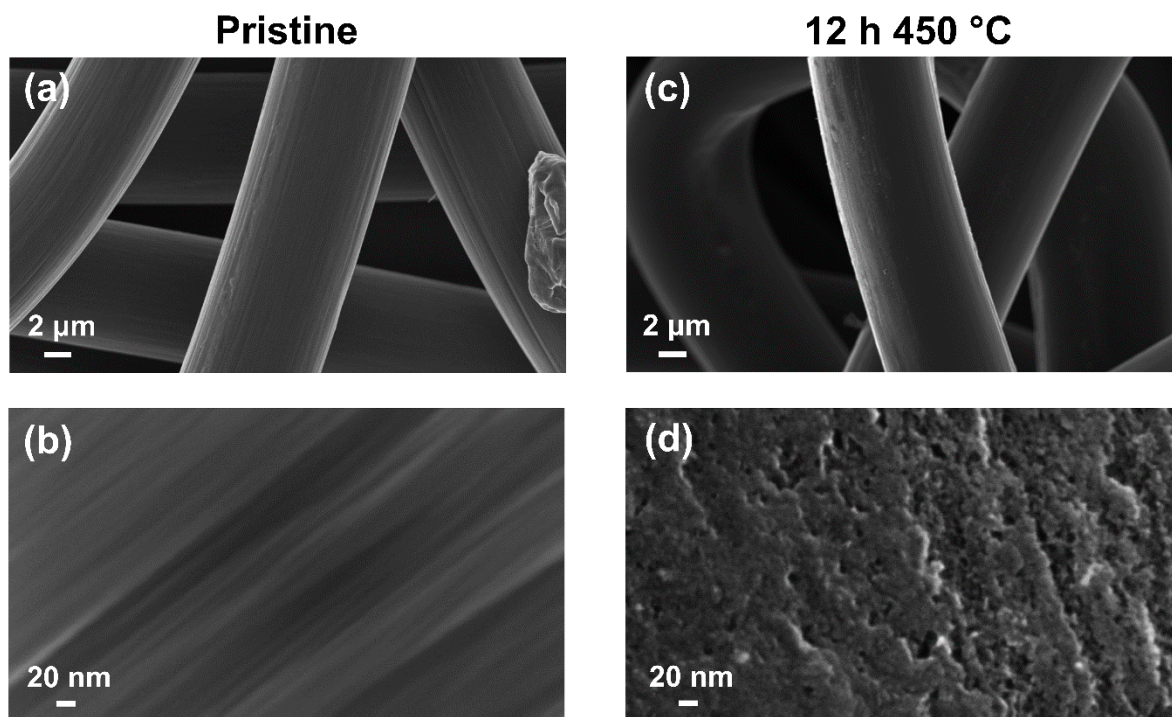
Figure III-1 *Top-down SEM images of Freudenberg H23 electrodes, (a), (b) pristine and (c), (d) treated for 12 h at 450 °C. Micrographs in the first row (a), (c) were captured at 5000× magnification, while micrographs in the second row (b), (d) were captured at 500,000× magnification. While the carbon fibers of the pristine electrode appear smooth, the fibers of the treated electrode have nanoscale pores or indentations on the surface.*

To gain further insight into the effect of thermal pretreatment on electrode fibers, the areal densities of pristine and treated materials were evaluated. Pristine electrodes have an average areal density (electrode mass normalized by geometric area) of 8.2 ± 0.4 mg cm^{-2}, slightly lower than the value of 9.5 mg cm^{-2} reported by the manufacturer.[97] Electrodes treated at 400 °C have similar areal densities as pristine electrodes, in the range of 8.0 to 8.3 mg cm^{-2}, independent of pretreatment time. At higher temperatures, the electrodes maintain constant areal density up to a certain pretreatment time. For electrodes treated at 450 °C, the areal density varies between 7.8 and 8.3 mg cm^{-2} for pretreatment times of 0.5 to 12 h but drops to 6.3 ± 0.5 mg cm^{-2} at 24 h. Similarly, electrodes treated at 500 °C from 0.5 to 4 h have areal densities in the range of 7.9 to 8.3 mg cm^{-2}, while electrodes treated for 5 h have an area density of 7.3 ± 0.7 mg cm^{-2}. Longer pretreatment times at this temperature result in electrodes too fragile to use. This time- and temperature-dependent decrease in density suggests that the electrode surface can be oxidized to a certain extent

before structural degradation occurs. A plot of the areal density as a function of time and temperature is shown in **Figure III-2**.
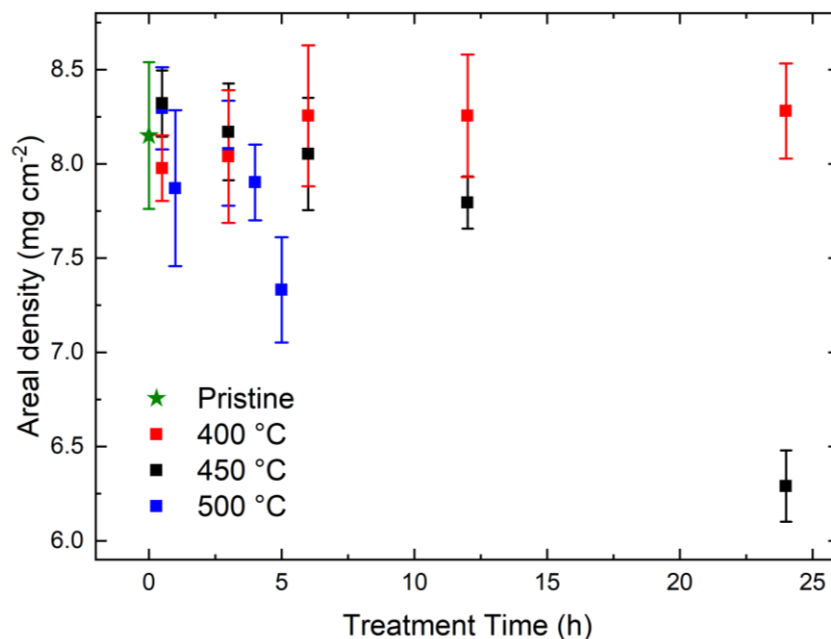
Figure III-2 *Areal density as a function of treatment time for each pretreatment temperature.*

XPS analysis was used to estimate oxygen functional groups present on the carbon fiber surfaces within the pristine and treated electrodes. The results show that more oxygen functional groups are added at higher temperatures and that for each temperature, surface coverage of oxygen functional groups increases with pretreatment time (**Figure III-3**). However, the relative increase in oxygen functional groups diminishes at longer times, seemingly approaching a plateau that is not necessarily reached due to the onset of sample degradation. There are no observed trends in specific oxygen-containing groups (i.e., carbonyl, carboxyl, hydroxyl) as a function of pretreatment temperature or time.

Electrode wettability may affect measured ECSA: poor wettability will mean that some useable surface area is not in contact with the electrolyte. To assess the wettability of thermally treated samples external contact angle measurements were performed in triplicate with droplets of deionized (DI) water and acetonitrile. As expected based on prior investigations of porous carbon materials,[99,100] the pristine materials are hydrophobic with an apparent external contact angle of $117 \pm 4°$ for DI water. In contrast, all thermally treated electrodes immediately imbibe the water droplet upon contact, even at the shortest pretreatment time of 0.5 h, indicating that the addition

of oxygen functional groups on the fiber surfaces induces wetting.[101] All pristine and treated electrodes immediately imbibe the acetonitrile droplets evincing good wettability of the nonaqueous solvent.[89]
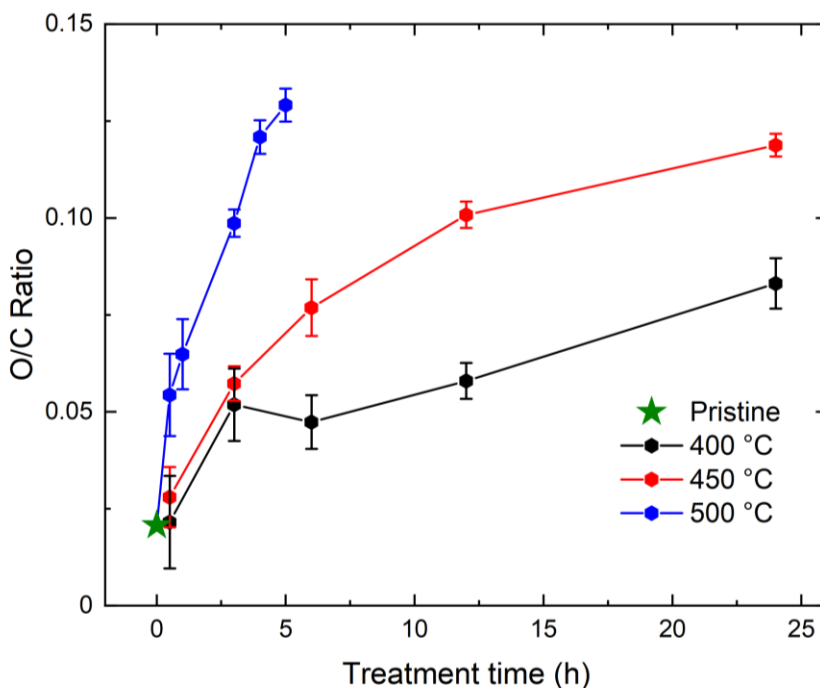
Figure III-3 *Relative amount of surface oxygen functional groups compared to surface carbon functional groups as measured by XPS. The O/C ratio increases with pretreatment time but amount of oxygen added appears to reduce as pretreatment time increases. For each data point, three different locations on two independent samples were analyzed (*n = 6*).*

3.1.2. Analysis of electrode surface area and pore size distribution

To quantify the electrode surface area, we utilized a combination of analytical and electrochemical techniques. To study materials with a broad surface area range and capture variability in SSA as a function of pretreatment time, electrodes treated at 450 °C were selected for study with either Kr or Ar gas adsorption. Kr adsorption is well-suited for samples with low specific surface area (< 1 m^2 g^{-1}) or low absolute area (i.e., small amount of sample), as the saturation vapor pressure of Kr (2.4 mm Hg at 77 K) is several orders of magnitude lower than the saturation pressure of Ar (760 mm Hg at 87 K). In the volumetric method used here, lower saturation pressure leads to larger pressure changes for similar relative pressure steps, which are easier to detect. This enables more accurate measurements of low surface area samples for which

small amounts of gas are adsorbed.[102] However, for samples with larger surface area, it is preferable to use other adsorbates (e.g., N$_2$, Ar) due to a lack of information about the Kr cross-sectional area in confined environments.[34] In contrast to N$_2$, which presents a significant quadrupole moment, Ar is considered more reliable due to its minimal specific interactions with surface polar group.[104] For this reason, we used Ar in the SSA measurement for larger surface area samples (> 6 h pretreatment time). The difference in estimated SSA between Kr- and Ar-based BET measurements is relatively small (~12%) and both show identical trends. Specifically, an increase in SSA from 0 to 12 h followed by a decrease from 12 to 24 h. Pristine electrodes and all electrodes pretreated at 450 °C were evaluated with Kr-based BET, and samples treated for 6, 12, and 24 h at 450 °C (SSA > 10 m^2 g^{-1}) were also evaluated with Ar-based BET. For comparison with ECSA and discussion of results, we used the BET values measured with Kr for pristine, 0.5, and 3 h and Ar for 6, 12, and 24 h to ensure the greatest accuracy. We find that as pretreatment time increases, electrode SSA initially increases, reaching a maximum of 44 ± 1 m^2 g^{-1} at 12 h (compared to 0.7 ± 0 m^2 g^{-1} for pristine). Further extending pretreatment time to 24 h results in a SSA of 40 ± 3 m^2 g^{-1}. This, along with the electrode areal density measurements, which are constant for 0 to 12 h of pretreatment but decrease at 24 h (**Figure III-2**), indicates that as the electrode surface is oxidized, there is a maximum surface area that may be achieved, beyond which structural decomposition results in a loss of surface area.

To evaluate the ECSA of the electrodes and understand its relationship to the physical surface area, we compared the ECSA with SSA from gas adsorption. We measured electrochemical capacitance in two different electrolyte compositions: aqueous 1 M H$_2$SO$_4$ (**Figure III-4(a)**) and nonaqueous 1 M TEABF$_4$ in acetonitrile (**Figure III-4(b)**). Both systems show similar trends: ECSA for electrodes treated at 400 °C monotonically increases as a function of pretreatment time, whereas electrodes treated at 450 and 500 °C increase to maxima at moderate times (12 and 4 h, respectively) before decreasing at longer times. The gas adsorption results show that SSA follows a trend identical to that of ECSA, with an initial increase in SSA followed by a decrease after 12 h of pretreatment for electrodes treated at 450° C (**Figure III-4(c)**).

Although the trends for all three approaches are consistent, there are differences in the magnitude of the measured surface area. Specifically, the ECSA measured in the nonaqueous TEABF$_4$ system is markedly lower than that measured in aqueous H$_2$SO$_4$. We hypothesize that this difference is due to the size of the constituent components within the electrochemical double

layer: as molecular size increases, measured capacitance (and thus ECSA) decreases, as fewer molecules can pack into the outer Helmholtz plane and/or access the smaller surface features.[105] The solvated diameter of the dissolved charged species can be estimated by summing the diameter of the molecule or atom and the diameter of the average number of solvent molecules that are affected by the electric field induced by the charged species.[106] In the aqueous electrolyte, solvated H^+ has an effective diameter of 0.80 nm ($H^+ \cdot 2.6H_2O$) estimated from standard partial molar volumes of hydrochloric acid,[106] while the effective diameter of solvated SO_4^{2-} is estimated to be 0.46 nm ($SO_4^{2-} \cdot 0.72H_2O$) via molecular dynamics simulations.[107] In the nonaqueous electrolyte, solvated TEA^+ has an effective diameter of 1.3 nm ($TEA^+ \cdot 7ACN$) and the BF_4^- effective diameter is 1.1 nm ($BF_4^- \cdot 9ACN$), both estimated from molecular dynamics simulations,[108] and larger than the aqueous ions. As shown in **Figure III-4(c)**, for electrodes treated at longer times (> 3 h), ECSA measured with either electrolyte is less than the physical surface area measured with gas adsorption, indicating an appreciable fraction of the surface area is inaccessible. However, there is good agreement between physical surface area and ECSA at shorter treatment times (< 3 h), suggesting that ECSA measurements provide a reasonable representation of the total surface area provided it is fully accessible to the electrolyte.
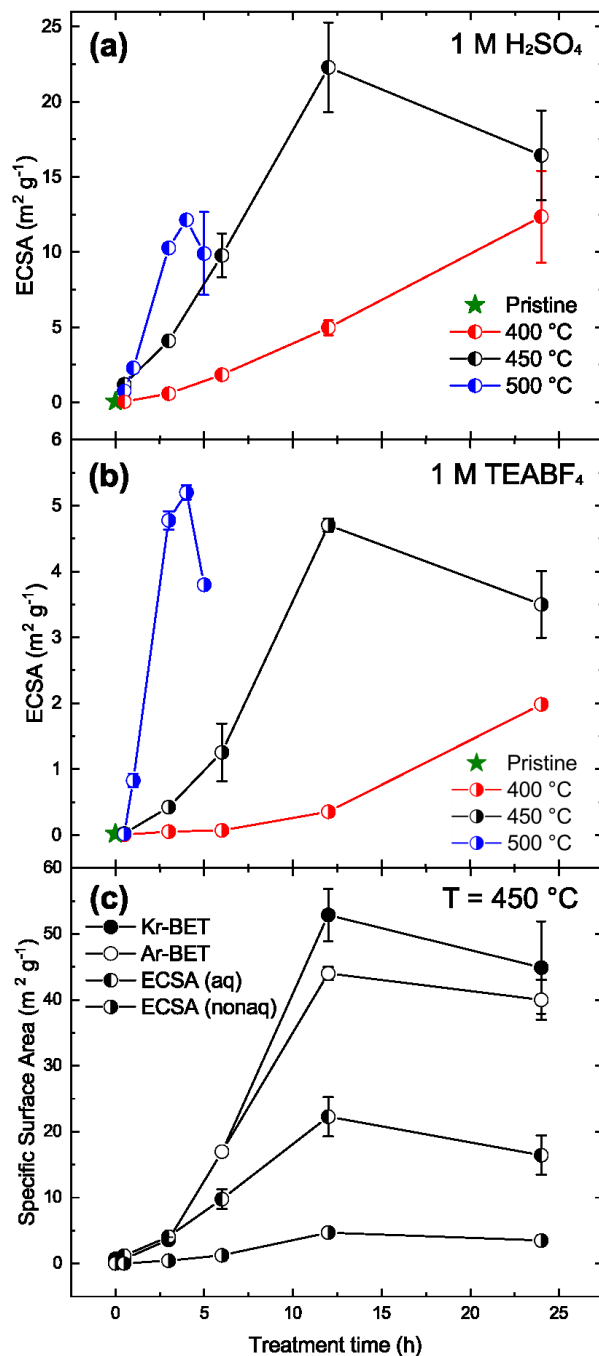
Figure III-4 *Specific surface area of thermally treated electrodes as a function of pretreatment time. (a) ECSA measured with electrode capacitance in 1 M H₂SO₄ solution. (b) ECSA measured with electrode capacitance in 1 M TEABF₄ solution. ECSA increases as function of pretreatment temperature but reaches a maximum at 450 and 500 °C in aqueous and nonaqueous systems. (c) Comparison of ECSA in both systems with specific surface area measured with Kr-BET and Ar-BET. In all cases, each measurement was repeated once (*n *= 2). Surface area as a function of pretreatment time display similar trends, but ECSA underpredicts the physical surface area of the electrode.*

To further characterize the porosity generated by thermal oxidation, we calculated the PSDs from the analysis of adsorption isotherms of Ar using 2D-NLDFT model for carbon slit-shaped pores. At 77 K, diffusion of N_2 into carbon ultramicropores (< 7 Å) is very slow,[109] which may cause under-equilibration of measured adsorption isotherms and distort the resulting PSD. In order to avoid potential diffusion limitations, we performed adsorption measurements with fast-diffusing CO_2 and H_2 adsorbates and coupled these isotherms with the Ar-adsorption isotherm.[110] It has been shown that CO_2 molecules can access ultramicropores in a reasonable time at 273 K due to relatively high temperature and pressures.[111,112] We elected to use H_2 for two reasons: (i) H_2 diffuses well in ultramicropores as it is supercritical at 77 K, and its relatively small kinetic diameter (2.9 Å) allows smaller pores to be probed in comparison to other adsorbates (kinetic diameters of Ar and CO_2 are 3.4 and 3.3 Å, respectively), and (ii) as compared to CO_2, which has a strong quadrupole moment that influences its adsorption on polar surface groups, H_2 has a minimal quadrupole moment, therefore enabling more accurate characterization of samples where polar groups are present on the surface.[110,113] The resulting unified PSDs are more robust, as they are consistent with both adsorption isotherms. Taken together, the comparison between the unified PSDs using Ar/CO_2 and Ar/H_2 gives information on the presence of polar surface oxygen functional groups on the surface of the thermally treated samples.

The calculated PSDs are shown in **Figure III-5(a)**. For the pristine Freudenberg H23 electrode, we do not observe any porosity in the microporous range (< 2 nm). However, for electrodes treated at 450 °C for 12 and 24 h, we observe peaks in the PSD at 0.42 nm and 1.5 nm, indicating that some microporosity has either been generated or exposed by pretreatment. Note that the PSD does not present sharp peaks but rather is continuous over the micropore size range, which is typical of disordered porous networks and likely entails the presence of bottlenecks that will hinder diffusion of the electrochemical species and impact accessibility.[114] We find the PSD peak locations are consistent for Ar, Ar/CO_2, and Ar/H_2 mixtures, but the intensity of the peak at 0.42 nm is lower for Ar. This indicates some diffusional limitations for Ar in the sub-nanometer pores at 87 K and highlights the importance of using faster-diffusing gases for the accurate determination of PSDs. The PSDs derived from Ar/CO_2 and Ar/H_2 methods are very similar, indicating that the polar oxygen surface functional groups added via thermal treatment have no effect on the adsorption of CO_2, which may indicate that, in contrast to the external surface area, the internal surfaces of the micropores are not fully oxidized during treatment. This result is complementary to XPS and

contact angle measurements, which provide information on the external surface properties of the sample, while adsorption allows for the bulk characterization of the internal surface. Moreover, this phenomenon has been documented in a previous study of double layer capacitance in activated carbon surfaces, where the surface of internal pores formed during activation was found to be composed primarily of basal plane carbon, with few surface oxygen functional groups present.[90] However, we note that the sensitivity of the PSD for samples with low concentration of functional groups is unclear at present; thus, further investigations are needed to verify this assumption.

By plotting the differential surface area as a function of pore size using the 2D-NLDFT method (**Figure III-5(b)**), we find that the majority of added surface area is in the microporous range (≤ 2 nm diameter). We also performed MIP on the electrodes, to confirm that additional surface area is not generated in the meso- or macroporous range, and show that the differential uptake is negligible above a 10 nm pore diameter (**Section S3**). However, it remains unclear how much of the added surface area is accessible to electrochemical species, as much exists in recessed pores smaller than their estimated solvated diameter. By plotting the differential surface area as a function of pore size and comparing the SSA to the ECSA, we can estimate the pore size at which fully-solvated electrochemical species are blocked from entering the internal surface area generated via thermal treatment. We propose to use this accessible pore size as a general indicator correlating the textural properties of the sample (e.g., pore size, pore surface chemistry, and topology of the porous network) with the properties controlling the accessibility of the electrochemical species for given conditions (e.g., wettability, voltage window, concentration, and partial or complete ion desolvation). By comparing the ECSA results with differential SSA as a function of pore size, we find that the smallest accessible pores in each sample increase slightly with increasing pretreatment time: in 1 M H_2SO_4, pores below 0.65 nm in size are not accessed in the 6 h sample, pores below 0.72 nm in size are not accessed in the 12 h sample, and pores below 0.85 nm in size are not accessed in the 24 h sample. These values show good agreement with the estimated solvation diameter of H^+ (0.80 nm).[106] Collectively, these results suggest that pores smaller than the solvation diameter of electrochemical species are not accessible, and this exclusion is the most likely cause of the discrepancy in physical surface area and ECSA at longer pretreatment times. Further, the slight increase in the lower bound of the accessible pore diameter seems to indicate that the textural properties evolve with the pretreatment time, gradually decreasing the access of the electrochemical species to the porous network. Similarly, in 1 M $TEABF_4$, we find that pores

below 1.83 nm (6 h), 1.85 nm (12 h), and 1.9 nm (24 h) are not accessed, which again shows an increasing trend with pretreatment time, and is similar to the literature estimate of solvated TEA^+ diameter (1.3 nm). We note that comparing the solvated ion diameters and pore sizes implicitly assumes that ion desolvation is thermodynamically unfavorable and that wetting of pores the same size or larger than the solvated ions is thermodynamically favorable.[115]

We caution against the treatment of these PSDs as exact limiting values. There is uncertainty in both measurement techniques: Ar gas adsorption to estimate SSA (± 1 m^2 g^{-1} for 12 h and ± 3 m^2 g^{-1} for 24 h) and capacitance measurements to estimate ECSA (± 1.5 m^2 g^{-1} for 6 h and ± 3 m^2 g^{-1} for both 12 and 24 h). Additionally, as previously state, the specific capacitance of the carbon fiber surface is assumed to be similar to that of glassy carbon, which is another potential source of error. We also note that the actual solvation diameter is likely to be somewhat different than the literature estimates due to the higher ion concentrations, the effects of electric field at the electrode-electrolyte interface, and the impact of confinement on the solvation structure itself.[116] In particular, the deviation from dilute solution behavior, as might be expected in practical technology embodiments, will result in a divergence from unity for both the osmotic coefficient of the solvent and the activity coefficient of the electrolyte.[117] Further, the small differences between limiting pore diameters for 6, 12, and 24 h, may be explained by variances in pore geometry of the samples. Specifically, because of the extremely small pore sizes, bottlenecks may form in the electrochemical environment that are not present in the gas adsorption environment, and, as such, contribute to variation in the ECSA measurements of electrodes at different pretreatment temperatures which have distinct pore geometries. In sum, these results are a general indicator for accessible pore diameter at given conditions and evince the importance of coupling ECSA and physical surface area measurements to evaluate the total surface area as well as the surface area accessible to electrochemical species in solution.
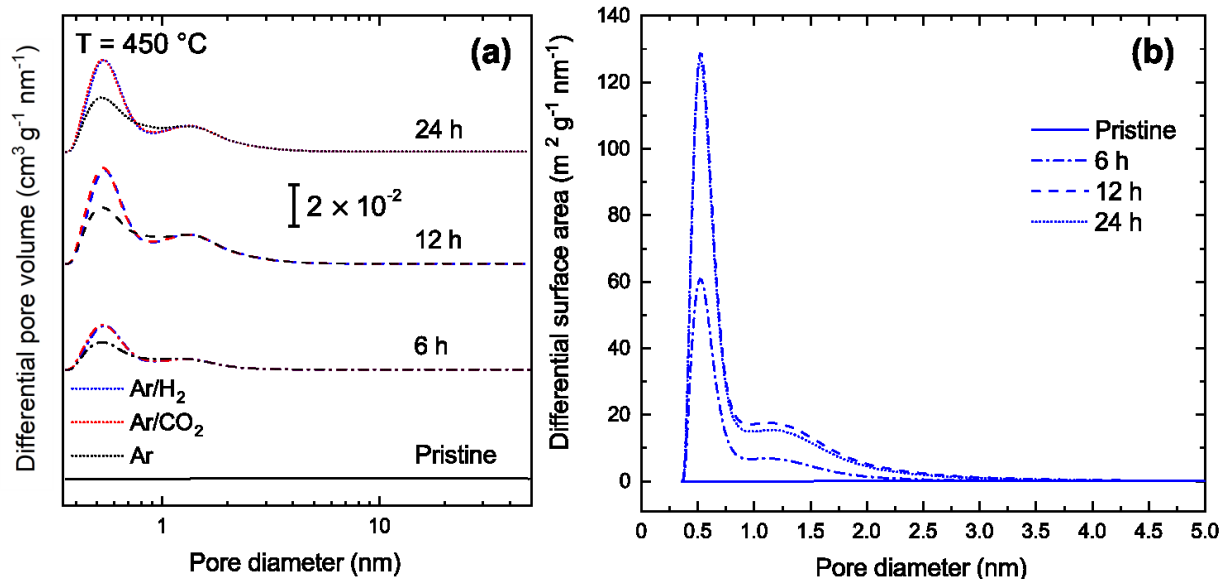
Figure III-5 *(a) Pore size distribution of thermally treated samples at 450 °C from Ar (black), Ar/CO₂ (red), and Ar/H₂ (blue). (b) Differential surface area as function of pore diameter measured with Ar/H₂. (a) and (b) show that majority of generated surface area for thermally treated samples is in the micropore range (< 2 nm).*

3.2.   Analysis of electrode performance in flow cells

To explore the impact of electrode surface area on flow cell performance, we designed a system to separate the effect of added surface area from the convoluting effects of wetting or surface oxygen functional groups. Specifically, we selected TEMPO˙/TEMPO⁺ in 1 M TEABF₄ / acetonitrile as redox electrolyte, as, due to its fast kinetics,[118] we do not anticipate sensitivity to surface groups; further, as a nonaqueous system, it is not sensitive to wetting. Because higher surface area should, in general, provide more reaction sites per given electrode volume, the system is expected to be sensitive to surface area.

Figure III-6 shows the measured iR_Ω-corrected polarization curve in the kinetically limited region (low current density, estimated as 0-60 mA cm⁻² based on curvature of the polarization curve) in a single electrolyte flow cell as a function of electrode pretreatment time at different current densities. While the overpotential of the cell decreases with thermal pretreatment as compared to the pristine polarization curve, all thermally treated electrodes have comparatively similar polarization behavior (**Figure III-6(a)**). Constant overpotential in the kinetically limited region across electrodes with different surface areas suggests that the pretreated electrodes either contain sufficient surface area such that the number of reaction sites is not a limitation, or that the

surface area added is inaccessible (*vide supra,* **Section III.3.1.2***Ex-situ* materials characterization*II.3.1*). The plots of cell overpotential vs. nonaqueous ECSA, shown in **Figure III-6(b)**, further support the hypothesis that surface area does not play a significant role in performance, as we do not observe a clear correlation between overpotential and ECSA. Specifically, we see an initial decrease in overpotential with relatively small increases in surface area (from 0.1 to 1 m^2 g^{-1}), beyond which overpotential levels off despite further increase in surface area. This trend is confirmed with the results of the convection-reaction model in **Chapter IV** (*vide infra*). Further, while overpotential decreases with increased electrode surface area, the observed changes are smaller than expected based on the order of magnitude change in ECSA (2-3 orders of magnitude increase in ECSA from pristine to electrodes treated at 450 °C for 12 h). For this experimental data it is unclear whether the surface area is inaccessible, or whether the surface area is accessible but mass transport limitations hinder its use. This question is considered through convection-reaction modeling in the following chapter.
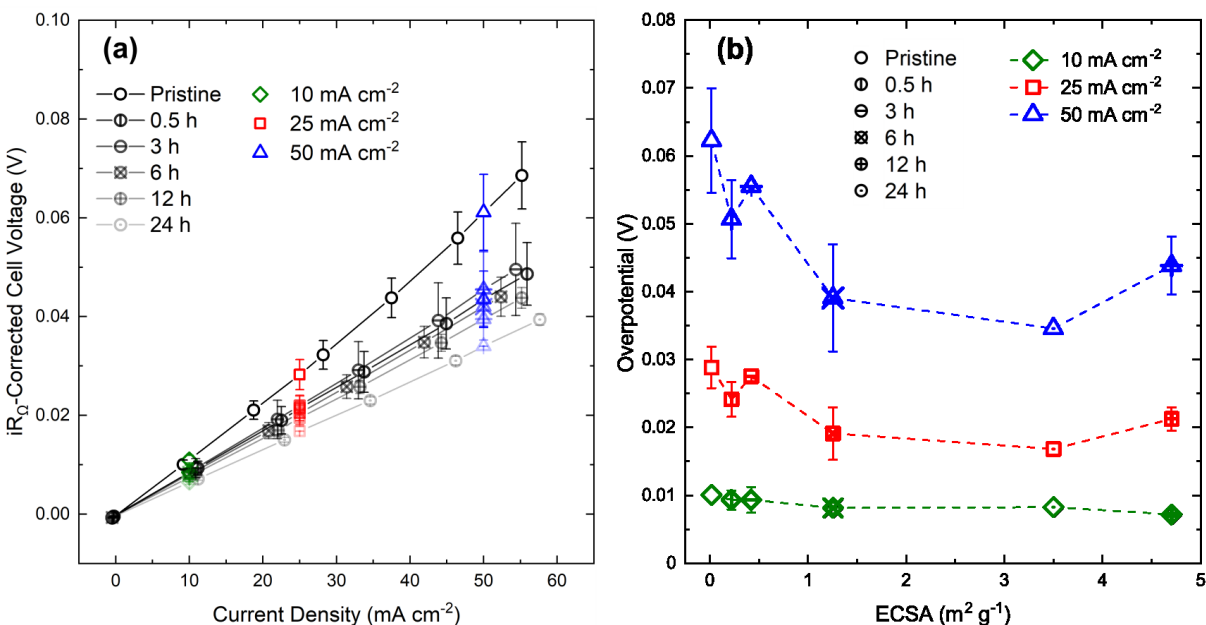
Figure III-6 *iR_Ω-corrected polarization in kinetically-limited region (0-60 mA cm^{-2}) of single-electrolyte TEMPO˙/TEMPO⁺ flow cell at 50% SOC as a function of electrode treatment time at 450 °C. (a) Cell overpotential of treated electrodes overlay, while pristine electrodes have slightly higher overpotential. (b) Cell overpotential of the TEMPO˙/TEMPO⁺ electrolyte (up to 50 mA cm^{-2} current density) changes only slightly as a function of ECSA (*n=2).*

4. Conclusions

Thermal oxidation is a common pretreatment for commercial carbon fiber materials used in RFBs, as it enhances electrode performance by improving electrochemical activity via surface functionalization and increasing electroactive surface area via enhanced wettability and increased physical surface area. However, the effects these properties have on flow cell performance are difficult to decouple, and it is often unclear to what extent each property is responsible for performance improvements. In this work, we studied the impact of electrode surface area on RFB performance. We characterized the physical electrode surface area using gas adsorption and compare the SSA to ECSA, demonstrating that thermal pretreatment increases both SSA and ECSA; however, as pretreatment time increases, the ECSA becomes an increasingly smaller fraction of the SSA. We find that a significant fraction of porosity added via thermal pretreatment is in the micropore (≤ 2 nm) range, and postulate that the solvation diameter of electrochemical species in solution inhibits access to these small pores and thus a sizeable fraction of the SSA. By testing the performance of thermally treated electrodes with a model redox couple in a single electrolyte flow cell configuration, we find that increases in surface area positively impact kinetic performance of the electrodes, but this effect is much smaller than would be expected for the observed increase in ECSA. Taken together, these results demonstrate that future electrode design should carefully consider the nature of added surface area to ensure that it is accessible to electrochemical species in solution; further mass transfer losses within electrodes are as important to consider as kinetic losses, especially with the facile redox reactions used in emerging RFB systems. Finally, these results suggest moderate improvements to electrode surface area (exact magnitude specific to system characteristics such as electrode and active species) are sufficient to overcome surface area limitations in electrode performance, and that catalysis (i.e. increasing heterogeneous rate constant) and mass transport should be the focus of electrode engineering and design.

5. Acknowledgments

IV.   Convection-Reaction Model for Redox Flow Battery Electrodes

In the previous chapter, we showed that increases in electrode surface area can positively impact electrode performance via decreasing overpotential. However, this effect is much smaller than would be expected for the observed increase in ECSA—while we achieved a two order of magnitude increase in ECSA via electrode modification, overpotential decreased only tens of millivolts. Moreover, once a moderate increase in surface area was achieved over the base case, overpotential ceased to decrease with further increases in ECSA. Here, we seek to expound this behavior by modeling electrode overpotential as a function of ECSA. Specifically, we develop a convection-reaction model of the one-dimensional concentration profile within an electrode. We use this concentration profile to estimate corresponding electrode overpotential as a function of surface area. With this model, we validate the observed experimental trends: overpotential initially decreases exponentially as ECSA increases; however, there is a maximum useable surface area beyond which decreases in overpotential are greatly diminished. The value of this maximum useable surface area changes as standard rate constant and interstitial velocity are varied; specifically, as standard rate constant (i.e., reaction rate) increases, maximum useable surface area decreases, as fewer reactions sites are necessary to deplete the bulk concentration. As interstitial velocity (i.e., rate of reactant mass transport) increases, maximum useful surface area increases, as the bulk concentration is replenished throughout the electrode area and more surface area may be utilized. Overall, these results show that the extent to which surface area improves electrode performance is highly dependent on other system properties, and that kinetic improvements via catalysis and enhanced mass transport should be the main focus of electrode engineering efforts.

1.   *Background*

To study the nature of surface area generated via thermal pretreatment and to assess its importance in electrochemical reactions, in **Chapter III** we compared the physical electrode area (SSA) with electrochemically accessible surface area (ECSA) and probed the trend between ECSA and electrode performance. Our analyses indicate that both ECSA and SSA of the electrodes are maximized at moderate pretreatment temperatures and times, and that further treatment results in reduced surface area of the electrode. Electrodes with increased surface area show improved performance over the baseline, but as surface area increases further there are diminishing returns in performance gains. Here we seek to rationalize this observation with a one-dimensional

convection-reaction model, which is used to analyze the trade-offs between mass transport and effective use of catalyst sites in a porous architecture.

In order to calculate electrode overpotential, we utilized a classical approach in chemical engineering by deriving an effectiveness factor to compare the observed reaction rate to the theoretical reaction rate that would be achieved if the entire electrode area was exposed to the bulk electrolyte concentration. The characteristic transport lengthscale used is the volume of the slab divided by its surface area, which was shown as a valid approximation for predicting the effectiveness factor of various shapes in the seminal work of Aris.[119] We assume that electrolyte transport is dominated by convection—as typical superficial velocities do not exceed 100 cm s^{-1}, and assuming superficial and interstitial velocities are equivalent, Péclet number (Pe) varies from 10^2-10^8, indicating mass transport from diffusion should be negligible.[87] We assume a diffusivity of 10^{-9} m^2 s^{-1}, which is standard for the electrochemical species in which we are interested: previous work experimentally found the diffusivity of TEMPO$^\bullet$ and TEMPO$^+$ to be 1.46±0.14 × 10^{-9} and 1.33 ±0.08 × 10^{-9} m^2 s^{-1}, respectively.[86] Additionally, we assume that boundary layer affects are negligible; in order to justify this assumption, we limit the heterogeneous standard rate constants studied to ≤10^{-6} m s^{-1} such that the Damköhler number (Da), or ratio of kinetic rate to diffusion rate, is much less than 1. With convection dominated transport and in the absence of boundary layer effects, the effectiveness factor is dependent on the ratio of Da number to Pe—a dimensionless parameter that describes the balance between kinetic and mass transport resistances in the electrode slab. In regimes where this dimensionless value is large, overall reaction rate is limited by mass transport limitations and bulk concentration is depleted quickly upon entering the electrode slab, whereas at small values, the overall reaction rate is limited by the reaction rate which is controlled by the rate constant and available surface area.

Here, we used the effectiveness factor to study electrode utilization as a function of electrode overpotential. We assessed effectiveness factors as a function of applied potential using Butler–Volmer kinetics, and assumed one-dimensional transport through a slab that represents the electrode. We used this model to study electrode overpotential as a function of surface area, and varied mass transport efficiency and kinetic rate constant to determine the interdependency of these relationships. With these results, we outlined design principles for electrocatalyst sizing based on desired utilization. While conditions and parameters used in this work are based on an aqueous electrolyte at room temperature in a porous carbon paper electrode, we anticipate that the

mathematical framework is generalizable and applicable to porous electrocatalysts across a range of conditions.

2. *Model formulation*

A model was formulated to quantify the effect of surface area on performance. We modeled the electrode as a slab with an internal surface area (ECSA) that is geometry agnostic—in other words, the ECSA of the electrode is not represented by fibers, pore walls, etc., but is rather the amount of intrinsic surface area within the slab, all of which is assumed accessible to active species. We assume one-dimensional transport in the x-direction within the slab is not affected by the electric field (i.e., excess supporting electrolyte) and is dominated by convection rather than diffusion. This assumption is derived from the scaling of the electrode-scale Péclet number (Pe) the convective mass transport rate compared to the diffusive mass transport rate (**Equation IV-1**).

$$Pe = \frac{uL}{D} \tag{IV-1}$$

Here u is superficial velocity within the electrode (m s^{-1}), L is the length of the flow path (m), and D is the diffusivity of the reactant (m^2 s^{-1}). In the range of conditions that are typical for the RFB system under investigation (**Table IV-1**), Pe is large (Pe >> 1). Additionally, this treatment assumes the boundary layer effect along the reaction surface is negligible, which is derived from the electrode-scale Damköhler number (Da) scaling, the ratio of reaction rate to diffusion rate (**Equation IV-2**).

$$Da = \frac{l^2}{D}k \tag{IV-2}$$

Here, l is the representative microscopic length scale (m) and k is the homogeneous first-order rate constant (s^{-1}). Da is small in the range of conditions investigated (Da << 1). The physical quantities used in the scaling analysis and the justification of their use and/or derivation are shown in **Table IV-1**.

Table IV-1 – *Order of magnitude approximations of the physical quantities used in the scaling analysis of transport within the electrode system, as well as resulting scaling of Pe and Da. A justification is provided for each property.*

Property	Order of magnitude	Justification
Superficial velocity u (m s^{-1})	$10^{-4} – 10^1$	Range of velocities typically used in flow cell experiments; calculated from pump volumetric flow rate and the dimensions of the flow field and electrode.[87]
Length of flow path L (m)	10^{-4}	The flow path is assumed to be the slab volume divided by surface area. Electrode dimensions are 0.017 m × 0.015 m × 0.00021 m.
Diffusivity of reactant D (m^2 s^{-1})	10^{-9}	Experimentally measured diffusivity for the electrochemical species in this work.[86]
Microscopic length scale l (m)	10^{-6}	Square root of electrode permeability, derived experimentally from the Darcy-Forchheimer equation.[86]
Effective homogeneous rate constant k (s^{-1})	$10^{-5} – 10^2$	Calculated with electrode surface area and heterogeneous standard rate constant k^0, which was varied from 10^{-10} to 10^{-6} m s^{-1}. Typical standard rate constants of redox molecules used in RFB systems vary from 10^{-10} m s^{-1} for slow systems (i.e. vanadium)[99] to 10^{-3} m s^{-1} for fast systems (i.e. TEMPO.)[120] However, for standard rate constants above 10^{-6} m s^{-1} the scaling of Da does not meet the required criteria of Da $<< 1$, thus we limit our study to rate constants of 10^{-6} m s^{-1} or less. The standard rate constant was normalized by the volumetric surface area internal to the slab (calculated with ECSA (varied from 0.1 – 100 m^2 g^{-1}) multiplied by the density of the electrode material ($\rho = 2 \times 10^6$ g m^{-3}, measured experimentally) (**Equation IV-4**).
Péclet number Pe	$10 – 10^6$	See **Equation IV-1**
Damköhler number Da	$10^{-7} – 10^{-1}$	See **Equation IV-2**

After applying the scaling analysis to the system, the resulting governing equation and boundary condition are shown in **Equation IV-3**. Note that this representation is qualitatively analogous to a flow-through flow field configuration in a flow cell.[87]

$$\frac{dC}{dx} = -\frac{k}{u}C; \quad C(x = 0) = C_{bulk} \tag{IV-3}$$

Where C is active species concentration (mol m^{-3}), C_{bulk} is the bulk concentration (0.05 mol m^{-3}), x is position within the electrode slab (m), u is interstitial velocity within the slab (varied from $10^{-4} - 10^1$ m s^{-1}), k is the effective homogeneous rate constant (s^{-1}), calculated with the heterogeneous standard rate constant k^0 (varied from 10^{-10} to 10^{-6} m s^{-1}) normalized by the volumetric surface area internal to the slab (calculated with ECSA (varied from $0.1 - 100$ m^2 g^{-1}) multiplied by the density of the electrode material ($\rho = 2 \times 10^6$ g m^{-3}, measured experimentally) (**Equation IV-4**)).

$$k = k^0 \rho \cdot ECSA \tag{IV-4}$$

From the governing equation (**Equation IV-3**), we solved for the dimensionless concentration profile Ψ normalized by C_{bulk} within the slab (**Equation IV-5**):

$$\Psi(v) = e^{-\frac{kL}{u}v} \tag{IV-5}$$

where L is the characteristic length of the flow path (slab volume divided by surface area, $\sim 10^{-4}$ m) and v is the dimensionless position normalized by L. Using the dimensionless concentration profile, we calculated an effectiveness factor H, defined as the rate of reaction within the slab normalized by the rate of reaction if the entire internal surface area was exposed to the bulk concentration. This rate is calculated by integrating **Equation IV-5**, the dimensionless concentration profile, across the normalized length of the electrode to find the average concentration, and normalizing this concentration by the bulk concentration. The resulting effectiveness factor H is shown in **Equation IV-6**.[119]

$$H = \frac{u}{kL}\left(1 - e^{-\frac{kL}{u}}\right) \tag{IV-6}$$

To determine the resulting current as a function of overpotential, we first calculated a reference current density using Butler-Volmer kinetics, assuming that the concentration within the electrode surface is uniform and equal to the bulk concentration. We adjusted this reference current density

to the expected current density with the calculated effectiveness factor. To account for the availability of reaction sites through the electrode slab, we scaled the current density by the ECSA normalized by the geometric area (**Equation IV-7**).

$$i = i_{ref} H \frac{mECSA}{A_{geo}} = H \frac{mECSA}{A_{geo}} i_0 \left(exp \left[\frac{\alpha_f nF}{RT} \eta \right] - exp \left[\frac{-\alpha_r nF}{RT} \eta \right] \right) \tag{IV-7}$$

Here, i_0 is the exchange current density ((A m^{-2}) calculated with the standard rate constant k^0 and C_{bulk}), m is the electrode mass (g), A_{geo} is the geometric area of the electrode (2.55 m^2) α_f and α_r are the forward and reverse charge transfer coefficients, respectively (both assumed to be 0.5), n is the number of electrons transferred per molecule (1 mol e$^-$ mol^{-1}), F is the Faraday constant (C mol^{-1}), R is the universal gas constant (J mol^{-1} K^{-1}), T is absolute temperature (assumed to be 298 K), and η is overpotential (varied from 0.1 to 0.8 V).

3.   Results and discussion

3.1.   Concentration profile and effect of dimensionless coefficient

To determine the character of the concentration profile through the slab, we plot dimensionless concentration as a function of position within the slab at fixed standard kinetic rate constant (10^{-8} m s^{-1}) and interstitial velocity (10^{-2} m s^{-1}) (**Figure IV-1(a)**). We find that the active species concentration exponentially decays along the flow path, and that there is greater consumption of active species at larger ECSA. To understand the impact of kinetic and transport limitations on electrode performance, we plot the calculated effectiveness factor, which is the rate of reaction normalized by the rate of reaction if the entirety of the internal surface of the electrode were exposed to the bulk concentration, as a function of the dimensionless parameter kL/u, which is the ratio of the reaction rate to the rate of convective transport (**Figure IV-1(b)**). We find that increasing standard rate constant decreases the effectiveness factor, as faster active species consumption results in diminished concentration through the slab. Similarly, we find that increasing interstitial velocity increases the effectiveness factor, as the active species is more quickly replenished and thus concentration gradients through the electrode are minimized. In an ideal system, as rate constant is increased (either through increases in ECSA or standard rate constant), the rate of active species transport would be augmented to balance the increased rate of consumption.
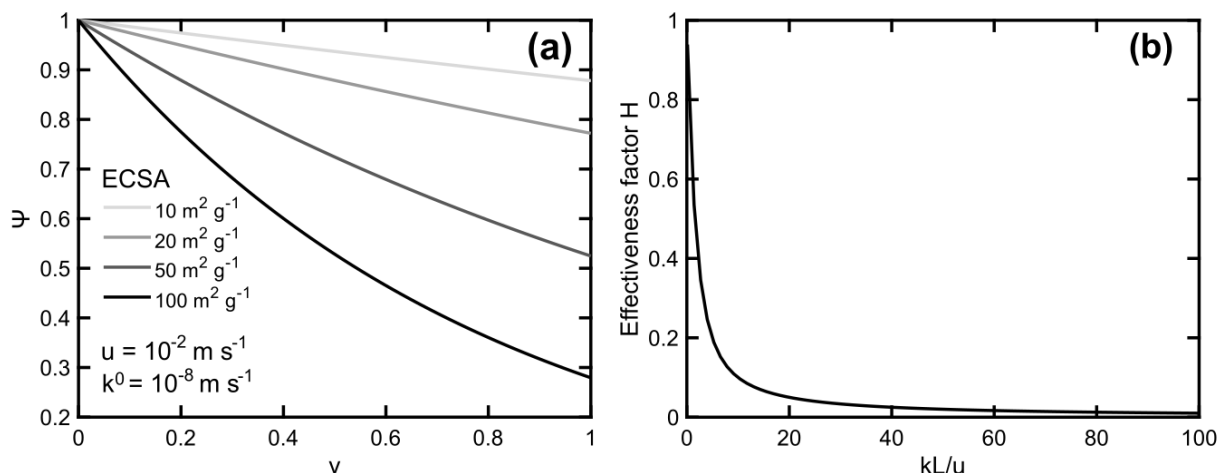
Figure IV-1 *(a) Dimensionless concentration profile over the length of the electrode. Standard rate constant was set to 10^{-8} m s^{-1}, interstitial velocity was set to 10^{-2} m s^{-1}, and ECSA was varied from 10 to 100 m^2 g^{-1}. (b) Effectiveness factor as a function of dimensionless parameter kL/u. Effectiveness factor diminishes quickly as this parameter increases, reflecting the concentration gradients that form due to fast kinetics and/or diminished interstitial velocity.*

3.2.   Effect of surface area on electrode performance

Using the presented mathematical framework, we studied how electrode overpotential changes as a function of surface area. This treatment assumes all the surface area is accessible to electrochemical species in solution and that this internal surface area is geometry agnostic (no specific microstructure). We also vary kinetic performance (via standard rate constant) and mass transport (via interstitial velocity) to explore the impact of surface area in different regimes (**Figure IV-2**). **Figure IV-2(a)** illustrates overpotential as a function of ECSA: initially, as ECSA increases, the overpotential decreases significantly. However, as ECSA increases further, there is little to no change in the electrode overpotential. This suggests an upper limit to the useable surface area, beyond which further increases in surface area do not improve performance. Thus, in order to further improve performance beyond this point, enhancements in mass transport and reaction rates are necessary. **Figure IV-2(b)** illustrates how changing mass transfer rate (with the interstitial velocity) and reaction rate (with the heterogeneous standard kinetic rate constant) alter the value of maximum useable surface area. The standard rate constant was varied from 10^{-10} to 10^{-6} m s^{-1} (10^{-8} to 10^{-4} cm s^{-1}), intended to represent a reasonable range of standard rate constants for typical RFB active species[121]—however, for rate constants beyond 10^{-6} m s^{-1} the model is no longer valid, as this would result in Damköhler number (ratio of kinetic rate to diffusion) scaling of about 1 (Da

~ 1); in this regime, transport limitations in the boundary layers becomes significant, which would require a multi-length scale model beyond the scope of this work.[122] However, we expect that the observed trend of decreasing maximum useable surface area with increasing rate constant to continue, indicating that faster reactions require less surface area for similar performance. To investigate impact of mass transport, the interstitial velocity within the slab was varied from 10^{-4} to 10^1 m s^{-1} (10^{-2} to 10^2 cm s^{-1}), intended to roughly span the transport properties reported in redox flow cells.[87] We find that the maximum useable surface area decreases as the interstitial velocity decreases, indicating that mass transfer losses inhibit the accessible amount of surface area that can be utilized. As this model neglects to account for differences in electrode topology, these results represent an optimistic scenario where all surface area is accessible; however, we find that even at these conditions there is a limit of useable surface area, and increasing surface area beyond this point will result in only curtailed performance improvements. This model suggests that once a reasonable accessible surface area ($\sim$10 m^2 g^{-1}) has been achieved, the focus of electrode engineering and design should shift towards improving kinetics and mass transport properties to maximize performance.
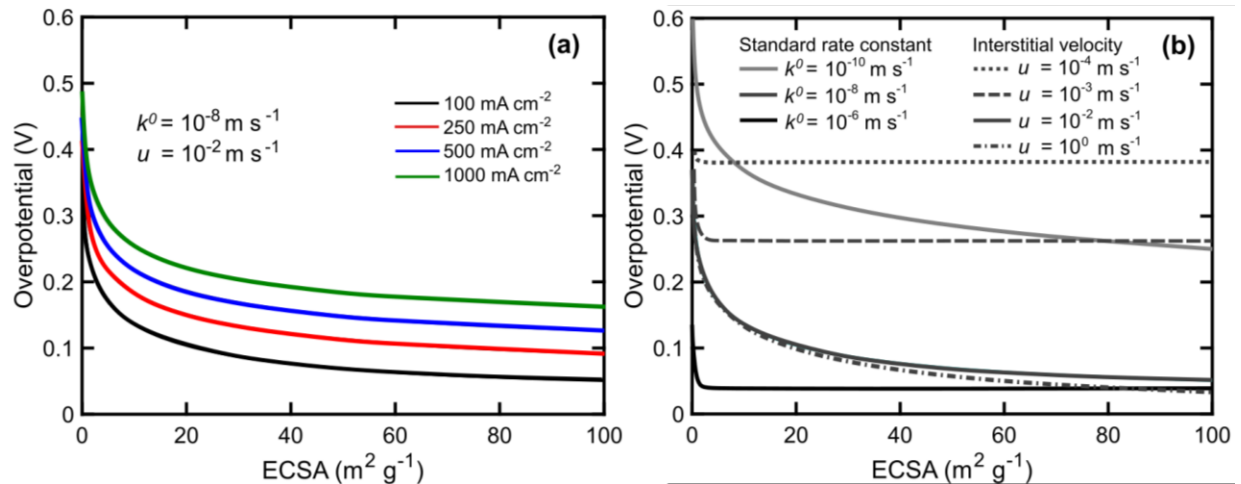
Figure IV-2 *Electrode overpotential at different currents assuming Butler-Volmer kinetics and modeled using a slab Thiele modulus to approximate the effect on ECSA. (a) Overpotential vs. ECSA with constant standard rate constant of 10^{-8} m s^{-1} and interstitial velocity of 10^{-2} m s^{-1}. Initially, the overpotential decreases significantly as ECSA increases, but further increases in ECSA do not significantly affect the overpotential, indicating there is a maximum useable surface area. (b) Overpotential as a function of surface area at 100 mA cm^{-2} with varying standard rate constants and interstitial velocities. While k^0 is*

varied, u *is fixed at 10^{-2} m s^{-1}; while* u *is varied,* k^0 *is held at 10^{-8} m s^{-1}. The maximum useable surface area decreases as rate constant increases and decreases as the velocity decreases.*

4. Conclusions

Here we have developed a convection-reaction model that can be used to study the impact of surface area, catalysis, and mass transport on electrode performance. Active species consumption is modeled as exponential decay of concentration through the slab; the rate of this decay is governed by the dimensionless parameter kL/u, the rate of kinetics to mass transport. As the standard rate constant increases, rate of consumption increases; as interstitial velocity increases, bulk concentration is replenished and the decay is lessened. The impact of surface area on performance is studied using an effectiveness factor to calculate current density within the slab at varying ECSAs. Even when assuming that all surface area is accessible, we find that ECSA improves electrode performance only to a certain threshold, beyond which overpotential remains constant as a function of ECSA. We postulate that kinetic and mass transfer losses inhibit use of additional surface area; in other words, once the concentration within the slab is sufficiently depleted, additional surface area cannot be used for reactions and thus does not contribute to performance. Thus, in order to optimize electrode performance, once a reasonable accessible surface area (based on the results of this work, ~10 m^2 g^{-1}) has been achieved, the focus of electrode engineering and design should shift towards improving kinetics via catalysis and mass transport properties to replenish concentration of active species throughout the electrode.

5. Acknowledgments

6. Appendix A: List of symbols and abbreviations

Symbol	Description	Units
x	Position within electrode slab	m
C	Active species concentration	mol m^{-3}
C_{bulk}	Active species bulk concentration	mol m^{-3}
u	Interstitial velocity	m s^{-1}
k	Effective homogeneous rate constant	s^{-1}
k^0	Standard electrochemical rate constant	m^2 s^{-1}
ρ	Density	g m^{-3}
L	Characteristic length scale	m
Ψ	Dimensionless active species concentration	--
ν	Dimensionless position	--
H	Effectiveness factor	--
F	Faraday's constant	C mol^{-1}
i	Current density	A m^{-2}
i_{ref}	Current density at reference concentration	A m^{-2}
i_0	Exchange current density	A m^{-2}
m	Electrode mass	g
α_f	Forward charge transfer coefficient	--
α_r	Reverse charge transfer coefficient	--
η	Electrode overpotential	V
n	Number of electrons transferred	mol e$^-$ mol^{-1}
R	Universal gas constant	J mol^{-1} K^{-1}
T	Absolute temperature	K

V. Deposition and Plating for Metal and Metal-Decorated Electrode Fabrication

Metal electrodes offer several potential advantages over carbon electrodes, providing various possible catalytic functional groups and improving stability in certain systems. In order to pair these advantages with the existing assets and our growing understanding of carbon electrodes based on the previous chapters, we synthesize metal electrodes via deposition on carbon fiber substrates. In particular, nickel catalysts were deposited electrochemically using the wood's nickel strike industrial plating bath. We tested several different types of commercially available carbon electrodes as deposition substrates, including AvCarb 1071 cloth, SGL 29AA paper, and Toray 60 paper. Of the electrodes tested, AvCarb 1071 showed the best performance in a polysulfide electrolyte, showing significant reductions in overpotential compared to the baseline nickel foam. However, all nickel electrodes did not perform as well as cobalt-decorated electrodes for the polysulfide system, indicating that cobalt is a superior catalyst for the polysulfide redox reaction. In subsequent testing of nickel deposited electrodes in permanganate electrolyte, we showed that nickel-deposited AvCarb 1071 outperforms stainless steel weave electrodes, the previous best performing material.

In addition to successful *ex-situ* deposition of nickel in a 3-electrode set-up, nickel was deposited *in-situ* in a 2-electrode flow cell. *Ex-situ* and *in-situ* nickel-deposited AvCarb 1071 electrodes show comparable performance. These results can enable *in-situ* performance recovery by periodically re-depositing nickel that may be oxidized by the corrosive permanganate electrolyte. The goal of this work is to show the potential for using electrochemical deposition to improve electrode catalysis and performance, enabling large system performance gains.

1. Background

Metal electrodes have potential to offer improved performance for certain RFB systems, particularly for those electrolytes in which carbon is not stable or not catalytically active. Metal catalysts have been incorporated into electrodes via a variety of fabrication methods, including electrodeposition, electrospinning, and impregnation/drying.[19] Electrodeposition is advantageous over other fabrication methods, as the thickness and mass of the metal catalyst may be controlled via deposition parameters, including deposition time, current, and electrolyte composition.[20] Further, the electrodeposition process is easily scalable and does not require any post-treatment

steps, making it ideal for large-scale electrode production.[21] Metal electrocatalysts have the potential to significantly improve standard electrode performance—for example, precious metal electrodes have been shown to be superior catalysts for the vanadium redox reaction.[22] In fact, the majority of papers published which investigate the use of metal electrodes in RFBs focus on the vanadium RFB.[19] Metal catalysts have been shown to augment other redox reactions of interest, including polysulfide;[23] hence metal electrodeposition may be used as a tool to augment performance of these novel electrolytes, making them more viable for commercial adoption.

Electrodeposition is typically carried out in a 3-electrode set-up, where the deposition substrate is the working electrode. While many deposition reactions are potentiostatic, i.e. the deposition voltage is held constant, it is convenient to use galvanostatic or constant current operation to avoid complications in plating potential due to ohmic resistance or electric field in the plating bath.[123] Galvanostatic operation also enables electrodeposition without the use of a reference electrode, which may facilitate *in-situ* deposition in a 2-electrode systems.

Here, we investigate the potential for electrochemically deposited nickel electrodes for use in a novel polysulfide-permanganate redox flow battery. We tested several different types of carbon paper electrodes as deposition substrates, including AvCarb 1071 cloth, SGL 29AA paper, and Toray 60 paper. We demonstrated the ability to deposit nickel in a 2-electrode flow cell, finding that electrodes deposited in this manner perform equivalently to electrode deposited in a 3-electrode set-up. We tested the performance and stability of these materials in a polysulfide and permanganate electrolytes to determine their efficacy for a polysulfide-permanganate flow battery. Polysulfide redox is kinetically slow, while carbon electrodes are not stable in permanganate,[124] thus metal electrodes have great potential to improve the viability of this system.

2.   Experimental methods

2.1.   Nickel deposition

A 3-electrode set-up was used for deposition of nickel onto the working electrode substrate. Nickel foam, nickel foil, or a nickel bar were used as a counter electrode (to replenish depleted nickel in the solution) and a Ag/AgCl electrode (BASi, Inc.) was used as a reference electrode. The plating solution and all electrodes were immersed in Wood's Nickel Strike, an industrial plating solution, which was made in the lab using nickel(II) chloride (98%, Sigma Aldrich) in concentration of 1.8 M and hydrochloric acid (37%, Sigma Aldrich) at a concentration of 3 M dissolved in DI water (Milli-Q Millipore, 18.2 MΩ-cm). For the 2.55 cm^{-2} samples, a reductive

current density of 20 mA cm^{-2} was applied for 2 minutes, followed by a reductive current density of 200 mA cm^{-2} for 4 minutes. For the 25 cm^{-2} samples, we were unable to apply the equivalent current density due to potentiostat limitations; instead, deposition was carried out for a longer time such that an equivalent number of coulombs of charge were passed.

Alternatively, nickel was deposited in a 2-electrode cell, which contained the substrate on the positive (working) side and a counter electrode on the negative side. The counter electrode was a thermally treated Toray Carbon Paper TGH-H-60 (Fuel Cell Store). Wood's Nickel Strike was used as the electrolyte on the positive (working) side, and 3 M sodium hydroxide in DI water (NaOH pellets 98%, Sigma Aldrich) was used on the negative (counter) side. Deposition occurred under flow, at 10 mL min^{-1} in the research-scale flow cell (2.55 cm^2 active area) and 100 mL min^{-1} in the subscale (25 cm^2 active area) cell. Interdigitated flow fields were used in both cells. The positive and negative sides of the cell were separated by a Nafion 115 membrane (Fuel Cell Store) used as received.

Substrates used for deposition were various commercially available carbon papers, which were either used as received or thermally treated at 400 °C for 30 h prior to deposition. Carbon papers tested include AvCarb 1071 HCB, Toray TGH-60-HP, and Sigracet SGL 29AA, all purchased from Fuel Cell Store.

2.2. Electrode characterization

Prior to cell testing, the electrodes were characterized using microscopic, spectroscopic, and analytical techniques. Electrode microstructure and morphology were characterized by scanning electron microscopy (SEM) / energy-dispersive X-ray analysis (EDX). SEM/EDX measurements were performed using a FESEM Ultra Plus (Zeiss, Germany) with an electron energy of 5 keV, an aperture of 30 μm, and a gun-to-sample distance of ca. 5 mm. The samples were adhered to the stage with double-sided conductive carbon tape (Ted Pella Inc.). X-ray Diffraction data was gathered on the PANalytical X'Pert PRO X-Ray Powder Diffractometer (Malvern, United Kingdom) using copper Kα radiation (λ=1.5418 Å) set to 40 kV and 4 mA. The 2θ range of the XRD spectra were 5-100° and the rate was ca. 10° min^{-1}. XRD spectra were analyzed using High Score Plus software (Malvern), and reference spectra for cubic nickel, hexagonal carbon, and graphitic carbon were obtained from the International Centre for Diffraction Data (ICDD) database. Electrodes were weighed before and after deposition (n=4) to determine the amount of nickel deposited.

2.3. Evaluation of electrode performance via flow cell testing

Ni-deposited electrodes were tested in polysulfide and/or permanganate solutions. Sodium polysulfide electrolytes (2.1 M Na_2S_x/3 M NaOH) were prepared by mixing stoichiometric ratios of sodium sulfide ($Na_2S \bullet 9 H_2O$, >99.999%, Sigma Aldrich) and elemental polysulfide (sublimed polysulfide powder, 98%, Alfa Aesar), along with sodium hydroxide in DI water. Sodium permanganate solutions (2.1 M $KMnO_4$/3 M NaOH) were prepared by mixing sodium permanganate monohydrate ($\geq$ 97%, Sigma Aldrich), and sodium hydroxide in DI water. All samples were prepared in polypropylene centrifuge tubes (VWR). All solutions were degassed using humidified nitrogen for one minute per every milliliter before use.

Two flow cell configurations were used for testing: a research-scale flow cell (2.55 cm^2 active area) and subscale flow cell (25 cm^2 active area), both with zero-gap architecture.[24] In the research-scale cell, Tokai G347B resin-impregnated graphite plates of 3.18 mm thickness (Tokai Carbon Co., Tokyo, Japan) milled with an interdigitated pattern served as current collectors and flow fields, while polypropylene flow diffusers served as backing plates. Electrolyte flow rate was set at 10 mL min^{-1}. A peristaltic pump (Masterflex L/S Series, Cole-Parmer) and Norprene tubing (1.6 mm inner diameter, Cole-Parmer) were used to circulated electrolyte through the flow cell and reservoirs. Polytetrafluoroethylene (PTFE) gaskets (of thicknesses sized for each electrode) compressed electrodes by 20% and prevented electrolyte leaking. Two layers of carbon paper electrodes (1.5 cm × 1.7 cm) were used for each electrode, positive and negative. In the subscale cell, resin-impregnated graphite plates of 0.318 cm thickness milled with an interdigitated pattern served as flow fields, while copper plates served as current collectors. Electrolyte flow rate was set at 100 mL min^{-1}. A diaphragm pump (FF 12 series, KNF Neuberger) and Norprene tubing (3.1 mm inner diameter, Cole-Parmer) were used to circulated electrolyte through the flow cell and reservoirs. Polytetrafluoroethylene (PTFE) gaskets (of thicknesses sized for each electrode) compressed electrodes by 20% and prevented electrolyte leaking in both systems. Nafion 115 membranes soaked in 3 M NaOH for 3+ days were used as separators.

Galvanostatic polarization was carried out to determine electrode performance for both charge and discharge of the cell, both in a symmetric polysulfide configuration and in a full cell. Polarization analyses were performed at 50% SOC. In the full cell, the SOC started at 100%, and was discharged to 50% SOC at 20 mA cm^{-2} for 5.25 h. The cell was then subjected to increasing magnitudes of current density from 10 mA cm^{-2} to 120 mA cm^{-2} in increments of 10 mA cm^{-2},

alternating between positive and negative currents which were each held for 2 minutes (to allow the potential to stabilize), followed by another 2-minute constant current holds of equal magnitude but opposite sign to return the cell to 50% SOC before the next step.

3. *Results and discussion*

3.1. Structure and efficiency of nickel deposits

Electrode mass was recorded before and after deposition to determine the amount of nickel that was added via deposition, and to compare efficiency of deposition across electrode types (**Table V-1**). On AvCarb 1071 and SGL 29AA, an average deposited mass of ~5 mg cm^{-2} is achieved, compared to a slightly lower deposited mass on the Toray 60 paper. AvCarb 1071 has the most variation across samples; this is likely due to the large pores within the sample, which may lead to diffusion limitations that prevented uniform deposition within the bulk of the electrode.[89]

Table V-1 – *Average mass of nickel deposited on each electrode type, normalized by the geometric electrode area (n=4).*

Electrode	Average deposited mass (mg cm^{-2})
AvCarb 1071	4.7±2.7
Toray TGP-H-60	3.4±0.5
Sigracet SGL 29AA	4.8±0.7

In order to characterize the nickel deposits, we investigated their structure using SEM (**Figure V-1**). We find that nickel is deposited on the surfaces of each electrode, regardless of binder content; in other words, the nickel does not appear to selectively adhere to specific surface sites. However, we find that the deposits are somewhat rough, and there is variability in the structure across the different electrode types—for example, the deposit on the surface of AvCarb 1071 is cracked (**Figure V-1(d)**) while the deposit on the surface of the Toray appears to contain crystalline structures (**Figure V-1(e)**).
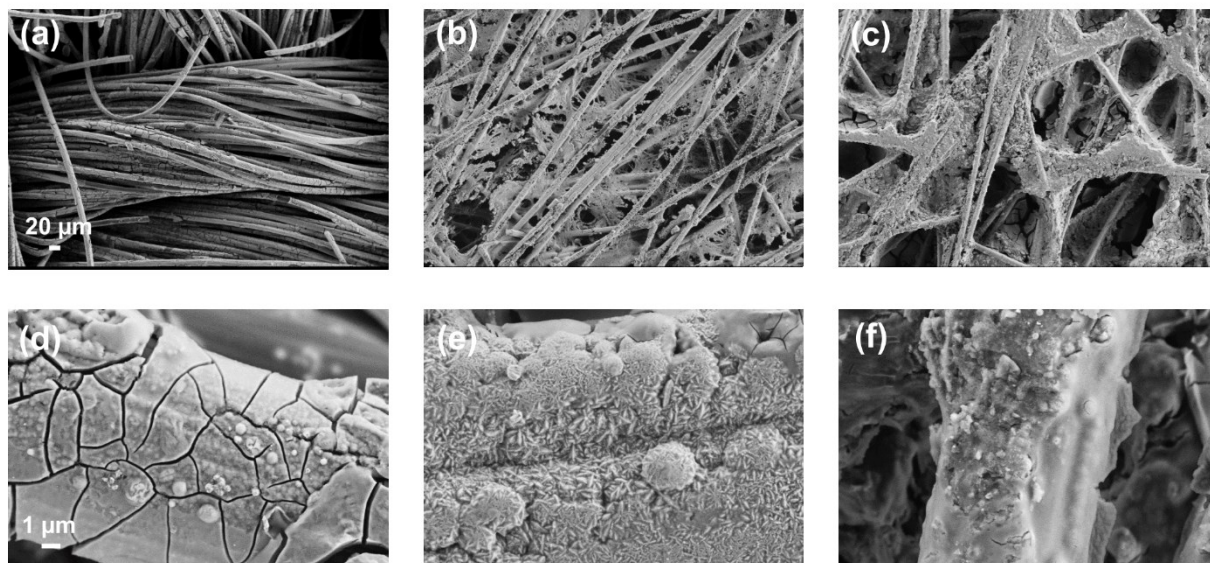
Figure V-1 *SEM images of metal deposited electrodes – (a), (d) AvCarb 1071, (b), (e) Toray 60, (c), (f) SGL 29AA.*

It is possible that the variation surface features seen in **Figure V-1** are due to impurities, such as nickel oxide. To determine whether the deposit was primarily nickel or contained impurities, we investigated the nature of the deposited nickel using XRD (**Figure V-2**). XRD results show that each nickel deposit contains cubic nickel, and the XRD spectra are relatively consistent across electrode types. The lack of background noise and absence of peak shifting indicate that the majority of the deposit is cubic nickel, rather than impurities such as nickel oxide.
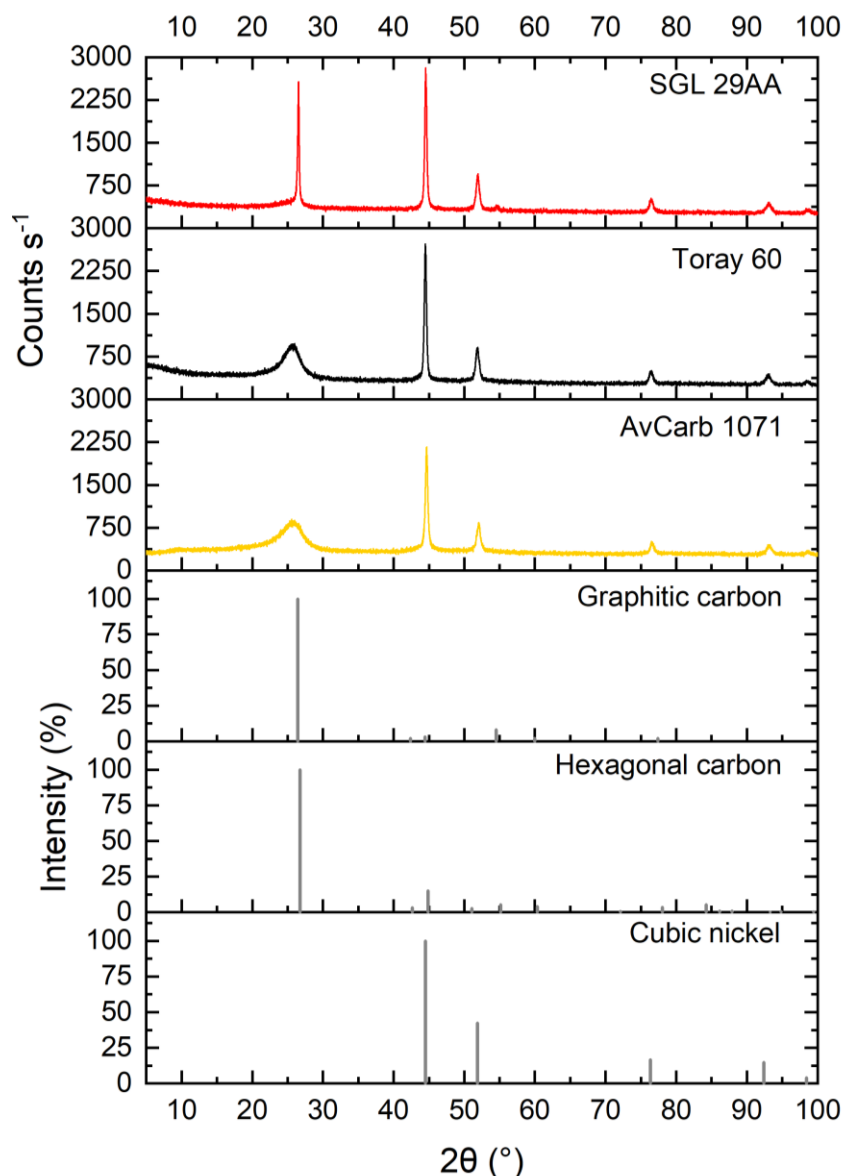
Figure V-2 *XRD spectra of nickel-deposited electrodes AvCarb 1071 (yellow), Toray 60 (black), and SGL 29AA (red). Reference peaks from ICDD are shown for cubic nickel, hexagonal carbon, and graphitic carbon.*

3.2. *In-situ* deposition of nickel in a flow cell

In addition to *ex-situ* 3-electrode deposition, we investigated *in-situ* nickel deposition in a 2-electrode flow cell set-up. This deposition technique has the potential to reverse the effects of electrode degradation over extended cycling, enabling RFB servicing without the need to dismantle the system. We successfully deposited nickel on an AvCarb 1071 carbon cloth working electrode in a 2.55 cm^2 cell (**Figure V-3**). From **Figure V-3(a)** one can clearly see striations in the deposit, most likely due to contact with the flow field interfering with the deposit. **Figure V-3(b)**

shows that there is some deposition on the flow field itself; however, the photo was taken after nickel deposition on 6 different electrode samples using the same flow field, and the deposition did not accumulate to the point that it interfered with electrolyte flow.

The performance of the *in-situ* deposited electrodes was compared to the 3-electrode deposited electrodes (*vide supra*) in a symmetric polysulfide flow cell (**Figure V-3(c)**). We find that the performance of electrodes synthesized with both deposition methods is similar, illustrating the viability of *in-situ* flow cell deposition.
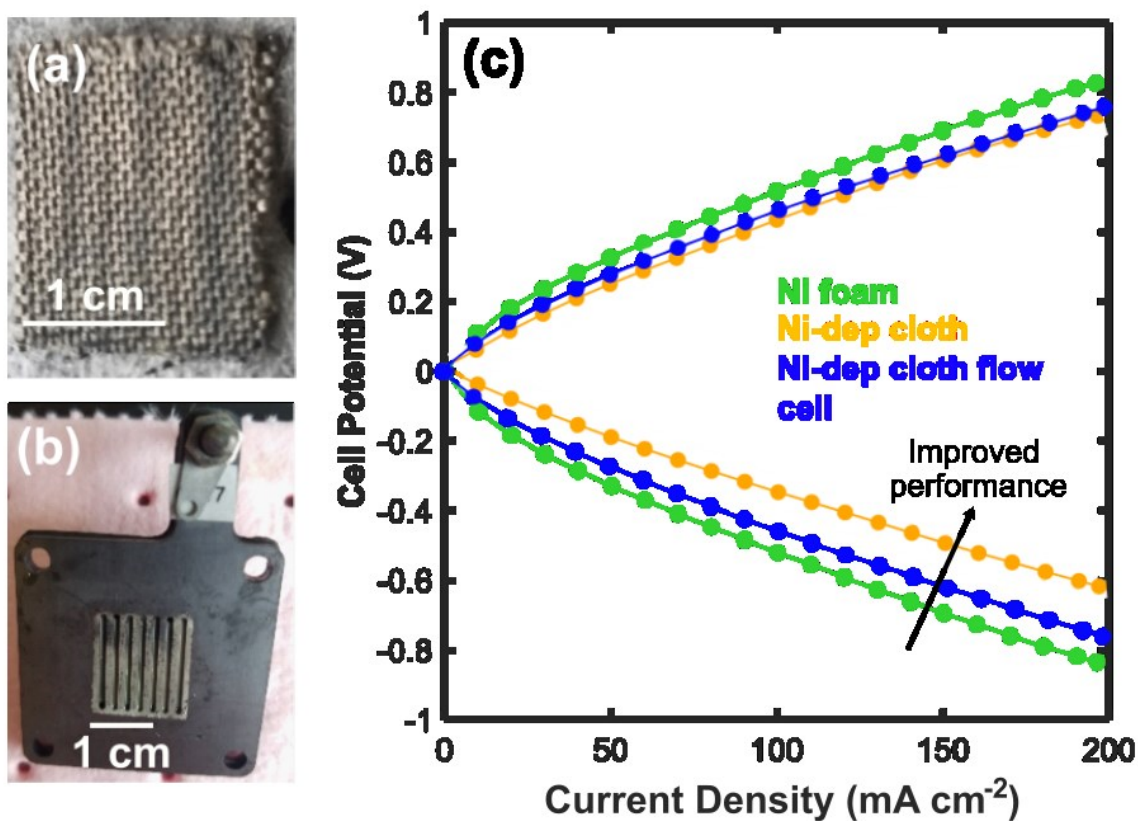
Figure V-3 *(a) AvCarb 1071 electrode after nickel deposition in a flow cell. (b) Flow field used on the deposition side of the flow cell. (c) Polarization curves in a 2-electrode symmetric polysulfide flow cell, comparing nickel-deposited cloth electrodes synthesized in a flow cell (blue) to 3-electrode synthesized nickel-deposited electrodes (yellow) and nickel foam electrodes (green) for reference.*

3.3.   Testing deposits on varying commercial carbon papers

Each type of Ni-deposited electrode was compared in a symmetric polysulfide cell. Polysulfide was chosen as the active species as the polysulfide redox reaction is kinetically limiting as compared to permanganate, thus improvements in polysulfide catalysis will result in the largest system performance gains. We find all nickel-deposited electrodes outperform the baseline of MTI

1.6 mm-thick Ni-foam (**Figure V-4**). We postulate that the soft carbon electrodes allow greater compression and enhanced contact between flow field, electrode, and membrane, thereby reducing contact resistance that leads to overpotential losses. Further, AvCarb 1071 offers the best performance; this is likely due to the enhanced mass transfer facilitated by the bimodal pore-size distribution of the carbon cloths compared to other types of carbon papers.[89]
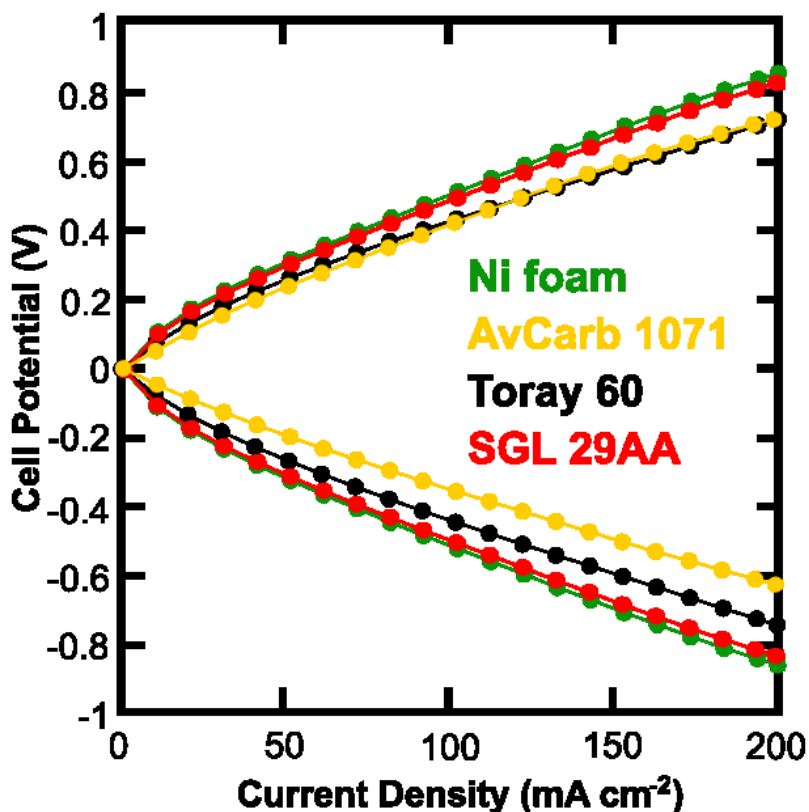
Figure V-4 *Polarization results of a symmetric polysulfide cell for nickel foam (green) and nickel deposited carbons: AvCarb 1071 (yellow), Toray 60 (black), and SGL 29AA (red).*

Previous work has shown that cobalt (Co) is a promising catalyst for the polysulfide redox reaction.[23] In order to compare performance of the nickel-deposit electrodes in polysulfide to the state-of-the-art, symmetric polysulfide polarization experiments were performed at room temperature in a large (25 cm^2) set-up and compared the results to Co-decorated Toray-60 electrodes with equivalent (5 mg cm^{-2}) loading (synthesized via electroless deposition by Raytheon Technologies research center, adapted from Zhou *et al.*[125]) (**Figure V-5**). Flow cell testing was performed by Raytheon Technologies. Despite the relative improvement in the performance of the nickel-deposited carbon electrodes compared to nickel foam, nickel-deposited electrodes perform

significantly worse in comparison to Co-decorated carbon. Compared to nickel, cobalt appears to be a superior catalyst for the polysulfide reaction; thus, going forward we chose to focus effort on electrode development for the permanganate reaction.
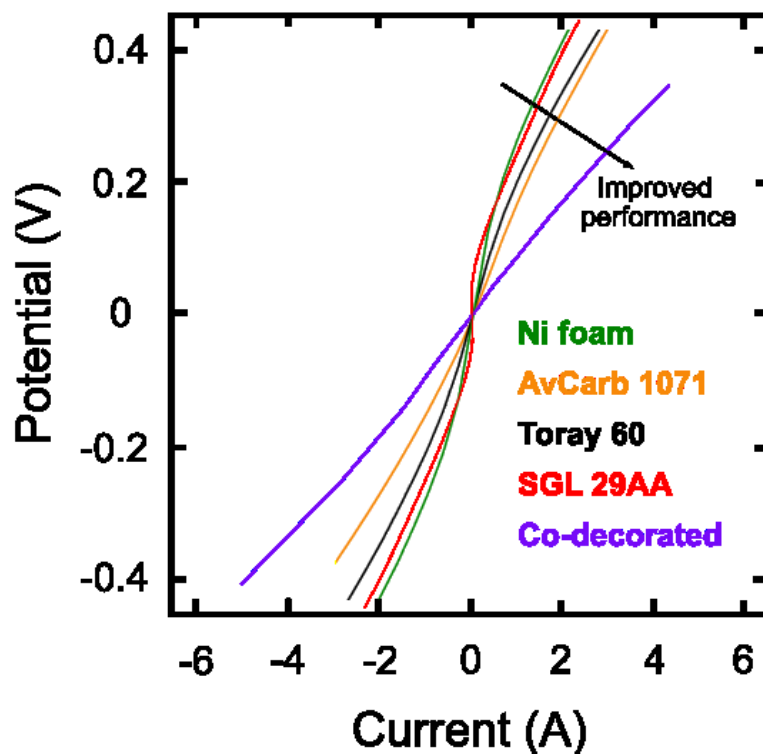
Figure V-5 *Polarization of polysulfide symmetric cell with nickel foam (green); nickel-deposited AvCarb 1071 (yellow), Toray 60 (black), and SGL29AA (red); and Co-decorated Toray 60 electrodes (purple).*

3.4.   Performance of nickel-deposited electrodes in permanganate

In order to test the Ni-deposited electrodes in permanganate, we compared them to stainless-steel (SS)-weave electrodes, which were the previous best performing material, in a polysulfide-permanganate flow battery of active area 25 cm^2 at a temperature of 50 °C (**Figure V-6**). We find that, compared to the SS-weave electrodes, nickel-deposited electrodes significantly decrease system overpotential, due to a reduction in ohmic resistance: 2 Ω cm^2 for the flow cell with the nickel-deposited electrodes versus 2.5 Ω cm^2 for the flow cell with SS-weave electrode. This phenomenon is likely due to decreased contact resistance—carbon electrodes are more flexible and more easily compressed than metal electrodes, and we anticipate that increased compression results in improved contact between electrode, membrane, and flow field.[126]
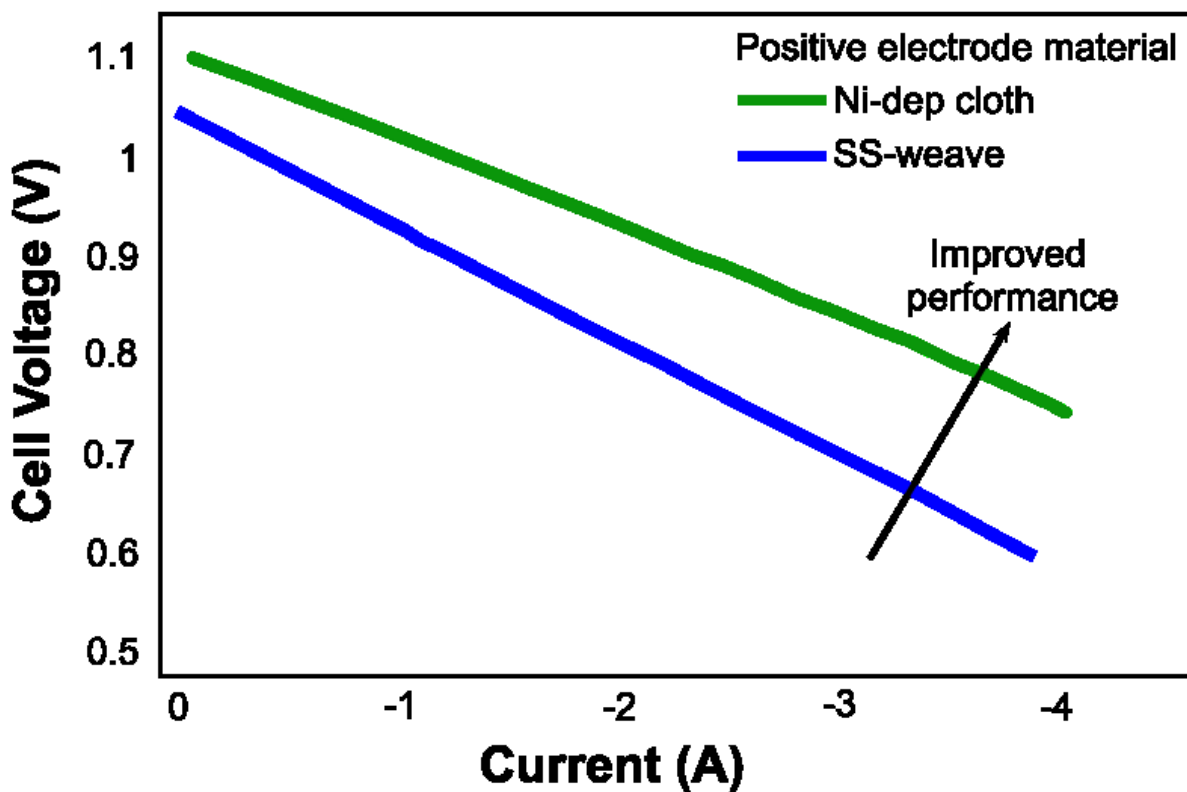
Figure V-6 *– Polarization curve of 25 cm² S-Mn flow cell with nickel-deposited electrodes (red) and the previous standard stainless-steel weave electrodes (blue) on the positive (permanganate) side. Overpotential is reduced when using nickel-deposited electrodes as compared to the SS-weave.*

4. Conclusions

Metal electrodes offer several potential advantages over carbon electrodes, providing various possible catalytic functional groups and improved stability in certain systems. In order to pair these advantages with the existing assets and our enhanced understanding of carbon electrodes, metal electrodes were synthesized via deposition on carbon fiber substrates. In particular, nickel electrodes were deposited electrochemically using the Wood's Ni-Strike industrial plating bath for use in a novel polysulfide-permanganate flow battery. Nickel was successfully deposited both *ex-situ* in a 3-electrode set-up and *in-situ* in a 2-electrode flow cell. *Ex-situ* and *in-situ* nickel-deposited AvCarb 1071 electrodes showed comparable performance. These results can enable *in-situ* performance recovery by periodically re-depositing nickel that may be oxidized by the corrosive permanganate electrolyte. Additionally, nickel-deposited AvCarb 1071 electrodes show enhanced performance compared to the previous best-performing positive electrode material.

These results illustrate the potential for using electrochemical deposition of catalysts to improve electrode catalysis and performance, enabling large system performance gains.

5.   *Acknowledgements*

VI.   Conclusions & Future Work

The overarching goal of this thesis work was to develop a deeper understanding of the influence that electrode properties have on RFB performance. The structure-function relationships of electrodes may be used to optimize and predict system performance. I conclude by providing some perspective on why understanding the physical mechanisms at play within the electrode is necessary for upgrading, designing, and synthesizing next-generation materials.

The de facto state of electrode research is to begin with a pristine, untreated carbon paper or felt, modify it in some way (e.g., thermal treatment, catalyst deposition), and compare the performance of the modified material to the pristine material. Inevitably, the treated materials outperform the untreated materials. However, due to differences in electrolyte composition, membrane selection, and flow-field design—among other system properties—it is nearly impossible to compare electrode performance across published studies. In order to circumvent this problem, we must develop or identify system agnostic electrode properties that can be used as electrode performance indicators.

In this work, I have shown the potential for using certain fundamental electrode properties as predictors of performance. Based on the results of this thesis and other works, we are able to predict that improved oxygen functional groups will enhance performance of kinetically limited systems (i.e., vanadium), but we are unable to make performance predictions for kinetically facile systems (i.e., TEMPO). Thus new, more reliable physical property indicators that are system agnostic must be identified or developed to predict performance of RFB electrodes. Additionally, although we are able to make certain system-specific estimates that are qualitative in nature and can be used to compare material sets, we cannot yet quantitatively predict the electrode overpotential *a priori*. The advancement of models or perhaps even simple mathematical relationships to predict electrode overpotential taking electrode and electrolyte properties as inputs will enable targeted electrode design and development.

There has been major growth in recent years in modeling of RFB electrolyte transport in porous materials that may serve as a starting point. One shortcoming of these models is the use of total surface area in calculations, typically as rendered by tomographic images. As discussed in **Chapter III** of this thesis, the physical surface area is a significant overestimation of the ECSA that is actually contributing to reaction catalysis. One facile improvement to these models would be to adopt ECSA as the standard surface area for reactions. One could envision other potential

improvements to modeling electrode activity, including pairing surface characterization techniques, such as EDX or XPS, with electrode modeling, enabling the capture of the kinetic contributions of reaction sites added via treatment.

Although I have primarily discussed modification of commercially available electrodes in this thesis, I firmly believe that continued study of the physical and chemical mechanisms of electrode catalysis and transport will lead to development of materials that are uniquely tailored for use in RFBs. Many commonly used carbon electrodes have been designed for use in polymer electrolyte fuel cells, and thus are engineered to have properties that are at cross-purposes for RFB performance. By continuing to expand our fundamental understanding of kinetics and transport within complex porous media, we will be prepared to design novel porous material classes that are suited for use in RFBs and other even more challenging electrochemical environments.

References

(1)   Yang, Z.; Zhang, J.; Kintner-Meyer, M. C. W.; Lu, X.; Choi, D.; Lemmon, J. P.; Liu, J. Electrochemical Energy Storage for Green Grid. *Chem. Rev.* **2011**, *111* (5), 3577–3613. https://doi.org/10.1021/cr100290v.

(2)   Skyllas-Kazacos, M.; Chakrabarti, M. H.; Hajimolana, S. A.; Mjalli, F. S.; Saleem, M. Progress in Flow Battery Research and Development. *J. Electrochem. Soc.* **2011**, *158* (8), R55. https://doi.org/10.1149/1.3599565.

(3)   Wang, W.; Luo, Q.; Li, B.; Wei, X.; Li, L.; Yang, Z. Recent Progress in Redox Flow Battery Research and Development. *Adv. Funct. Mater.* **2013**, *23* (8), 970–986. https://doi.org/10.1002/adfm.201200694.

(4)   Yang, Z.; Liu, J.; Baskaran, S.; Imhoff, C. H.; Holladay, J. D. Enabling Renewable Energy- and the Future Grid-with Advanced Electricity Storage. *JOM* **2010**, *62* (9), 14–23. https://doi.org/10.1007/s11837-010-0129-0.

(5)   Kear, G.; Shah, A. A.; Walsh, F. C. Development of the All-Vanadium Redox Flow Battery for Energy Storage: A Review of Technological, Financial and Policy Aspects. *Int. J. Energy Res.* **2012**, *36*, 1106–1120.

(6)   Darling, R. M.; Gallagher, K. G.; Kowalski, J. A.; Ha, S.; Brushett, F. R. Pathways to Low-Cost Electrochemical Energy Storage : A Comparison of Aqueous and Nonaqueous Flow Batteries. *Energy Environ. Sci.* **2015**, *7*, 3459–3477. https://doi.org/10.1039/C4EE02158D.

(7)   Perry, M. L.; Weber, A. Z. Advanced Redox-Flow Batteries: A Perspective. *J. Electrochem. Soc.* **2016**, *163* (1), A5064–A5067. https://doi.org/10.1149/2.0101601jes.

(8)   Chakrabarti, M. H.; Brandon, N. P.; Hajimolana, S. A.; Tariq, F.; Yufit, V.; Hashim, M. A.; Hussain, M. A.; Low, C. T. J.; Aravind, P. V. Application of Carbon Materials in Redox Flow Batteries. *J. Power Sources* **2014**, *253*, 150–166. https://doi.org/10.1016/j.jpowsour.2013.12.038.

(9)   Kim, K. J.; Park, M.-S.; Kim, Y.-J.; Kim, J. H.; Dou, S. X.; Skyllas-Kazacos, M. A Technology Review of Electrodes and Reaction Mechanisms in Vanadium Redox Flow Batteries. *J. Mater. Chem. A* **2015**, *3* (33), 16913–16933. https://doi.org/10.1039/C5TA02613J.

(10)   SGL Group. SIGRACET GDL for Fuel Cells, Electrolyzers, and Batteries. 2016.

(11)   Sun, B.; Skyllas-Kazacos, M. Modification of Graphite Electrode Materials for Vanadium Redox Flow Battery Application—I. Thermal Treatment. *Electrochimica Acta* **1992**, *37* (7), 1253–1260. https://doi.org/10.1016/0013-4686(92)85064-R.

(12)   Pezeshki, A. M.; Clement, J. T.; Veith, G. M.; Zawodzinski, T. A.; Mench, M. M. High Performance Electrodes in Vanadium Redox Flow Batteries through Oxygen-Enriched Thermal Activation. *J. Power Sources* **2015**, *294*, 333–338. https://doi.org/10.1016/j.jpowsour.2015.05.118.

(13)   Liu, T.; Li, X.; Xu, C.; Zhang, H. Activated Carbon Fiber Paper Based Electrodes with High Electrocatalytic Activity for Vanadium Flow Batteries with Improved Power Density. *ACS Appl. Mater. Interfaces* **2017**, acsami.6b14478. https://doi.org/10.1021/acsami.6b14478.

(14) Flox, C.; Rubio-García, J.; Skoumal, M.; Andreu, T.; Morante, J. R. Thermo-Chemical Treatments Based on NH3/O2 for Improved Graphite-Based Fiber Electrodes in Vanadium Redox Flow Batteries. *Carbon* **2013**, *60*, 280–288. https://doi.org/10.1016/j.carbon.2013.04.038.

(15) Langner, J.; Bruns, M.; Dixon, D.; Nefedov, A.; Wöll, C.; Scheiba, F.; Ehrenberg, H.; Roth, C.; Melke, J. Surface Properties and Graphitization of Polyacrylonitrile Based Fiber Electrodes Affecting the Negative Half-Cell Reaction in Vanadium Redox Flow Batteries. *J. Power Sources* **2016**, *321*, 210–218. https://doi.org/10.1016/j.jpowsour.2016.04.128.

(16) Kabtamu, D. M.; Chen, J. Y.; Chang, Y. C.; Wang, C. H. Water-Activated Graphite Felt as a High-Performance Electrode for Vanadium Redox Flow Batteries. *J. Power Sources* **2017**, *341*, 270–279. https://doi.org/10.1016/j.jpowsour.2016.12.004.

(17) Kil, D.; Lee, H. J.; Park, S.; Kim, S.; Kim, H. Synthesis of Activated Graphite Felts Using Short-Term Ozone/Heat Treatment for Vanadium Redox Flow Batteries. *J. Electrochem. Soc.* **2017**, *164* (13), A3011–A3017. https://doi.org/10.1149/2.0311713jes.

(18) Rabbow, T. J.; Trampert, M.; Pokorny, P.; Binder, P.; Whitehead, A. H. Variability within a Single Type of Polyacrylonitrile-Based Graphite Felt after Thermal Treatment. Part I: Physical Properties. *Electrochimica Acta* **2015**, *173*, 24–30. https://doi.org/10.1016/j.electacta.2015.05.058.

(19) Amini, K.; Gostick, J.; Pritzker, M. D. Metal and Metal Oxide Electrocatalysts for Redox Flow Batteries. *Adv. Funct. Mater.* **2020**, *30* (23), 1910564. https://doi.org/10.1002/adfm.201910564.

(20) *Rotating Electrode Methods and Oxygen Reduction Electrocatalysts*; Xing, W., Yin, G., Zhang, J., Eds.; Elsevier: Amsterdam, 2014.

(21) Su, J.; Ge, R.; Dong, Y.; Hao, F.; Chen, L. Recent Progress in Single-Atom Electrocatalysts: Concept, Synthesis, and Applications in Clean Energy Conversion. *J. Mater. Chem. A* **2018**, *6* (29), 14025–14042. https://doi.org/10.1039/C8TA04064H.

(22) Wei, L.; Zhao, T.; Zeng, L.; Zhou, X.; Zeng, Y. Titanium Carbide Nanoparticle-Decorated Electrode Enables Significant Enhancement in Performance of All-Vanadium Redox Flow Batteries. *Energy Technol.* **2016**, *4* (8), 990–996. https://doi.org/10.1002/ente.201600016.

(23) Su, L.; Badel, A. F.; Cao, C.; Hinricher, J. J.; Brushett, F. R. Toward an Inexpensive Aqueous Polysulfide–Polyiodide Redox Flow Battery. *Ind. Eng. Chem. Res.* **2017**, *56* (35), 9783–9792. https://doi.org/10.1021/acs.iecr.7b01476.

(24) Aaron, D. S.; Liu, Q.; Tang, Z.; Grim, G. M.; Papandrew, A. B.; Turhan, A.; Zawodzinski, T. A.; Mench, M. M. Dramatic Performance Gains in Vanadium Redox Flow Batteries through Modified Cell Architecture. *J. Power Sources* **2012**, *206*, 450–453. https://doi.org/10.1016/j.jpowsour.2011.12.026.

(25) Liu, Q. H.; Grim, G. M.; Papandrew, A. B.; Turhan, A.; Zawodzinski, T. A.; Mench, M. M. High Performance Vanadium Redox Flow Batteries with Optimized Electrode Configuration and Membrane Selection. *J. Electrochem. Soc.* **2012**, *159* (8), A1246–A1252. https://doi.org/10.1149/2.051208jes.

(26) Darling, R. M.; Perry, M. L. The Influence of Electrode and Channel Configurations on Flow Battery Performance. *J. Electrochem. Soc.* **2014**, *161* (9), A1381–A1387. https://doi.org/10.1149/2.0941409jes.

(27) Wei, G.; Su, W.; Wei, Z.; Fan, X.; Liu, J.; Yan, C. Electrocatalytic Effect of the Edge Planes Sites at Graphite Electrode on the Vanadium Redox Couples. *Electrochimica Acta* **2016**, *204*, 263–269. https://doi.org/10.1016/j.electacta.2016.04.081.

(28) Hodkiewicz, J. Characterizing Carbon Materials with Raman Spectroscopy. *Prog. Mater. Sci.* **2005**, *50*, 929–961. https://doi.org/10.1088/0022-3727/46/12/122001.

(29) Darling, R. M.; Perry, M. L. Half-Cell, Steady-State Flow-Battery Experiments. *ECS Trans.* **2013**, *53* (7), 31–38.

(30) Pezeshki, A. M.; Sacci, R. L.; Delnick, F. M.; Aaron, D. S.; Mench, M. M. Elucidating Effects of Cell Architecture , Electrode Material , and Solution Composition on Overpotentials in Redox Flow Batteries. *Electrochimica Acta* **2017**, *229*, 261–270. https://doi.org/10.1016/j.electacta.2017.01.056.

(31) Sun, C. N.; Delnick, F. M.; Baggetto, L.; Veith, G. M.; Zawodzinski, T. A. Hydrogen Evolution at the Negative Electrode of the All-Vanadium Redox Flow Batteries. *J. Power Sources* **2014**, *248*, 560–564. https://doi.org/10.1016/j.jpowsour.2013.09.125.

(32) Qu, D. Studies of the Activated Carbons Used in Double-Layer Supercapacitors. *J. Power Sources* **2002**, *109*, 403–411.

(33) Goulet, M. A.; Skyllas-Kazacos, M.; Kjeang, E. The Importance of Wetting in Carbon Paper Electrodes for Vanadium Redox Reactions. *Carbon* **2016**, *101*, 390–398. https://doi.org/10.1016/j.carbon.2016.02.011.

(34) Rabbow, T. J.; Whitehead, A. H. Deconvolution of Electrochemical Double Layer Capacitance between Fractions of Active and Total Surface Area of Graphite Felts. *Carbon* **2017**, *111*, 782–788. https://doi.org/10.1016/j.carbon.2016.10.064.

(35) Wang, S.; Zhao, X.; Cochell, T.; Manthiram, A. Nitrogen-Doped Carbon Nanotube/Graphite Felts as Advanced Electrode Materials for Vanadium Redox Flow Batteries. *J. Phys. Chem. Lett.* **2012**, *3*, 2164–2167. https://doi.org/10.1021/jz3008744.

(36) Nibel, O.; Taylor, S. M.; Pătru, A.; Fabbri, E.; Gubler, L.; Schmidt, T. J. Performance of Different Carbon Electrode Materials: Insights into Stability and Degradation under Real Vanadium Redox Flow Battery Operating Conditions. *J. Electrochem. Soc.* **2017**, *164* (7), A1608–A1615. https://doi.org/10.1149/2.1081707jes.

(37) Pour, N.; Kwabi, D. G.; Carney, T.; Darling, R. M.; Perry, M. L.; Shao-Horn, Y. Influence of Edge-and Basal-Plane Sites on the Vanadium Redox Kinetics for Flow Batteries. *J. Phys. Chem. C* **2015**, *119* (10), 5311–5318. https://doi.org/10.1021/jp5116806.

(38) Taylor, S. M.; Pătru, A.; Streich, D.; El Kazzi, M.; Fabbri, E.; Schmidt, T. J. Vanadium (V) Reduction Reaction on Modified Glassy Carbon Electrodes – Role of Oxygen Functionalities and Microstructure. *Carbon* **2016**, *109*, 472–478. https://doi.org/10.1016/j.carbon.2016.08.044.

(39) Park, M.; Jeon, I. Y.; Ryu, J.; Baek, J. B.; Cho, J. Exploration of the Effective Location of Surface Oxygen Defects in Graphene-Based Electrocatalysts for All-Vanadium Redox-

Flow Batteries. *Adv. Energy Mater.* **2015**, *5* (5), 1–7. https://doi.org/10.1002/aenm.201401550.

(40) Maruyama, J.; Maruyama, S.; Fukuhara, T.; Hanafusa, K. Efficient Edge Plane Exposure on Graphitic Carbon Fiber for Enhanced Flow-Battery Reactions. *J. Phys. Chem. C* **2017**, *121* (39), 24425–24433. https://doi.org/10.1021/acs.jpcc.7b07961.

(41) Sadezky, A.; Muckenhuber, H.; Grothe, H.; Niessner, R.; Poschl, U. Raman Microspectroscopy of Soot and Related Carbonaceous Materials: Spectral Analysis and Structural Information. *Carbon* **2005**, *43* (8), 1731–1742. https://doi.org/10.1016/j.carbon.2005.02.018.

(42) Reich, S.; Thomsen, C. Raman Spectroscopy of Graphite. *Philos. Trans. R. Soc. Math. Phys. Eng. Sci.* **2004**, *362*, 2271–2288. https://doi.org/10.1098/rsta.2004.1454.

(43) Bourke, A.; Miller, M. A.; Lynch, R. P.; Gao, X.; Landon, J.; Wainright, J. S.; Savinell, R. F.; Buckley, D. N. Electrode Kinetics of Vanadium Flow Batteries: Contrasting Responses of V^{II}-V^{III} and V^{IV}-V^{V} to Electrochemical Pretreatment of Carbon. *J. Electrochem. Soc.* **2016**, *163* (1), A5097–A5105. https://doi.org/10.1149/2.0131601jes.

(44) Forner-Cuenca, A.; Biesdorf, J.; Manzi-Orezzoli, V.; Gubler, L.; Schmidt, T. J.; Boillat, P. Advanced Water Management in PEFCs: Diffusion Layers with Patterned Wettability. *J. Electrochem. Soc.* **2016**, *163* (13), F1389–F1398. https://doi.org/10.1149/2.0891613jes.

(45) Borup, R.; Meyers, J.; Pivovar, B.; Kim, Y. S.; Mukundan, R.; Garland, N.; Myers, D.; Wilson, M.; Garzon, F.; Wood, D.; Zelenay, P.; More, K.; Stroh, K.; Zawodzinski, T.; Boncella, X. J.; Mcgrath, J. E.; Inaba, O. M.; Miyatake, K.; Hori, M.; Ota, K.; Ogumi, Z.; Miyata, S.; Nishikata, A.; Siroma, Z.; Uchimoto, Y.; Meyers, J. P.; Mcgrath, J. E. Scientific Aspects of Polymer Electrolyte Fuel Cell Durability and Degradation. *Chem.Rev.* **2007**, *107*, 3904–3951. https://doi.org/10.1021/cr050182l.

(46) Cassie, A. B. D.; Baxter, S. Wettability of Porous Surfaces. *Trans. Faraday Soc.* **1944**, *40* (5), 546–551. https://doi.org/10.1039/tf9444000546.

(47) Pasaogullari, U.; Wang, C. Y. Liquid Water Transport in Gas Diffusion Layer of Polymer Electrolyte Fuel Cells. *J. Electrochem. Soc.* **2004**, *151* (3), A399. https://doi.org/10.1149/1.1646148.

(48) Zhou, X. L.; Zhao, T. S.; An, L.; Zeng, Y. K.; Zhu, X. B. Performance of a Vanadium Redox Flow Battery with a VANADion Membrane. *Appl. Energy* **2016**, *180*, 353–359. https://doi.org/10.1016/j.apenergy.2016.08.001.

(49) Aaron, D.; Yeom, S.; Kihm, K. D.; Ashraf, Y.; Ertugrul, T.; Mench, M. M. Kinetic Enhancement via Passive Deposition of Carbon-Based Nanomaterials in Vanadium Redox Flow Batteries. *J. Power Sources* **2017**, *366*, 241–248. https://doi.org/10.1016/j.jpowsour.2017.08.108.

(50) Tang, Z. Proton Exchange Membrane Performance Characterization in VRFB. *ECS Trans.* **2012**, *41* (23), 25–34. https://doi.org/10.1149/1.3697451.

(51) Sun, C.-N.; Delnick, F. M.; Aaron, D. S.; Papandrew, A. B.; Mench, M. M.; Zawodzinski, T. A. Resolving Losses at the Negative Electrode in All-Vanadium Redox Flow Batteries

Using Electrochemical Impedance Spectroscopy. *J. Electrochem. Soc.* **2014**, *161* (6), A981–A988. https://doi.org/10.1149/2.045406jes.

(52) Fink, H.; Friedl, J.; Stimming, U. Composition of the Electrode Determines Which Half-Cell's Rate Constant Is Higher in a Vanadium Flow Battery. *J. Phys. Chem. C* **2016**, *120* (29), 15893–15901. https://doi.org/10.1021/acs.jpcc.5b12098.

(53) Blasi, A. Di; Blasi, O. Di; Briguglio, N.; Aricò, A. S.; Sebastián, D.; Lázaro, M. J.; Monforte, G.; Antonucci, V. Investigation of Several Graphite-Based Electrodes for Vanadium Redox Flow Cell. *J. Power Sources* **2013**, *227*, 15–23. https://doi.org/10.1016/j.jpowsour.2012.10.098.

(54) Kim, K. J.; Kim, Y. J.; Kim, J. H.; Park, M. S. The Effects of Surface Modification on Carbon Felt Electrodes for Use in Vanadium Redox Flow Batteries. *Mater. Chem. Phys.* **2011**, *131* (1–2), 547–553. https://doi.org/10.1016/j.matchemphys.2011.10.022.

(55) Chakrabarti, M. H.; Brandon, N. P.; Hajimolana, S. A.; Tariq, F.; Yufit, V.; Hashim, M. A.; Hussain, M. A.; Low, C. T. J.; Aravind, P. V. Application of Carbon Materials in Redox Flow Batteries. *J. Power Sources* **2014**, *253*, 150–166. https://doi.org/10.1016/j.jpowsour.2013.12.038.

(56) Zeng, L.; Zhao, T.; Wei, L. Revealing the Performance Enhancement of Oxygenated Carbonaceous Materials for Vanadium Redox Flow Batteries: Functional Groups or Specific Surface Area? *Adv. Sustain. Syst.* **2017**, *1700148*, 1700148. https://doi.org/10.1002/adsu.201700148.

(57) Melke, J.; Jakes, P.; Langner, J.; Riekehr, L.; Kunz, U.; Zhao-Karger, Z.; Nefedov, A.; Sezen, H.; Wöll, C.; Ehrenberg, H.; Roth, C. Carbon Materials for the Positive Electrode in All-Vanadium Redox Flow Batteries. *Carbon* **2014**, *78*, 220–230. https://doi.org/10.1016/j.carbon.2014.06.075.

(58) Zhong, S.; Skyllas-Kazacos, M. Electrochemical Behaviour of Vanadium (V)/Vanadium (IV) Redox Couple at Graphite Electrodes. *J. Power Sources* **1992**, *39*, 1–9.

(59) Aaron, D.; Sun, C.-N.; Bright, M.; Papandrew, A. B.; Mench, M. M.; Zawodzinski, T. A. In Situ Kinetics Studies in All-Vanadium Redox Flow Batteries. *ECS Electrochem. Lett.* **2013**, *2* (3), A29–A31. https://doi.org/10.1149/2.001303eel.

(60) Weber, A. Z.; Mench, M. M.; Meyers, J. P.; Ross, P. N.; Gostick, J. T.; Liu, Q. Redox Flow Batteries: A Review. *J. Appl. Electrochem.* **2011**, *41* (10), 1137–1164. https://doi.org/10.1007/s10800-011-0348-2.

(61) Deen, W. *Analysis of Transport Phenomena*, 2nd ed.; Oxford University Press: New York, 2012.

(62) Wong, A. A.; Aziz, M. J.; Rubinstein, S. M. Direct Visualization of Electrochemical Reactions and Comparison of Commercial Carbon Papers in Operando by Fluorescence Microscopy Using a Quinone-Based Flow Cell. *ECS Trans.* **2017**, *77* (11), 153–161.

(63) Forner-Cuenca, A.; Biesdorf, J.; Gubler, L.; Kristiansen, P. M.; Schmidt, T. J.; Boillat, P. Engineered Water Highways in Fuel Cells: Radiation Grafting of Gas Diffusion Layers. *Adv. Mater.* **2015**, *27* (41), 6317–6322. https://doi.org/10.1002/adma.201503557.

(64)   Jervis, R.; Brown, L. D.; Neville, T. P.; Millichamp, J.; Finegan, D. P.; Heenan, T. M. M.; Brett, D. J. L.; Shearing, P. R. Design of a Miniature Flow Cell for in Situ X-Ray Imaging of Redox Flow Batteries. *J. Phys. Appl. Phys.* **2016**, *49* (43), 434002. https://doi.org/10.1088/0022-3727/49/43/434002.

(65)   Gostick, J. T.; Ioannidis, M. A.; Fowler, M. W.; Pritzker, M. D. Pore Network Modeling of Fibrous Gas Diffusion Layers for Polymer Electrolyte Membrane Fuel Cells. *J. Power Sources* **2007**, *173* (1), 277–290. https://doi.org/10.1016/j.jpowsour.2007.04.059.

(66)   Pezeshki, A. M.; Sacci, R. L.; Veith, G. M.; Zawodzinski, T. A.; Mench, M. M. The Cell-in-Series Method: A Technique for Accelerated Electrode Degradation in Redox Flow Batteries. *J. Electrochem. Soc.* **2016**, *163* (1), 5202–5210. https://doi.org/10.1149/2.0251601jes.

(67)   Zhang, Y.; Liu, L.; Xi, J.; Wu, Z.; Qiu, X. The Benefits and Limitations of Electrolyte Mixing in Vanadium Flow Batteries. *Appl. Energy* **2017**, *204*, 373–381. https://doi.org/10.1016/j.apenergy.2017.07.049.

(68)   Jiang, B.; Wu, L.; Yu, L.; Qiu, X.; Xi, J. A Comparative Study of Nafion Series Membranes for Vanadium Redox Flow Batteries. *J. Membr. Sci.* **2016**, *510*, 18–26. https://doi.org/10.1016/j.memsci.2016.03.007.

(69)   Agar, E.; Benjamin, A.; Dennison, C. R.; Chen, D.; Hickner, M. A.; Kumbur, E. C. Reducing Capacity Fade in Vanadium Redox Flow Batteries by Altering Charging and Discharging Currents. *J. Power Sources* **2014**, *246*, 767–774. https://doi.org/10.1016/j.jpowsour.2013.08.023.

(70)   Agar, E.; Knehr, K. W.; Chen, D.; Hickner, M. A.; Kumbur, E. C. Species Transport Mechanisms Governing Capacity Loss in Vanadium Flow Batteries: Comparing Nafion and Sulfonated Radel Membranes. *Electrochimica Acta* **2013**, *98*, 66–74. https://doi.org/10.1016/j.electacta.2013.03.030.

(71)   Trogadas, P.; Taiwo, O. O.; Tjaden, B.; Neville, T. P.; Yun, S.; Parrondo, J.; Ramani, V.; Coppens, M. O.; Brett, D. J. L.; Shearing, P. R. X-Ray Micro-Tomography as a Diagnostic Tool for the Electrode Degradation in Vanadium Redox Flow Batteries. *Electrochem. Commun.* **2014**, *48*, 155–159. https://doi.org/10.1016/j.elecom.2014.09.010.

(72)   Derr, I.; Fetyan, A.; Schutjajew, K.; Roth, C. Electrochemical Analysis of the Performance Loss in All Vanadium Redox Flow Batteries Using Different Cut-off Voltages. *Electrochimica Acta* **2017**, *224*, 9–16. https://doi.org/10.1016/j.electacta.2016.12.043.

(73)   Petchsingh, C.; Quill, N.; Joyce, J. T.; Eidhin, D. N.; Oboroceanu, D.; Lenihan, C.; Gao, X.; Lynch, R. P.; Buckley, D. N. Spectroscopic Measurement of State of Charge in Vanadium Flow Batteries with an Analytical Model of V ^{IV} -V ^{V} Absorbance. *J. Electrochem. Soc.* **2016**, *163* (1), A5068–A5083. https://doi.org/10.1149/2.0091601jes.

(74)   Wu, L.; Wang, J.; Shen, Y.; Liu, L.; Xi, J. Electrochemical Evaluation Methods of Vanadium Flow Battery Electrodes. *Phys. Chem. Chem. Phys.* **2017**, *19* (22), 14708–14717. https://doi.org/10.1039/c7cp02581e.

(75)   Dixon, D.; Babu, D. J.; Langner, J.; Bruns, M.; Pfaffmann, L.; Bhaskar, A.; Schneider, J. J.; Scheiba, F.; Ehrenberg, H. Effect of Oxygen Plasma Treatment on the Electrochemical

Performance of the Rayon and Polyacrylonitrile Based Carbon Felt for the Vanadium Redox Flow Battery Application. *J. Power Sources* **2016**, *332*, 240–248. https://doi.org/10.1016/j.jpowsour.2016.09.070.

(76) Zeng, L.; Zhao, T.; Wei, L. Revealing the Performance Enhancement of Oxygenated Carbonaceous Materials for Vanadium Redox Flow Batteries: Functional Groups or Specific Surface Area? *Adv. Sustain. Syst.* **2018**, *2* (2), 1700148. https://doi.org/10.1002/adsu.201700148.

(77) Wang, R.; Li, Y.; He, Y.-L. Achieving Gradient-Pore-Oriented Graphite Felt for Vanadium Redox Flow Batteries: Meeting Improved Electrochemical Activity and Enhanced Mass Transport from Nano- to Micro-Scale. *J. Mater. Chem. A* **2019**, *7* (18), 10962–10970. https://doi.org/10.1039/C9TA00807A.

(78) Kim, K. J.; Kim, Y.-J.; Kim, J.-H.; Park, M.-S. The Effects of Surface Modification on Carbon Felt Electrodes for Use in Vanadium Redox Flow Batteries. *Mater. Chem. Phys.* **2011**, *131* (1–2), 547–553. https://doi.org/10.1016/j.matchemphys.2011.10.022.

(79) Zhou, X. L.; Zeng, Y. K.; Zhu, X. B.; Wei, L.; Zhao, T. S. A High-Performance Dual-Scale Porous Electrode for Vanadium Redox Flow Batteries. *J. Power Sources* **2016**, *325*, 329–336. https://doi.org/10.1016/j.jpowsour.2016.06.048.

(80) Flox, C.; Skoumal, M.; Rubio-Garcia, J.; Andreu, T.; Morante, J. R. Strategies for Enhancing Electrochemical Activity of Carbon-Based Electrodes for All-Vanadium Redox Flow Batteries. *Appl. Energy* **2013**, *109*, 344–351. https://doi.org/10.1016/j.apenergy.2013.02.001.

(81) Forner-Cuenca, A.; Brushett, F. R. Engineering Porous Electrodes for Next-Generation Redox Flow Batteries: Recent Progress and Opportunities. *Curr. Opin. Electrochem.* **2019**, *18*, 113–122. https://doi.org/10.1016/j.coelec.2019.11.002.

(82) Gautam, R. K.; Verma, A. Uniquely Designed Surface Nanocracks for Highly Efficient and Ultra-Stable Graphite Felt Electrode for Vanadium Redox Flow Battery. *Mater. Chem. Phys.* **2020**, *251*, 123178. https://doi.org/10.1016/j.matchemphys.2020.123178.

(83) Abbas, S.; Lee, H.; Hwang, J.; Mehmood, A.; Shin, H.-J.; Mehboob, S.; Lee, J.-Y.; Ha, H. Y. A Novel Approach for Forming Carbon Nanorods on the Surface of Carbon Felt Electrode by Catalytic Etching for High-Performance Vanadium Redox Flow Battery. *Carbon* **2018**, *128*, 31–37. https://doi.org/10.1016/j.carbon.2017.11.066.

(84) Shin, J. H.; Park, H. J.; Song, Y. il; Choi, Y. S.; Suh, S.-J. Morphological Optimization and Nitrogen Functionalization of Vertically Oriented CNW for High Performance Electrical Double Layer Capacitor Electrode. *Electrochimica Acta* **2020**, *348*, 136210. https://doi.org/10.1016/j.electacta.2020.136210.

(85) Rabbow, T. J.; Whitehead, A. H. Deconvolution of Electrochemical Double Layer Capacitance between Fractions of Active and Total Surface Area of Graphite Felts. *Carbon* **2017**, *111*, 782–788. https://doi.org/10.1016/j.carbon.2016.10.064.

(86) Tenny, K. M.; Forner-Cuenca, A.; Chiang, Y.-M.; Brushett, F. R. Comparing Physical and Electrochemical Properties of Different Weave Patterns for Carbon Cloth Electrodes in

Redox Flow Batteries. *J. Electrochem. Energy Convers. Storage* **2020**, *17* (4), 041108. https://doi.org/10.1115/1.4046661.

(87) Darling, R. M.; Perry, M. L. The Influence of Electrode and Channel Configurations on Flow Battery Performance. *J. Electrochem. Soc.* **2014**, *161* (9), A1381–A1387. https://doi.org/10.1149/2.0941409jes.

(88) Sun, C.-N. Hydrogen Evolution at the Negative Electrode of the All-Vanadium Redox Flow Batteries. *J. Power Sources* **2014**, 5.

(89) Forner-Cuenca, A.; Penn, E. E.; Oliveira, A. M.; Brushett, F. R. Exploring the Role of Electrode Microstructure on the Performance of Non-Aqueous Redox Flow Batteries. *J. Electrochem. Soc.* **2019**, *166* (10), A2230–A2241. https://doi.org/10.1149/2.0611910jes.

(90) Shi, H. Activated Carbons and Double Layer Capacitance. *Electrochimica Acta* **1996**, *41* (10), 1633–1639. https://doi.org/10.1016/0013-4686(95)00416-5.

(91) Brunauer, S.; Emmett, P. H.; Teller, E. Adsorption of Gases in Multimolecular Layers. *J. Am. Chem. Soc.* **1938**, *60* (2), 309–319. https://doi.org/10.1021/ja01269a023.

(92) Jagiello, J.; Olivier, J. P. 2D-NLDFT Adsorption Models for Carbon Slit-Shaped Pores with Surface Energetical Heterogeneity and Geometrical Corrugation. *Carbon* **2013**, *55*, 70–80. https://doi.org/10.1016/j.carbon.2012.12.011.

(93) Lastoskie, C.; Gubbins, K. E.; Quirke, N. Pore Size Heterogeneity and the Carbon Slit Pore: A Density Functional Theory Model. *Langmuir* **1993**, *9* (10), 2693–2702. https://doi.org/10.1021/la00034a032.

(94) Ravikovitch, P. I.; Vishnyakov, A.; Russo, R.; Neimark, A. V. Unified Approach to Pore Size Characterization of Microporous Carbonaceous Materials from N_2, Ar, and CO_2 Adsorption Isotherms [†]. *Langmuir* **2000**, *16* (5), 2311–2320. https://doi.org/10.1021/la991011c.

(95) Jagiello, J.; Tolles, D.; F. Meunier, editor. *Fundamentals of Adsorption*; Elsevier: Amsterdam, 1998; Vol. 6.

(96) Jagiello, J.; Ania, C.; Parra, J. B.; Cook, C. Dual Gas Analysis of Microporous Carbons Using 2D-NLDFT Heterogeneous Surface Model and Combined Adsorption Data of N2 and CO2. *Carbon* **2015**, *91*, 330–337. https://doi.org/10.1016/j.carbon.2015.05.004.

(97) Freudenberg Gas Diffusion Layers Technical Data. Freudenberg Performance Materials.

(98) Milshtein, J. D.; Kaur, A. P.; Casselman, M. D.; Kowalski, J. A.; Modekrutti, S.; Zhang, P. L.; Harsha Attanayake, N.; Elliott, C. F.; Parkin, S. R.; Risko, C.; Brushett, F. R.; Odom, S. A. High Current Density, Long Duration Cycling of Soluble Organic Active Species for Non-Aqueous Redox Flow Batteries. *Energy Environ. Sci.* **2016**, *9* (11), 3531–3543. https://doi.org/10.1039/C6EE02027E.

(99) Greco, K. V.; Forner-Cuenca, A.; Mularczyk, A.; Eller, J.; Brushett, F. R. Elucidating the Nuanced Effects of Thermal Pretreatment on Carbon Paper Electrodes for Vanadium Redox Flow Batteries. *ACS Appl. Mater. Interfaces* **2018**, *10* (51), 44430–44442. https://doi.org/10.1021/acsami.8b15793.

(100) Leonard, M. E.; Clarke, L. E.; Forner-Cuenca, A.; Brown, S. M.; Brushett, F. R. Investigating Electrode Flooding in a Flowing Electrolyte, Gas-Fed Carbon Dioxide Electrolyzer. *ChemSusChem* **2020**, *13* (2), 400–411. https://doi.org/10.1002/cssc.201902547.

(101) Rabbow, T. J.; Trampert, M.; Pokorny, P.; Binder, P.; Whitehead, A. H. Variability within a Single Type of Polyacrylonitrile-Based Graphite Felt after Thermal Treatment. Part I: Physical Properties. *Electrochimica Acta* **2015**, *173*, 17–23. https://doi.org/10.1016/j.electacta.2015.05.020.

(102) Sing, K. S. W. Assessment of Surface Area by Gas Adsorption. In *Adsorption by Powders and Porous Solids*; Elsevier, 2014; pp 237–268. https://doi.org/10.1016/B978-0-08-097035-6.00007-3.

(103) Records, W. C.; Yoon, Y.; Ohmura, J. F.; Chanut, N.; Belcher, A. M. Virus-Templated Pt–Ni(OH)2 Nanonetworks for Enhanced Electrocatalytic Reduction of Water. *Nano Energy* **2019**, *58*, 167–174. https://doi.org/10.1016/j.nanoen.2018.12.083.

(104) Thommes, M.; Kaneko, K.; Neimark, A. V.; Olivier, J. P.; Rodriguez-Reinoso, F.; Rouquerol, J.; Sing, K. S. W. Physisorption of Gases, with Special Reference to the Evaluation of Surface Area and Pore Size Distribution (IUPAC Technical Report). *Pure Appl. Chem.* **2015**, *87* (9–10), 1051–1069. https://doi.org/10.1515/pac-2014-1117.

(105) Han, J.; Yoshimoto, N.; Todorov, Y. M.; Fujii, K.; Morita, M. Characteristics of the Electric Double-Layer Capacitors Using Organic Electrolyte Solutions Containing Different Alkylammonium Cations. *Electrochimica Acta* **2018**, *281*, 510–516. https://doi.org/10.1016/j.electacta.2018.06.012.

(106) Marcus, Y. Volumes of Aqueous Hydrogen and Hydroxide Ions at 0 to 200 °C. *J. Chem. Phys.* **2012**, *137* (15), 154501. https://doi.org/10.1063/1.4758071.

(107) Mountain, R. D. Solvation Structure of Ions in Water. *Int. J. Thermophys.* **2007**, *28* (2), 536–543. https://doi.org/10.1007/s10765-007-0154-6.

(108) Kim, Y.-J.; Masutzawa, Y.; Ozaki, S.; Endo, M.; Dresselhaus, M. S. PVDC-Based Carbon Material by Chemical Activation and Its Application to Nonaqueous EDLC. *J. Electrochem. Soc.* **2004**, *151* (6), E199. https://doi.org/10.1149/1.1715095.

(109) Rodriguez-Reinoso, F.; Linares-Solano, A.; P.A. Thrower, editor. *Chemistry & Physics of Carbon*; Marcel Dekker: New York, 1988; Vol. 21.

(110) Jagiello, J.; Thommes, M. Comparison of DFT Characterization Methods Based on N2, Ar, CO2, and H2 Adsorption Applied to Carbons with Various Pore Size Distributions. *Carbon* **2004**, *42* (7), 1227–1232. https://doi.org/10.1016/j.carbon.2004.01.022.

(111) Jagiello, J. Stable Numerical Solution of the Adsorption Integral Equation Using Splines. *Langmuir* **1994**, *10* (8), 2778–2785. https://doi.org/10.1021/la00020a045.

(112) Garrido, J.; Linares-Solano, A.; Martin-Martinez, J. M.; Molina-Sabio, M.; Rodriguez-Reinoso, Francisco.; Torregrosa, R. Use of Nitrogen vs. Carbon Dioxide in the Characterization of Activated Carbons. *Langmuir* **1987**, *3* (1), 76–81. https://doi.org/10.1021/la00073a013.

(113) Jagiello, J.; Kenvin, J.; Ania, C. O.; Parra, J. B.; Celzard, A.; Fierro, V. Exploiting the Adsorption of Simple Gases O2 and H2 with Minimal Quadrupole Moments for the Dual Gas Characterization of Nanoporous Carbons Using 2D-NLDFT Models. *Carbon* **2020**, *160*, 164–175. https://doi.org/10.1016/j.carbon.2020.01.013.

(114) Magnin, Y.; Chanut, N.; Pantano, D. A.; Chaput, E.; Ulm, F. J.; Pellenq, R. J.-M.; Villermaux, E. Granular-like Behavior of Molecular Flow in Constricted Nanopores. *ArXiv201108594 Cond-Mat Physicsphysics* **2020**.

(115) Chmiola, J.; Largeot, C.; Taberna, P.-L.; Simon, P.; Gogotsi, Y. Desolvation of Ions in Subnanometer Pores and Its Effect on Capacitance and Double-Layer Theory. *Angew. Chem. Int. Ed.* **2008**, *47* (18), 3392–3395. https://doi.org/10.1002/anie.200704894.

(116) Faucher, S.; Aluru, N.; Bazant, M. Z.; Blankschtein, D.; Brozena, A. H.; Cumings, J.; Pedro de Souza, J.; Elimelech, M.; Epsztein, R.; Fourkas, J. T.; Rajan, A. G.; Kulik, H. J.; Levy, A.; Majumdar, A.; Martin, C.; McEldrew, M.; Misra, R. P.; Noy, A.; Pham, T. A.; Reed, M.; Schwegler, E.; Siwy, Z.; Wang, Y.; Strano, M. Critical Knowledge Gaps in Mass Transport through Single-Digit Nanopores: A Review and Perspective. *J. Phys. Chem. C* **2019**, *123* (35), 21309–21326. https://doi.org/10.1021/acs.jpcc.9b02178.

(117) Marcus, Y. *Ions in Solution and Their Solvation*; John Wiley & Sons, Inc: Hoboken, NJ, 2015. https://doi.org/10.1002/9781118892336.

(118) Suga, T.; Pu, Y.-J.; Oyaizu, K.; Nishide, H. Electron-Transfer Kinetics of Nitroxide Radicals as an Electrode-Active Material. *Bull. Chem. Soc. Jpn.* **2004**, *77* (12), 2203–2204. https://doi.org/10.1246/bcsj.77.2203.

(119) Aris, R. On Shape Factors for Irregular Particles—I. *Chem. Eng. Sci.* **1957**, *6* (6), 262–268. https://doi.org/10.1016/0009-2509(57)85028-3.

(120) Maruyama, Y.; Nagamine, K.; Nomura, A.; Iwasa, S.; Tokito, S. Electrochemical Characterization of TEMPO Radical in Ionic Liquids. *Electrochemistry* **2020**, *88* (1), 34–38. https://doi.org/10.5796/electrochemistry.19-00054.

(121) Weber, A. Z.; Mench, M. M.; Meyers, J. P.; Ross, P. N.; Gostick, J. T.; Liu, Q. Redox Flow Batteries: A Review. *J. Appl. Electrochem.* **2011**, *41* (10), 1137–1164. https://doi.org/10.1007/s10800-011-0348-2.

(122) Braff, W. A.; Buie, C. R.; Bazant, M. Z. Boundary Layer Analysis of Membraneless Electrochemical Cells. *J. Electrochem. Soc.* **2013**, *160* (11), A2056–A2063. https://doi.org/10.1149/2.052311jes.

(123) Brenner, A. *Electrodeposition of Alloys Principles and Practice*; Academic Press Inc., 1963; Vol. 1.

(124) Yang, Z.; Gerhardt, M. R.; Fortin, M. E.; Shovlin, C.; Weber, A. Z.; Perry, M. L.; Darling, R. M.; Saraidaridis, J. D. Polysulfide-Permanganate Flow Battery Using Abundant Active Materials. *J. Electrochem. Soc.* **2021**. https://doi.org/10.1149/1945-7111/ac1036.

(125) Zhou, H.; Zhang, H.; Zhao, P.; Yi, B. Novel Cobalt Coated Carbon Felt as High Performance Negative Electrode in Sodium Polysulfide/Bromine Redox Flow Battery. *Electrochemistry* **2006**, *74* (4), 296–298. https://doi.org/10.5796/electrochemistry.74.296.

(126) Aaron, D. S.; Liu, Q.; Tang, Z.; Grim, G. M.; Papandrew, A. B.; Turhan, A.; Zawodzinski, T. A.; Mench, M. M. Dramatic Performance Gains in Vanadium Redox Flow Batteries through Modified Cell Architecture. *J. Power Sources* **2012**, *206*, 450–453. https://doi.org/10.1016/j.jpowsour.2011.12.026.

Permissions

Chapter II was reproduced in part with permission from K.V. Greco, A. Forner-Cuenca, A. Mularczyk, J. Eller, F. R. Brushett, Elucidating the Nuanced Effects of Thermal Pretreatment on Carbon Paper Electrodes for Vanadium Redox Flow Batteries, *ACS Appl. Mat. Interfaces* 2018 *10* (51), 44430–44442. Copyright 2018 American Chemical Society. **Chapter III** and **Chapter IV** are reproduced in part with permission from *ACS Energy Materials*. Unpublished work copyright 2021 American Chemical Society. **Chapter V** contains results that, in some form, may be submitted for publication in a peer-reviewed journal in the future.